

# RAM

● ROBOTICS  
AND  
MECHATRONICS

## DESIGN OF PNEUMATIC SOFT SURGICAL ROBOT FOR ENDOSCOPIC NOTES AND MIS APPLICATION WITH REDUCED SIZE

Y. (Yuanxiang) Lin

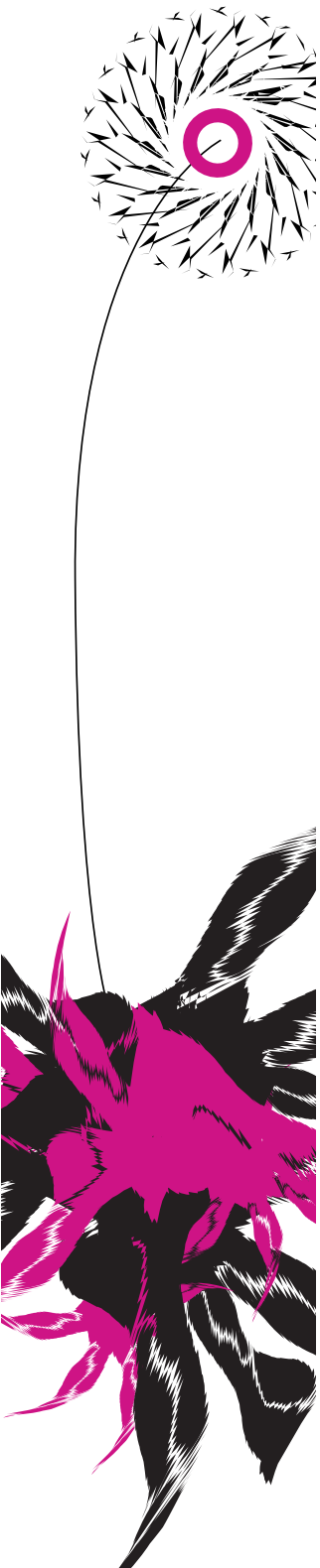
MSC ASSIGNMENT

**Committee:**

prof. dr. ir. G.J.M. Krijnen  
Y.X. Mak, MSc  
dr. ir. M. Abayazid  
dr. ir. H. Naghibi Beidokhti  
ir. E.E.G. Hekman

December, 2019

055RaM2019  
Robotics and Mechatronics  
EEMathCS  
University of Twente  
P.O. Box 217  
7500 AE Enschede  
The Netherlands



## Summary

Minimal invasive surgery (MIS) and natural orifice transluminal endoscopic surgery (NOTES) are gradually replacing traditional open surgery for reducing the pain of patient and the recovery time. In both MIS and NOTES applications, endoscope is an indispensable tool.

STIFF-FLOP (Stiffness Controllable Flexible and Learnable Manipulator for Surgical Operation) manipulator is a modular pneumatic flexible endoscope for colonoscopy. However, it is not suitable for laparoscopy in terms of size. For this reason, it is necessary to downscale STIFF-FLOP manipulator so that it can be applicable for laparoscopic application. In addition, STIFF-FLOP manipulator has several issues such as non-linear actuation and tradeoff between bending performance and space for equipment.

This study aims to downscale STIFF-FLOP manipulator for laparoscopy, and to develop control method on the bending of the downscaled design to compensate for different module orientations and limited load.

The downscaled STIFF-FLOP design (which is called the new design in this article) is developed based on literature survey on size requirement and constant curvature model. The body of the new design is an elastomeric cylinder which is 11.5 mm in diameter. Three arc chambers are embedded into the cylinder. Theoretically, the arc chamber which cross-section area is 17.6 mm<sup>2</sup> results in the maximal bending performance of the new design. The radial expansion of inflated chamber is limited by an external braided sheath which is fixed at both ends of the new design.

In this study, the new design is characterized by one-plane bending angle. The mechanical experiment is conducted for obtaining the system characterization of the new design, which is the relationship between one-plane bending angle and air pressure, in terms of one chamber bending and two-chamber bending. The result of experiment shows the new design is able to obtain 90° under pressure 0.38 bar. Based on the value of the gradient of the bending angle to air pressure, the static bending performance of the new design can be divided into three parts: the zero-bending zone, gradient increasing part and gradient decreasing part.

The bending hysteresis behavior of the new design is measured in this project. The maximum difference of bending angle in hysteresis behavior is 13.7°. Insights on reasons causing bending hysteresis of the new design are provided in this article.

To examine the constant curvature assumption, the backbone curvature of the bending module is compared with the estimated backbone curvature of constant radius. The deviation between these two curvatures reveals that the new design is not compliant with constant curvature model. This conclusion is also confirmed by the difference between the analytical model and the system characterization.

When all three chambers are actuated by 0.4 bar air pressure simultaneously, the new design can elongate 5.3 mm which is 10.6% with respect to the initial length of the module.

PID feedback control system is designed to compensate for the influence of different module orientations and limited load on the one-plane bending angle of the new design. To improve the response of PID controller, the feedforward controller is implemented based on system characterization. The validation experiments are conducted on the module in vertical, inverted and horizontal module orientations, and on the module with load to examine the control performance. The dynamic and static control performance are acceptable when the reference bending angle is more than 15°. However, the bending of the new design is not able to follow the trajectory when the desired bending angle is less than 15°. In addition, it has issues such as non-zero initial bending angle, consistent bending, pulse noise and oscillation around static reference signal.

## Acknowledgements

The work in this report has benefited from the support of the following people. Without their support, it is impossible for me to finish the work. Therefore, I would like to show my gratitude to them.

I would like to thank my parents for supporting me with finance. My study would have been impossible without their support.

I would also like to thank my supervisors, Momen Abayazid, Hamid Naghibi Beidokhti and Yoeko Mak for their guidance and support throughout the study. I have gained a lot on designing soft pneumatic endoscope and implementing feedback control loop from the discussion with them. Thank you for always being there when I needed help.

Thanks for prof.dr.ir. Gijs Krijnen and ir. E.E.G. Hekman for becoming my committee members.

In addition, I would like to thank friends at work who gave their time to provide me insights, especially Antonio Lanciano and Jornt Lagaveen. A special thank to Jan Lenssen, as he designed pneumatic driver shield which I used in the system characterization experiment.

Next to that, I would like to thank the technicians, Sander Smit and Henny Kuipers, who helped me realize the 3D-printed parts and provided many practical tips on 3D-printing and molding processes.

## Table of Contents

Summary .....	ii
Acknowledgements .....	iii
Table of Contents .....	iv
List of Figures .....	vi
List of Tables .....	ix
1. Introduction.....	10
1.1. Context.....	10
1.2. Limitation of previous soft endoscope.....	10
1.3. Research Question .....	12
1.4. Thesis Outline .....	13
2. Background.....	14
2.1. Introduction.....	14
2.2. Soft pneumatic actuators.....	14
2.3. State-of-art designs of soft pneumatic endoscope.....	16
2.3.1. CMMPAM .....	16
2.3.2. Chip-on-tip endoscope .....	17
2.3.3. STIFF-FLOP surgical manipulator .....	17
2.3.4. MOLLUSC Module .....	19
3. Design of downscaled pneumatic soft endoscope.....	21
3.1. Design requirements .....	21
3.2. Survey of the design requirement on size .....	21
3.2.1. MIS application.....	21
3.2.2. NOTES application.....	21
3.3. Design modification.....	22
3.3.1. Single Segment Model based on Constant Curvature model.....	22
3.3.2. Design objective.....	24
3.3.3. Design improvements .....	24
3.4. Fabrication .....	30
3.5. Discussion and conclusion .....	33
4. Characterization of a single soft pneumatic module .....	34
4.1. Aim of experiment .....	34
4.2. Experiments setups .....	34
4.2.1. Equipment .....	34
4.2.2. Experiment methodology .....	37
4.2.3. Test protocols.....	39
4.3. System characterization results.....	39

---

4.3.1.	One chamber bending .....	39
4.3.2.	Two-chamber bending .....	41
4.3.3.	Examining assumption of constant curvature model .....	44
4.3.4.	Elongation of the module with three actuated chambers .....	47
4.3.5.	Bending Hysteresis .....	47
4.3.6.	Comparison between analytical model and system characterization .....	49
4.4	Conclusion of experimental characterization.....	51
5.	Control of bending angle of single module in one plane .....	52
5.1.	Feedback and Feedforward algorithm for bending control.....	54
5.1.1.	Combination of PID feedback controller and feedforward controller .....	55
5.1.2.	Implementation of feedforward controller.....	56
5.2.	Experiments on bending control .....	56
5.3.	Results of experiments of bending control.....	57
5.4.	Conclusion of one-plane bending angle control of new design .....	63
6.	Conclusion and Future Work .....	65
6.1.	Conclusion .....	65
6.2.	Future works .....	66
	Bibliography .....	67
	Appendices.....	69
	Appendix 1. Influence of unfixed external braided sheath on system characterization.....	69
	Appendix 2. List of material for downscaled STIFF-FLOP design.....	70
	Appendix 3. Detailed fabrication processes.....	71

## List of Figures

Figure 1.1 (a) Longitudinal and transversal cross section of STIFF-FLOP design with semi-cylindrical fluidic chambers and the central stiffening channel [3]. (b) Effect of inflation of chamber in STIFF-FLOP design without the limitation of radial expansion by external crimped braided sheath [3].....	11
Figure 1.2 Bending capability of STIFF-FLOP design under the action of increasing pressure: the upper line refers to single chamber activation, lower line refers to two chambers activation [3] ....	11
Figure 1.3 The illustration of characteristics of STIFF-FLOP design. ....	12
Figure 2.1 Illustration of soft robotic endoscopes implemented in MIS and NOTES application. (left) modular soft robotic endoscope is implemented in laparoscopy (MIS application) [9]. (right) soft robotic endoscope applied in colonoscopy (NOTES application) .....	14
Figure 2.2 Pneu-net actuator designed by Bobak Mosadegh [8] .....	15
Figure 2.3 Structure and action of McKibben pneumatic artificial muscle.[10].....	15
Figure 2.4 Structure of Fiber reinforcement actuator.[12].....	16
Figure 2.5 (a) schematic design of CMMPAM manipulator (b) prototype of CMMPAM manipulator. ....	16
Figure 2.6 One degree-of-freedom chip-on-tip endoscope.....	17
Figure 2.7 Cross section of STIFF-FLOP, perpendicular to the chamber axis.....	18
Figure 2.8 Chamber cross-section center shifts during two chambers simultaneous actuation. ....	19
Figure 2.9 Design of MOLLUSC manipulator (left) top view of the mold, (right) side view of the mold [2].....	20
Figure 2.10 (Left)Unactuated state of MOLLOSC design. (Right) Cross-section shape when two chambers are actuated. ....	20
Figure 3.1 Schematic representation of the colonic segments and landmarks [18] .....	22
Figure 3.2 Module bending with no presence of external force.....	23
Figure 3.3 Elongation of a fragment of the module .....	24
Figure 3.4 Bend of the module at a point along its axial direction [7].....	24
Figure 3.5 Primary design of downscaled STIFF-FLOP manipulator inspired by Frasc, J [5]. (Left) The dimension of primary design. (Right) Chamber braiding concept [5].....	25
Figure 3.6 Secondary design of downscaled STIFF-FLOP manipulator (Left) The dimension of secondary design. (Right) Illustration of the design of Abidi, H [9] .....	26
Figure 3.7 Third design of downscaled STIFF-FLOP manipulator. Three chambers constitute one MP.....	26
Figure 3.8 Improvement from triple-cylinder configuration to arc configuration. ....	27
Figure 3.9 Design of a single module. Illustration of the module design: main dimensions, view of the structure of the internal chambers, main dimensions from top view and front view .....	29
Figure 3.10 Analytical model of the new design in bending angle versus air pressure .....	30
Figure 3.11 Molds of pneumatic soft robotic endoscope. Top: from left to right: central cylinder, shell A, cap A, chamber A, alignment. Bottom: from left to right: chamber B, cap B, shell B.....	30

Figure 3.12 Molding processes of downscaled STIFF-FLOP design. (a) fabrication of chamber part. (b) bottom part molding. (c) Three chamber A molds are replaced by three chamber B molds. (d) Top part molding.....	32
Figure 3.13 (a) braided sleeve with diameter of 5mm (Farnell 1297224). (b) the heat gun to harden the structure (c) the sleeve is pushed down until the crimped structure is formed. (d) Complete integration of module.....	33
Figure 4.1 The dimension of the coil sensor (NDI medical). Due to the size of coil sensor is only 0.8 mm x 11 mm, no external force is on new design caused by the weight of coil sensor. ....	35
Figure 4.2 (a) Initial state and activated state of new design in vertical module orientation. The bending moment of new design along Z-axis is 0. (b) The coil sensor is attached to top end of the module with double layer tape.....	35
Figure 4.3 Digital pressure regulator (Festo).....	36
Figure 4.4 The combination of the pneumatic driver shield and the Arduino Uno microcontroller [6]. Pneumatic driver shield is located on top layer while Uno microcontroller is placed on the bottom layer. ....	36
Figure 4.5 The layout of pneumatic driver shield [6]. (A) DC input for 24V power supply. (B) four connectors for connecting maximal four pressure regulator. (C) connectors for connecting maximal four solenoid valves which will not be used in this project. (D) jumper determining whether the Arduino Uno is powered by a separate source. (E) pin numbering information for connecting hardware. (F) the auxiliary analog inputs $A_i$ .....	37
Figure 4.6 Schematic diagraph of system characterization experiment. The tracking of the tip of new design by coil sensor is synchronized with varying input pressure to new design .....	38
Figure 4.7 (a) bending angle of the new design tracked by coil sensor on time (b) pressure values of the new design adjusted by pressure regulator on time.....	38
Figure 4.8 Synchronized plot presenting the relationship between bending angle of new design and the input air pressure.....	38
Figure 4.9 Bending angle versus pressure characteristic for three single chambers bending.....	40
Figure 4.10 The increase rate of bending angle in terms of air pressure. The increasement equals 0.0039 bar in this project .....	41
Figure 4.11 Bending angle versus pressure for two chambers bending.....	42
Figure 4.12 Gradient of two-chamber bending respect to air pressure .....	43
Figure 4.13 Comparison of system characterization between one chamber bending and two-chamber bending. (a) Comparison of system characterization between chamber 1 and chamber 2&3 (b) Comparison of system characterization between chamber 2 and chamber 1&3 (c) Comparison between system characterization between chamber 3 and chamber 1&2. ....	44
Figure 4.14 Bending angle versus pressure characteristic for chamber 1, chamber 2 and the combination of chamber 1 and chamber 2.....	44
Figure 4.15 Bent configuration of module captured by camera view.....	45
Figure 4.16 Length of inner curvature, outer curvature and backbone curvature under different pressures.....	46
Figure 4.17 Elongation versus pressure graph for actuating all three chambers simultaneously .....	47
Figure 4.18 Hysteresis of bending angle with pressure varying in ascending and descending order.....	48

Figure 4.19 Hysteresis of Eco-Flex 0030 under UX (uniaxial),PS (pure shear),EB (equibiaxial) loading [20]..... 49

Figure 4.20 Hysteresis of Eco-Flex 0050 when strain is less than 0.2 [21]..... 49

Figure 4.21 Comparison between analytical model and system characterization..... 50

Figure 5.1 Kinematics model of constant curvature continuum robot (Webster,2010) [24] ..... 52

Figure 5.2 (left) constant curvature arc, the position of the tip in one-plane can be presented by the curvature radius  $r$  and the bending angle  $\alpha$ . (Right) arc parameters in constant curvature model,  $l$  is the length of the module,  $\kappa$  is the curvature of the module which equals reciprocal of  $r$ ,  $\beta$  is the out-of-plane rotation angle [24] ..... 52

Figure 5.3 (a) Aurora 6DOF Disc sensor (b) the combination of Disc sensor on tip of the module in vertical orientation. .... 53

Figure 5.4 Module without load in different module orientations (a) Vertical module orientation. (b) Inverted module orientation. (c) Horizontal module orientation ..... 54

Figure 5.5 Module with load in different module orientations. (a) Vertical module orientation. (b) Inverted module orientation. (c) Horizontal module orientation ..... 54

Figure 5.6 (a) Positive value of bending angle corresponds to positive value of pressure. (b) Negative value of bending angle corresponds to negative value of pressure. (c) The bottom view of module. .... 55

Figure 5.7 The block diagram of the entire closed loop system for controlling one-plane bending angle  $\alpha$  ..... 55

Figure 5.8 System characterization for both positive bending and negative bending..... 56

Figure 5.9 Implementation of the control system on hardware level. The desired bending angle  $\alpha$  is sent to the feedback and feedforward controller. By calculating the error between the current bending angle and the desired bending angle, the controller sends the control effort  $\mu$  to Arduino Uno which translates the control effort to the voltage of two regulators. Regulator 1 controls the pressure of chamber 1 and regulator 2 controls the pressure of chamber 2 and chamber 3..... 57

Figure 5.10 Desired one-plane bending angle as reference signal. (a) reference bending signal for positive bending (b) reference bending angle for negative bending ..... 57

Figure 5.11 Control performance on module in vertical module orientation (a) Positive bending for module without load (b) Negative bending for module without load (c) Positive bending for module with load (d) Negative bending for module with load ..... 59

Figure 5.12 Control performance on module in inverted orientation. (a) Positive bending for module without load (b) Negative bending for module without load (c) Positive bending for module with load (d) Negative bending for module with load ..... 61

Figure 5.13 Control performance on module in horizontal orientation. (a) Positive bending for module without load (b) Negative bending for module without load (c) Positive bending for module with load (d) Negative bending for module with load ..... 63

Figure A1. Tested new design with unfixed braided sheath. (a) Case 1: The length of external braided sheath is the same as elastomer. (b) Case 2: The external braided sheath elongates and its fiber angle increases. (c) Case 3: The external braided sheath is compressed and its fiber angle decreases. .... 69

Figure A2 System characterization of new design with unfixed external braided sheath shown in Figure A1 ..... 70

---

## List of Tables

Table 2-1 Active performance of STIFF-FLOP design [3] .....	19
Table 3-1 Comparison of the colonic segmental diameter in supine and prone orientations in 24 patients (mean $\pm$ SD (median)) [18] .....	22
Table 3-2 Performance comparison between primary design, secondary design, third design and final design.....	28
Table 3-3 Numerical values and meaning of symbols of the final design in Equation (8).....	29
Table 3-4 Material of molds in corresponding molding processes .....	31
Table 3-5 Material of each part of new design .....	31
Table 4-1 Length of the module backbone under different pressures.....	46
Table 5- 1 Time of new design to start following the trajectory for different module orientations and limited load.....	61

---

# 1. Introduction

## 1.1. Context

Open surgery is the traditional type of surgery in which an incision is made using a scalpel. The incision in open surgery ranges from 7 to 10 cm to even larger, depending on the procedure being performed. In order to reduce the size of incision and the pain of patient, techniques of minimally invasive surgery (MIS) are becoming more prevalent. These surgeries use multiple incisions less than 2.5 cm in length. An endoscope and instruments are inserted into these incisions. With the endoscope, the surgeon is able to perform technical operation. Different from MIS, natural orifice transluminal endoscopic surgery (NOTES) makes use of body natural orifice such as vagina or mouth for surgical instrument to be inserted. In both MIS and NOTES, endoscope is an indispensable tool.

In general, endoscope can be divided into two types: rigid and flexible endoscope. Compared with traditional rigid endoscope, soft robotic endoscope has several advantages. Soft robotic endoscope can circumambulate the obstacle which might be located between the target object and incision position. The soft robotic endoscope is fabricated by silicone which will not cause over sensitive symptoms when touching human body. Its biocompatibility and elastomeric nature also make the interaction of soft robotic endoscope with surrounding organs and tissues without running the risk of damage [1].

## 1.2. Limitation of previous soft endoscope

Compared with conventional rigid endoscope, currently there are several limitations posing on soft endoscopic instruments in MIS and NOTES applications. Flexible endoscope might be unstable in doing the surgical intervention due to the lack of stiffness. In case of colonoscopy, the lack of stiffness control might prevent endoscope advancing in a sharp turn in the colon [2]. The localization of the endoscope inside the patient's body is another problem. For instance, when flexible endoscope traces a lumen, the view from the endoscope camera might not indicate how far the endoscope has gone inside the lumen. Another major limitation is that while the distal tip of soft endoscope can be controlled, the rest of soft endoscope cannot.

A previous soft robotic endoscopic design, STIFF-FLOP, titled "Stiffness Controllable Flexible and Learnable Manipulator for Surgical Operation" has been studied and tested in lab environment by Cianchetti [3]. This design provides method to solve limitations of flexible endoscope mentioned above. The structure of STIFF-FLOP design is shown in Figure 1.1 (a). The body of STIFF-FLOP design consists of an elastomeric cylinder (EcoFlex 00-50, Smooth-on Inc). Three semi-circular fluidic chambers are embedded in the body of STIFF-FLOP design and they are equally spaced in a radial arrangement for omnidirectional bending. The central part of the body houses the stiffness channel consisting of a cylindrical membrane filled with granular material. The inflation of chamber in the longitudinal direction of STIFF-FLOP design results in the bending of the module. An external crimped braided sheath surrounds the body of STIFF-FLOP design to limit the radial expansion of the chamber when it is inflated with air pressure.

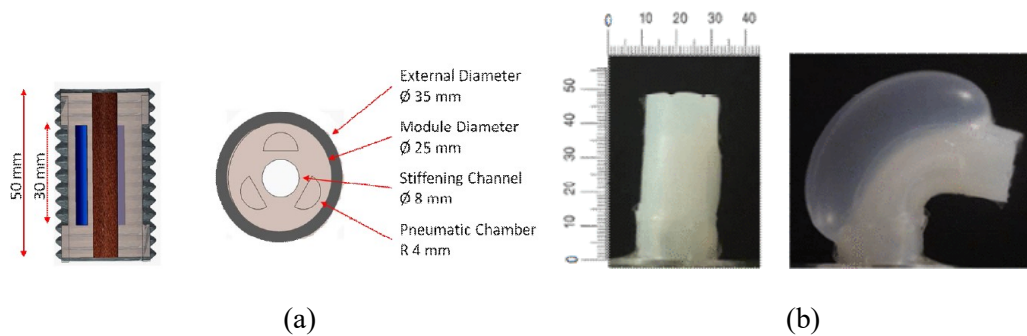


Figure 1.1 (a) Longitudinal and transversal cross section of STIFF-FLOP design with semi-cylindrical fluidic chambers and the central stiffening channel [3]. (b) Effect of inflation of chamber in STIFF-FLOP design without the limitation of radial expansion by external crimped braided sheath [3]

However, STIFF-FLOP design also has several limitations. One important issue is downscaling. Downscaling the current STIFF-FLOP design is necessary because that external diameter of STIFF-FLOP design is 25 mm while the standard trocar utilized in laparoscopy is 12 mm in diameter. It makes STIFF-FLOP design unacceptable for laparoscopy. However, it is not straightforward to downscale the manipulator because some functions like squeezing and stiffening might be excluded due to downscaling [4]. In addition, downscaling STIFF-FLOP design will change its bending ability. It makes the bending ability of downscaled STIFF-FLOP unpredictable.

Another limitation of STIFF-FLOP design is the non-linear actuation due to the change of the chamber cross-section area, when it is inflated by air pressure [5]. It is difficult to control the bending performance of soft robotic endoscope which is a non-linear actuation system. Moreover, as shown in Figure 1.2, the bending capability of single chamber activation is different from the bending capability of two chambers activation. They are due to the non-uniform inflation of chamber. When the chamber is inflated, it will not retain its initial semi-circular cross-section shape. It results in non-linear actuation and the difference of bending capability between single chamber activation and two chambers activation. A method to solve these limitation is applying inner sheath around each chamber [5]. However, the inner sheath requires higher pressure to achieve the same bending angle compared to design without inner sheath [6].

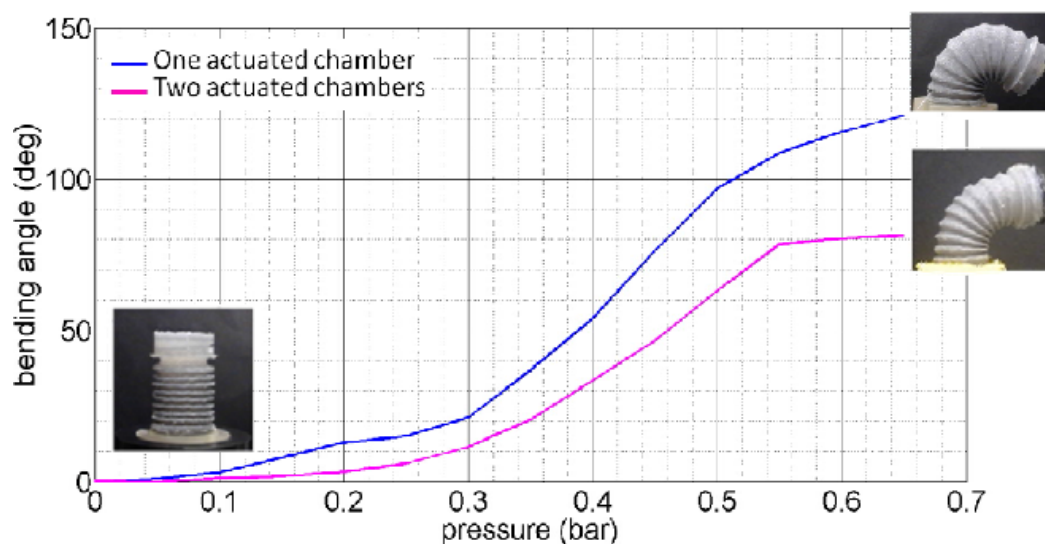


Figure 1.2 Bending capability of STIFF-FLOP design under the action of increasing pressure: the upper line refers to single chamber activation, lower line refers to two chambers activation [3]

Another important issue is the tradeoff between the size of pneumatic chambers and the space for equipment such as camera, pressure control lines, wires and modular connection parts. The amount of elongation of chamber is dependent on the stiffness of the module and pressure-induced force which is along the axial direction of chamber. The stiffness of the module depends on the geometry of the module.

The pressure-induced force is proportional to the transversal cross-section area of the chamber [7]. Due to the limited space for both chamber and equipment, the tradeoff between the bending performance and the spare space for equipment should be studied because high pressure is unacceptable which poses a risk to patient safety [3].

It is shown in Figure 1.3 that the STIFF-FLOP design has several characteristics like squeezing, elongation and bending. Among these characteristics, the bending is the most significant characteristic. The system characterization in this project refers to the process of obtaining the mathematical relationship between the bending angle of STIFF-FLOP design and the input air pressure. The example of system characterization is shown in Figure 1.2.

It is useful for system characterization to control the bending performance of STIFF-FLOP design. However different modules may have different system characterization due to the fabrication of STIFF-FLOP design consisting of several molding processes. Even when the module is placed in different module orientations e.g. vertical, inverted and horizontal module orientations, the different effect of the module gravity could result in different system characterization. Figure 1.3 shows that the STIFF-FLOP design is placed in vertical module orientation. In practical applications, soft robotic endoscope could not be placed in vertical module orientation, like in laparoscopy, the soft robotic endoscope is placed in inverted module orientation. It is even possible that the soft robotic endoscope could be inserted into patient's body horizontally. In addition, the load on the tip of STIFF-FLOP design could also influence the static system characterization. It is time-consuming to obtain system characterization for single STIFF-FLOP module with all possible module orientations and loads. Therefore, it is required to find an optimal method to control the bending performance of soft robotic endoscope without applying different system characterization.

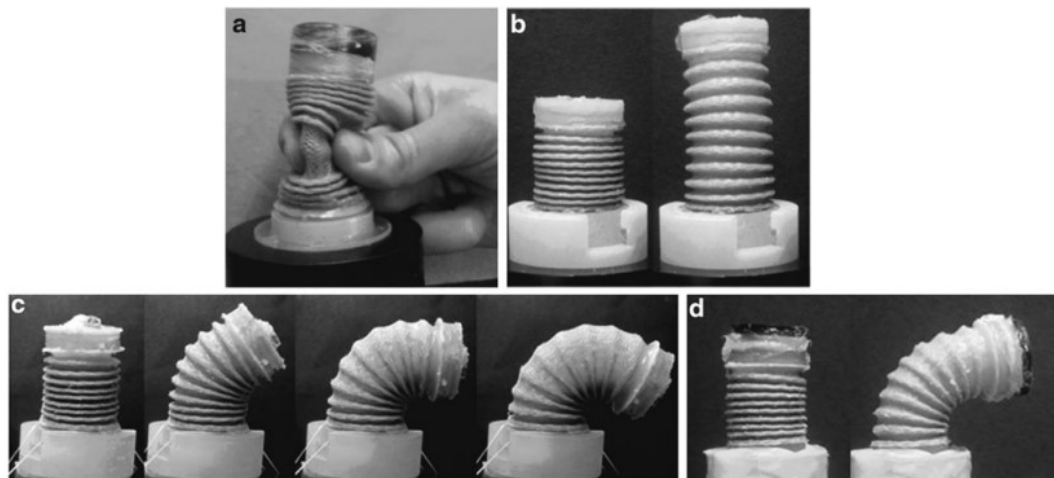


Figure 1.3 The illustration of characteristics of STIFF-FLOP design.  
 (a) Squeezing capability, (b) elongation, and bending behavior with one or two internal chambers activated (c,d) [4]

### 1.3. Research Question

Generally, the aim of this project is to design a soft robotic endoscope that is able to be applied in both MIS and NOTES applications. In addition, a control method should be developed for the new design to achieve the desired bendability under different external conditions.

The research question can be specified as “How to downscale and control a soft pneumatic endoscope based on the STIFF-FLOP design to compensate for load and different module orientations for laparoscopic applications?”.

To answer this question, the following research questions will be addressed:

- a. How to downscale the STIFF-FLOP design while the range of bendability of the new design

- can be maximized for laparoscopy?
- b. How to control the new design's bending while the influence of different module orientations can be compensated for?
  - c. How to control the bending of the new design while compensating for different limited loads?

The size requirement is surveyed based on the practical MIS and NOTES surgery. The downscaled STIFF-FLOP design can be developed based on this size requirement to answer sub-question a. In order to assess the new design, system characterization experiment will be performed when the module of developed design is placed in vertical module orientation without load on the tip of the new design. The result of system characterization is utilized for feedforward controller, and a feedback controller is designed. The cooperation of feedback and feedforward controller will control the bending performance of the new design placed in vertical, inverted and horizontal module orientations for answering sub-question b. The load will be attached on the tip of the new design. Meanwhile, the same feedback and feedforward controller will be applied for testing the control performance under different load on the tip of the new design.

#### **1.4. Thesis Outline**

The limitations of current STIFF-FLOP design and the aim of this study were described in this chapter. A more detailed literature review on soft robotic endoscope will be introduced in chapter 2. In chapter 3, the new design and fabrication processes will be described. Chapter 4 will describe the system characterization experiment on the module of the new design and its results. In chapter 5, PID feedback controller is cooperated with feedforward controller which is based on the result of system characterization. The combination of two controllers will be applied in controlling the one-plane bending angle of the new design in vertical, horizontal and inverted module orientations. In addition, the same controllers will be applied in controlling the one-plane bending angle of the new design with limited load on the tip of it. In chapter 6, the conclusion of the bendability and controllability of the new soft robotic endoscope will be illustrated. The limitations of this study and expectation on the further direction will also be discussed in chapter 6.

---

## 2. Background

In this chapter, the practical MIS and NOTES surgeries are introduced. The mechanisms of soft pneumatic actuators, which are pneumatic networks, pneumatic artificial muscles and fiber-reinforced actuator, will be explained. Some state-of-art designs of soft pneumatic robotic endoscope will be presented. STIFF-FLOP manipulator is the most important design as the foundation to develop the downscaled design.

### 2.1. Introduction

Less incision will reduce the pain of patients and leave less trauma on the surface of skin, meanwhile the recovery time will also be reduced. That is why MIS and NOTES are becoming popular and replacing traditional open surgery. With the development of MIS and NOTES, the endoscope is used as a tool for surgical intervention.

Different from rigid endoscopes, a flexible endoscope is able to reach distant surgical target and circumvent a healthy organ. Examples shown in Figure 2.1 are implementations of soft robotic endoscope for laparoscopy and colonoscopy. There are many actuation mechanics for soft endoscope, such as shape memory alloy, tendon driven mechanisms, flexible fluidic actuators. Pneumatic soft actuator is designed based on the mechanism of flexible fluidic actuator. The elastomeric nature of soft robotic endoscope together with no requirement of electrical power makes it useful in the presence of electric and magnetic fields, i.e., Magnetic Resonance Imaging (MRI) compatible, which means the pneumatic soft robotic endoscope can be tracked by MRI bore [1]. In addition, pneumatic soft actuators have advantages like rapid reaction since air has low viscosity and can be moved rapidly, easily controlled and measured by regulators and sensors, universally available and easy to be discarded into the atmosphere [8]. In this chapter, several pneumatic actuators will be introduced. Then previous pneumatic soft robotic endoscopes will be reviewed.

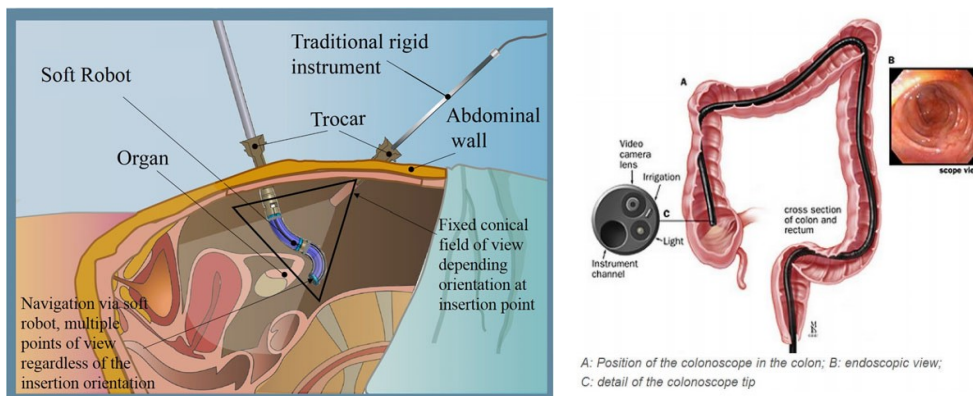


Figure 2.1 Illustration of soft robotic endoscopes implemented in MIS and NOTES application. (left) modular soft robotic endoscope is implemented in laparoscopy (MIS application) [9]. (right) soft robotic endoscope applied in colonoscopy (NOTES application)

### 2.2. Soft pneumatic actuators

*Pneumatic networks (Pneu-net):*

The Pneu-nets actuator consists of inflexible channels fabricated in an elastomeric material. This actuator comprises an extensible top layer and inextensible, but flexible, bottom layer which is shown

in Figure 2.2. The two inside walls of single chamber are designed to be thinner, and have greater surface area, than top wall. In this way, an increase of the internal pressure preferentially expands the inside walls and minimizes the strain that occurs on the other exterior walls. In addition, the expanding of inside walls pushes neighboring chambers against each other due to the close proximity of two neighboring chambers. The combination of these two phenomena results in the bending of the entire actuator and small changes in the height of extensible layer.

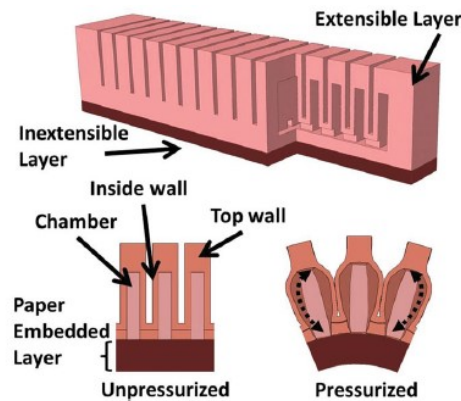


Figure 2.2 Pneu-net actuator designed by Bobak Mosadegh [8]

#### *Pneumatic Artificial Muscles:*

The pneumatic artificial muscle is also called McKibben actuator. It is composed of a chemical braided sleeve mesh and an inflatable elastic tube. As shown in Figure 2.3, the elastic tube is surrounded by the sleeve mesh. When air is input into the tube, it expands along the radial direction and contracts along the axial direction. This deformation terminates when the braided sleeve mesh reaches a specific braided angle.

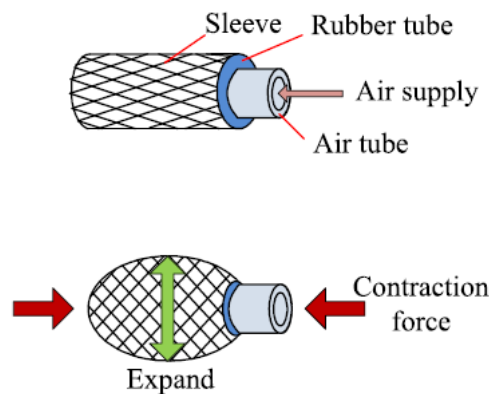


Figure 2.3 Structure and action of McKibben pneumatic artificial muscle [10]

#### *Fiber-reinforced actuator:*

The fiber-reinforced actuator performs bending due to the use of an inextensible layer in one side of the actuator. As shown in Figure 2.4, the continuum helical fiber reinforcement wraps around the outside wall of actuator, and blocks its radial expansion but permits the axial elongation. In this case, the bending performance results from the asymmetry in elongation caused by the inextensible layer in the bottom side. The actuator can be tuned to achieve a wide range of motions such as extension, expansion, twist and bending by varying the fiber angle and materials used. [11]

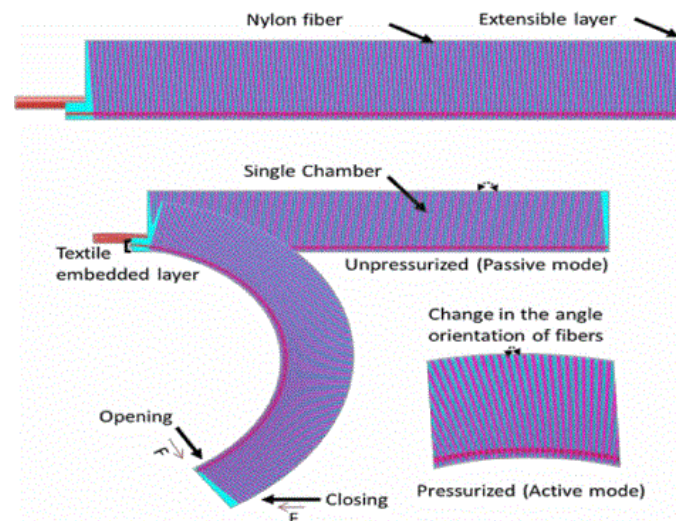


Figure 2.4 Structure of Fiber reinforcement actuator [12]

### 2.3. State-of-art designs of soft pneumatic endoscope

Soft pneumatic actuators are applied in the design of surgical endoscopes. In this session, several state-of-art designs of pneumatic soft robotic endoscope will be introduced.

#### 2.3.1. CMMPAM

The outer diameter of each McKibben actuator in CMMPAM (Continuum Manipulator actuated by McKibben pneumatic artificial muscle) is 2.6 mm. The weaving angle of each McKibben actuator is  $18^\circ$ . As shown in Figure 2.5, the length of the entire manipulator is 372mm. each joint of manipulator is connected by a double-layer flange plate which radius is 37.5 mm. A spring is designed to connect adjacent flange plates within each joint module to enhance the compliance and robustness of the entire manipulator. When the air pressure is applied, the actuator diameter increases and contraction force is generated which pulls the flange plate to bend the manipulator [10]. This design is not specified for MIS nor NOTE surgical applications due to its oversized shape. However, it completes expansion, contraction and three-dimensional movements with the error less than 7mm (the difference between desired value and the actual value). It also has the capability of varying stiffness. After the manipulator hits the obstacle, it can return to its original position and the maximal recovery error is 5.08 mm.

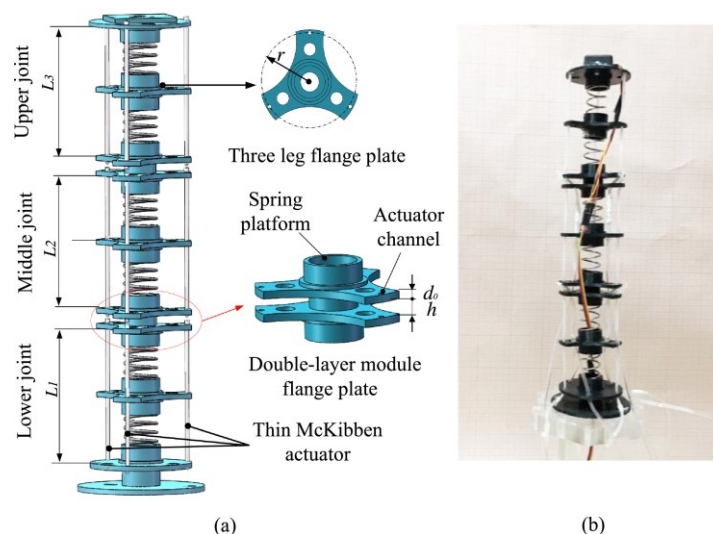


Figure 2.5 (a) schematic design of CMMPAM manipulator (b) prototype of CMMPAM manipulator.

### 2.3.2. Chip-on-tip endoscope

The Chip-on-tip endoscope is a one degree-of-freedom bending pneumatic endoscope. It consists of a CMOS camera and an elastic inflatable micro actuator with bending deformation showed in Figure 2.6 (a). The actuator is made by polydimethylsiloxane (PDMS) molding. It is able to bend  $160^\circ$  at a pressure loading of 250 kPa and exhibits a bandwidth of 14 Hz in air and 11 Hz in water. Due to the signal transferring cable through the channel of the actuator, the static bending performance of the actuator with CMOS camera is  $45^\circ$  at 280 kPa [13].

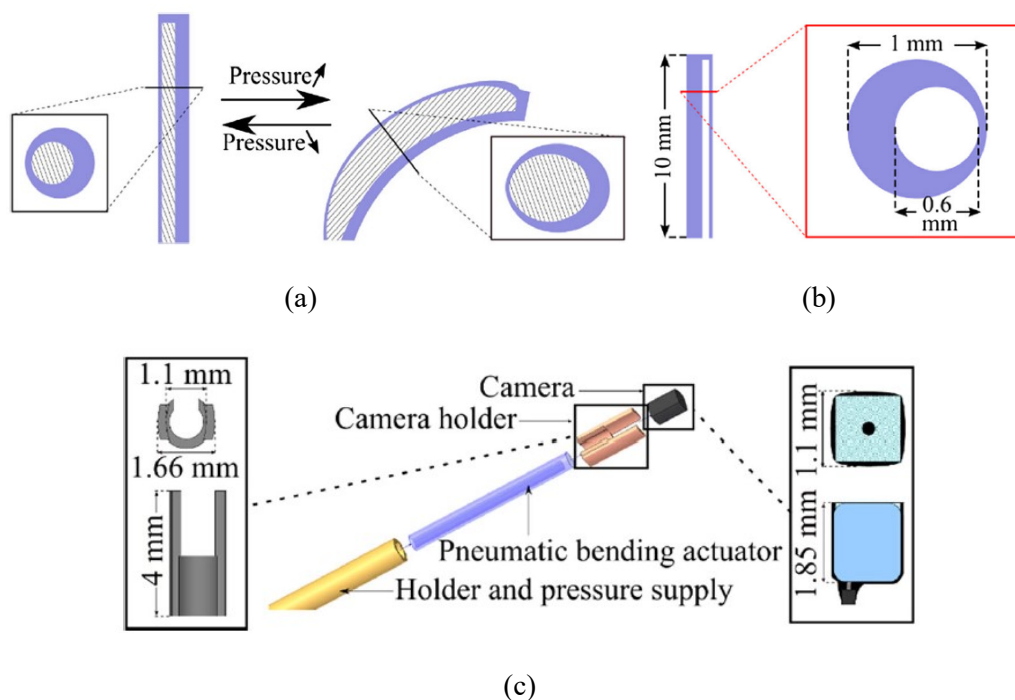


Figure 2.6 One degree-of-freedom chip-on-tip endoscope

(a) Schematic overview of the bending deformation of pneumatic bending actuator of chip-on-tip endoscope. (b) Overview of the dimension of pneumatic bending actuator with outer diameter of 1 mm, length of 10 mm, inner diameter of 0.6 mm and eccentricity of 0.14 mm. (c) Assembly of chip-on-tip endoscope with  $1.1 \times 1.1 \text{ mm}^2$  CMOS camera (NanEye, Awaiba) [13]

### 2.3.3. STIFF-FLOP surgical manipulator

STIFF-FLOP surgical manipulator is a modular manipulator designed for colonoscopy. In the structure shown in Figure 1.1 (a), three semi-cylindrical flexible fluidic actuators are equally spaced into the module in radial arrangement. The selective stiffness changing is implemented by granular jamming mechanism in the central channel. The main component of the manipulator is an elastomeric cylinder made by silicone (Eco-flex 0050-Smooth-on Inc). An external braided sheath is fixed at the distal ends of the cylinder to minimize the lateral expansion caused by the inflated chambers in all direction [3] shown in Figure 1.1 (b).

The STIFF-FLOP design contains several issues in sensing and actuation as a concept design. The use of external braiding directs the expansion of chambers in inward direction because the outward inflation of pressure chamber is constrained. This modifies the internal structure of the manipulator, and results in undesirable effects such as nonlinear actuation and different actuation performances between one chamber activation and two chambers activation [5]. These undesirable effects can be observed in Figure 1.2.

The new design of soft pneumatic endoscope is developed based on STIFF-FLOP design. Therefore, it is important to understand the actuation mechanism of STIFF-FLOP design.

STIFF-FLOP module can bend when one or two chambers are activated by air pressure. It can elongate in longitudinal direction when all three chambers are activated simultaneously. When single chamber is activated, the module will bend to the opposite direction of the activated chamber. When two chambers are activated with the same pressure simultaneously, the module will bend to the direction opposite to the central line between the two activated chambers.

As shown in Figure 2.7, the source of the deformation of the module is a bending moment caused by pressure-induced forces. Assuming that the pressure is constant at every point of the chamber volume, the value of internal force acting on a certain cross section center is calculated as:

$$F = PA \tag{1}$$

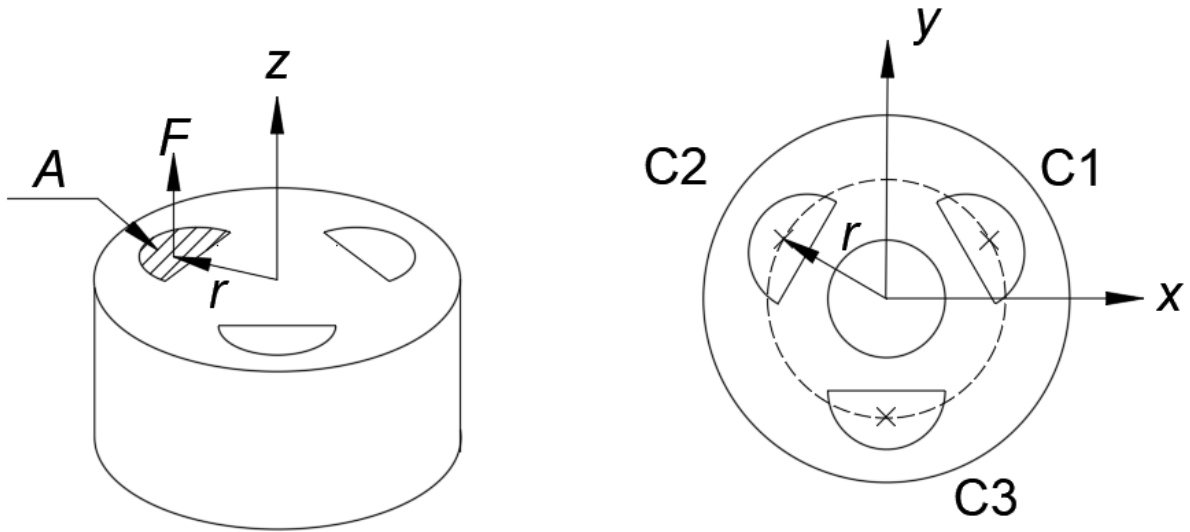


Figure 2.7 Cross section of STIFF-FLOP, perpendicular to the chamber axis

In this equation,  $F$  represents the pressure induced force acting on the center of the cross-section of the chamber. The direction of  $F$  is parallel with its  $Z$ -axis (perpendicular to the cross section).  $A$  represents the area of the cross section of the chamber.  $P$  is the input air pressure to the chamber. The value of  $F$  equals the scalar product of  $A$  and  $P$ .

Assuming that the dimension of the chamber and the pressure are constant throughout the module length along  $Z$ -axis, the force in the cross section is parallel with its  $Z$  axis, therefore the  $Z$ -axis moment is zero. The resulting moment of force causes pure bending of the module. The resulting moment is also constant due to constant chamber dimension and pressure. The resulting bending moment  $\vec{M}$  can be calculated using the force value and cross section geometry. Because the bottom of the module is fixed, the neutral point of the cross section of the module is located on the center of the geometry. The value of resulting bending moment equals the product of the force  $\vec{F}$  and the vector  $\vec{r}$  which is from the center of the module to the center of the chamber. It can be expressed as:

$$\vec{M} = \vec{r} \times \vec{F} \tag{2}$$

The bending moment resulting from activating two chambers simultaneously is presented in Figure 2.8. Labelling vectors from the center of the module to the centers of each chamber as  $\vec{r}_1$  and  $\vec{r}_2$ . The resulting bending moment can be expressed as:

$$\vec{M} = (\vec{r}_1 + \vec{r}_2) \times \vec{F}$$

Because chambers are in equally radial arrangement, the combination of bending moments of two chambers is the same as the bending moment of one chamber in value shown in Figure 2.8.1.

However, the external braided sheath only restricts the radial expansion of chamber away from the module center. No restriction is implemented to prevent the expansion of inflated chamber towards the module center, which changes the internal layout of the module. This causes the shift of chamber center and reduces the length of vectors from the center of the module to the center of chambers shown in Figure 2.8.2 [5].

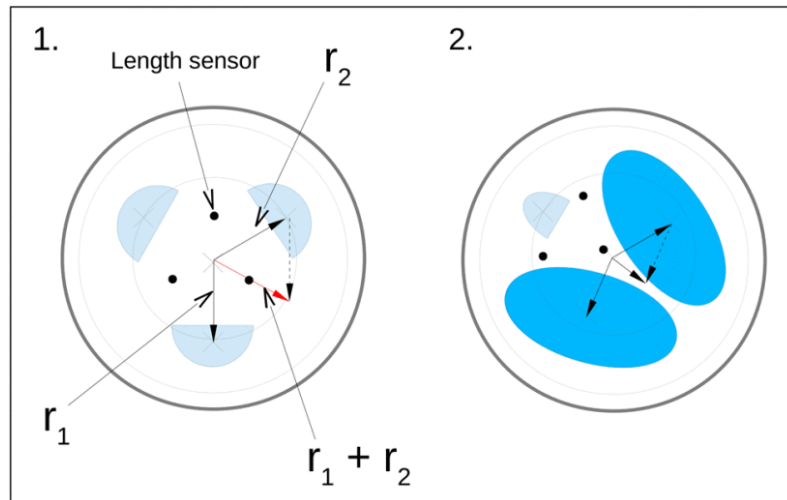


Figure 2.8 Chamber cross-section center shifts during two chambers simultaneous actuation.

(1) unactuated state. (2) the change of chamber cross-section shape causes the geometrical center shift and reduce the distance from module center. The resulting bending moment is reduced. [5]

The reduced bending moment when two chambers are actuated can also be observed in the experimental characterization of STIFF-FLOP design shown at Table 2.3. The maximum bending angle of one chamber actuation at 0.65 bar is 120°. There is a 40° reduction of the maximum bending angle of two chambers actuation at 0.65 bar.

Table 2-1 Active performance of STIFF-FLOP design [3]

STIFF-FLOP design	
<b>Max bending angle (one chamber @ 0.65 bar)</b>	120 deg
<b>Max bending angle (two chambers @ 0.65 bar)</b>	80 deg
<b>Max elongation (@ 0.65 bar)</b>	86.3%
<b>Max force (one chamber @ 0.65 bar)</b>	24.6 N
<b>Max force (three chambers @ 0.65 bar)</b>	41.4 N
<b>Max stiffness variation (@ base condition)</b>	36%

### 2.3.4. MOLLUSC Module

The STIFF-FLOP design has the issue that the bending moment of two chambers activation is smaller than one chamber activation. To solve this issue, MOLLUSC (multi-stiffness controllable endoscopic) module [2] is designed shown in Figure 2.9.

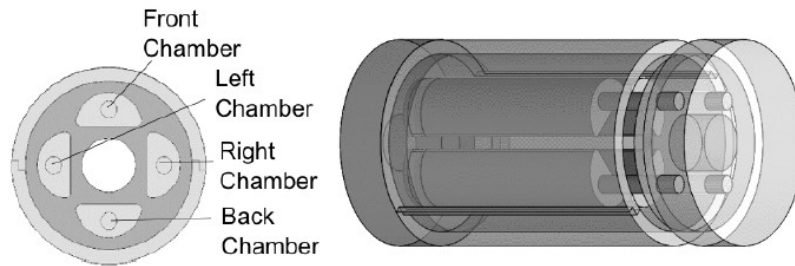


Figure 2.9 Design of MOLLUSC manipulator (left) top view of the mold, (right) side view of the mold [2]

As shown in Figure 2.10, four chambers are designed to exhibit an increase in the moment arm in case of two chambers activation. The angle distance between two adjacent chambers is  $90^\circ$ . Therefore, activating two adjacent chambers results in the moment arm of  $\sqrt{2} r$ . Although the chamber cross-section center is also shifted towards the center of the module, when two adjacent chambers are activated, the bending moment of MOLLUSC design is larger than that of STIFF-FLOP design. However, the increased number of chambers may result in a complex control system in hardware level.

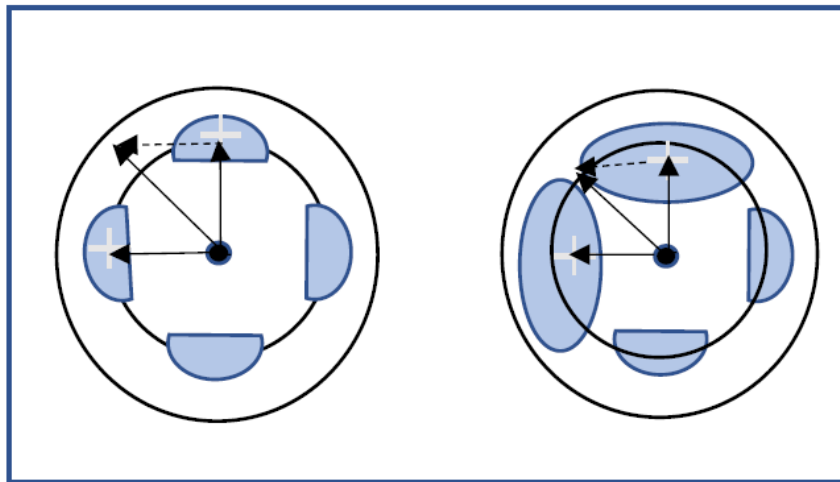


Figure 2.10 (Left) Unactuated state of MOLLOSC design. (Right) Cross-section shape when two chambers are actuated. The resultant cross-section center in MOLLOSC design is decreased, however due to the angle between two adjacent chambers is  $90^\circ$ , the resultant vector of two chambers activated simultaneously is  $\sqrt{2} r$

The change of cross-section area of chambers and the shift of chamber's geometry center are issues for designing a pneumatic soft robotic endoscope. This may cause the problem on controlling soft pneumatic endoscope. In designing a pneumatic endoscope module, methods should be developed to restrict the influence of the expansion of the cross-section area of chambers and the shift of the geometric center of chambers.

---

## 3. Design of downscaled pneumatic soft endoscope

### 3.1. Design requirements

The downscaled design is based on the STIFF-FLOP manipulator mentioned in the previous chapter. The objective is to design the pneumatic soft robotic endoscope for laparoscopic application. The new design was carried out considering the following requirements:

- a. The device has to be compatible with both standard trocars applied in laparoscopy and most natural orifice in NOTES applications in terms of dimension. Therefore, the diameter of the soft robotic endoscope should be less than 12 mm. Meanwhile, the lateral expansion of endoscope has to be avoided.
- b. The new design should be able to adjust the position and direction of the end effector, when the base is kept stationary, thus it should realize omnidirectional bending and the capability of elongation.
- c. A free central channel of about 4 – 5 mm is required for feeding surgical tools e.g. camera fixed at the end effector, graspers and electric wires.

### 3.2. Survey of the design requirement on size

A series of instruments, implemented in the current MIS and NOTES applications, are investigated in terms of dimension for downscaling STIFF-FLOP design. In MIS applications, soft robotic endoscopes are inserted into patient's body through trocars. The size of trocars is considered as the most important dimension parameter to design new soft robotic endoscope. For NOTES applications (oral, rectal, vaginal, vesical etc.), camera size and natural orifice size are two limiting factors for downscaling STIFF-FLOP design.

#### 3.2.1. MIS application

*The standard diameter of trocars utilized for minimally laparoscopy is 5mm, 10mm and 12 mm [14].* Based on the size of current trocars, the soft robotic endoscope should be designed smaller than 12 mm. In the field of laparoscopy, as shown in Figure 2.1, a two-module soft robotic endoscope is designed with 14.5 mm in outer diameter. In the field of brain tumor surgery, a flexible mesoscale MRI-Compatible Neurosurgical Continuum robot is designed to be 12.6 mm in diameter and 60 mm in length [15]. For appendectomy, three trocars are implemented which diameters are 5 mm, 5mm and 10 mm separately, while for colectomy, four trocars are applied which diameters are 5mm, 5mm, 10mm and 10mm separately [16].

The camera module in the design of Abidi [9] is 3mm in diameter. The free central channel should be larger than the diameter of the camera. In the design of Bernth [17], the miniature USB camera is 6mm in diameter.

#### 3.2.2. NOTES application

The segments of colon have different dimensions which are presented in Figure 3.1. As shown in Table 3.1, *the narrowest of colon is Sigmoid which diameter is around 26 mm.*

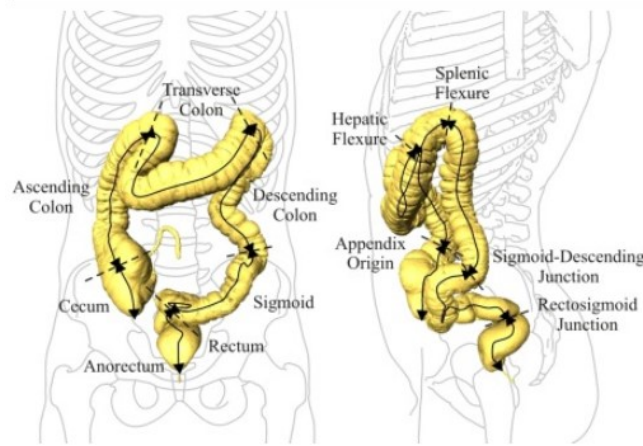


Figure 3.1 Schematic representation of the colonic segments and landmarks [18]

Table 3-1 Comparison of the colonic segmental diameter in supine and prone orientations in 24 patients (mean ± SD (median)) [18]

	Diameter, cm		
	Supine	z-value (p)	Prone
<b>Rectum</b>	3.6 ± 0.8 (3.4)	-1.400 (0.166)	3.7 ± 0.7 (3.6)
<b>Sigmoid</b>	2.6 ± 0.4 (2.5)	-1.263 (0.214)	2.6 ± 0.3 (2.6)
<b>Descending</b>	3.3 ± 0.6 (3.3)	-1.072 (0.294)	3.2 ± 0.5 (3.1)
<b>Transverse</b>	3.7 ± 0.4 (3.7)	-2.030 (0.042)	3.6 ± 0.5 (3.5)
<b>Ascending</b>	4.5 ± 0.7 (4.7)	-2.359 (0.017)	4.3 ± 0.7 (4.6)
<b>Cecum</b>	4.4 ± 0.7 (4.5)	-3.187 (0.001)	3.8 ± 0.6 (3.9)
<b>Proximal colon</b>	4.2 ± 0.4 (4.3)	-3.514 (0.000)	3.9 ± 0.5 (4.0)
<b>Distal colon</b>	3.1 ± 0.5 (3.0)	-4.286 (0.000)	3.1 ± 0.4 (3.1)
<b>Total colon</b>	4.7 ± 0.5 (4.7)	-4.286 (0.000)	3.5 ± 0.4 (3.5)

### 3.3. Design modification

#### 3.3.1. Single Segment Model based on Constant Curvature model

Constant curvature model is applicable in case of external forces having zero value. By this model, the relationship between bending angle and the value of air pressure can be evaluated. The applicability of constant curvature assumption in the downscaled design will be examined using the physical prototype in chapter 4. In this chapter, the analytical relationship between bending angle and input pressure will be derived by constant curvature assumption (Fraś et al., 2014) [7].

As discussed in chapter 2.3.3 and referring to Figure 2.7, it is assumed that the shape of the chamber and the pressure in the chamber are constant throughout the module length. According to equation (1) and (2), the value of pressure-induced force  $F$  is proportional to the input air pressure  $P$ . Due to the direction of pressure induced force is perpendicular to the vector from the center of the structure to the center of the chamber, the value of bending moment  $M$  is equivalent to the scalar product of pressure induced force  $F$  and length of vector  $r$ .

$$F = PA \tag{3}$$

$$M = Fr = PAr \quad (4)$$

The Euler-Bernoulli formula relates the bending moment with resulting curvature as follows [7]:

$$\kappa = \frac{1}{\rho} = \frac{M}{EI} \quad (5)$$

where  $E$  is the Young's modulus constant of silicone, and  $I$  is the second moment of inertia of the module at the cross-section respect to the neutral point.  $\kappa$  is the curvature of the module. It is shown in Figure 3.2 that  $\kappa$  is represented as the inverse of the radius of the module circle  $\rho$ .

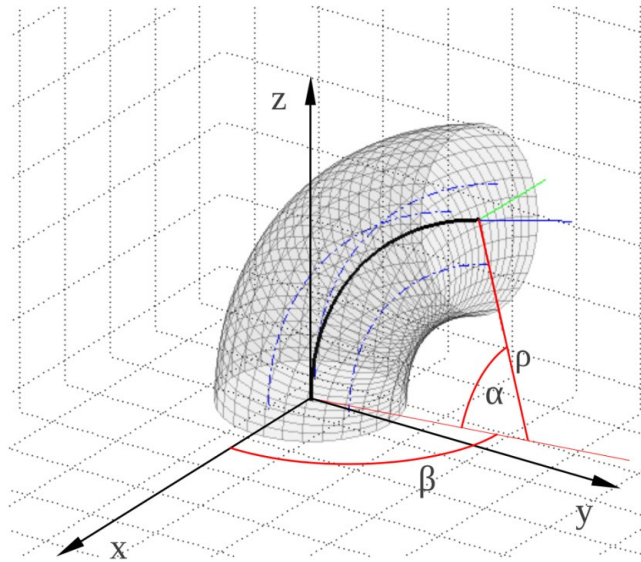


Figure 3.2 Module bending with no presence of external force.  $\rho$  is the radius of the curvature, and  $\alpha$  is the bending angle.  $\beta$  is the direction of module.[7]

Assuming no presence of external forces, the bending moment has the same value at every cross section along its  $Z$ -axis. Therefore, the total curvature can be calculated as:

$$\nabla_k \kappa_k = \kappa_0$$

$$\kappa_0 = \frac{M_0}{EI}$$

$k$  represents the number of cross-section structure of the module along its  $Z$ -axis.

In constant curvature case shown in Figure 3.2, the position and the shape of the module are described with only three parameters: the bending angle  $\alpha$ , direction  $\beta$  and radius  $\rho$ . Along the module's axis, the elongation at any point can be described by Hooke's Law:

$$\Delta dl = \frac{F_p}{A'E} dl$$

Where  $F_p$  is the overall force resulting from chamber pressures, at single cross-section. It is calculated by adding forces resulting from each chamber pressure.  $A'$  is the cross section area of the silicone part (cross section area of the module minus the area of three chambers). Figure 3.3 presents the elongation of a fragment of the module by chamber pressures.

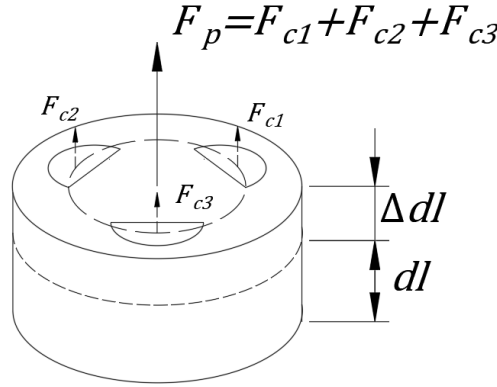


Figure 3.3 Elongation of a fragment of the module

The overall change of the module length can be calculated by integrating the elongation of a fragment of the module from 0 to  $l_0$  (the total length of the module):

$$\Delta l = \int_0^{l_0} \Delta dl = \int_0^{l_0} \frac{F_p}{A'E} dl = \frac{F_p}{A'E} \int_0^{l_0} dl = \frac{F_p l_0}{A'E} \quad (6)$$

It is presented in Figure 3.4 that the elongation of the module can result in the change of the bending angle. The value of bending angle  $\alpha$  can be evaluated by integrating the curvature from 0 to  $l_0 + \Delta l$ :

$$\alpha = \int_0^{l_0 + \Delta l} d\alpha = \int_0^{l_0 + \Delta l} \frac{1}{\rho} dl = \frac{1}{\rho} (l_0 + \Delta l) \quad (7)$$

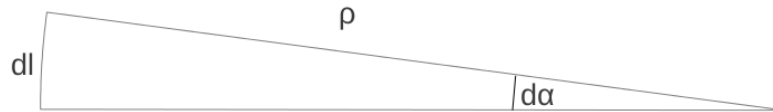


Figure 3.4 Bend of the module at a point along its axial direction [7]

With the combination of equation (3), (4), (5), (6) and (7), the relationship between bending angle and air pressure can be evaluated as:

$$\alpha = \frac{1}{\rho} (l_0 + \Delta l) = \frac{M}{EI} \left( l_0 + \frac{F_p l_0}{A'E} \right) = \frac{P^2 A^2 r l_0}{A'E^2 I} + \frac{P A r l_0}{EI} \quad (8)$$

### 3.3.2. Design objective

The design target is to achieve the maximal range of bending angles, which the new soft robotic endoscope can reach, with the fixed structure and dimension. The Young's modulus  $E$ , length of the vector  $r$ , the cross-section area of the module,  $A + A'$ , are constant if the structure and the dimension of the new design is determined. It is undesirable to apply high air pressure to achieve the desired bending angle. In this case, with constant air pressure, the new design is required to have maximal bending angle. Based on Equation (8), with constant air pressure, the increase of chamber's cross-section area  $A$  will lead to the increase of the bending angle that the new design can reach. For this reason, the design objective can be transformed into maximizing the chamber's cross-section area.

### 3.3.3. Design improvements

Based on design requirements and the survey of instruments in MIS and NOTES surgery on size, it is determined that the external diameter of the new design is 11.5 mm, driven by requirements of trocar

size. Meanwhile, considering the dimension of camera, the new design should have a free central channel with 4.5 mm in diameter to contain 3mm miniature camera.

With the fixed dimensions of external diameter and internal central channel, the space for chambers configuration is limited. Three-chamber configuration, which is the same as STIFF-FLOP module, is applied instead of four-chamber configuration, like MOLLUSC design. The application of four-chamber configuration will reduce the cross-section area of each chamber when the limited space is fully exploited. In addition, it is enough for three chambers to achieve omni-directional bending. Four-chambers configuration will also lead to a complex control system in aspect of hardware.

#### *Primary design:*

The primary design is shown in Figure 3.5. This design is inspired by Fras, J [5]. The chamber in primary design is designed as the cylindrical instead of semi-cylinder because the chamber behavior during actuation will aim to maximize its cross-section area, and will finally reach a circular cross section shape without any external constrains [5]. The braiding is employed around each individual chamber in the form of tight helical threading, instead of constraining the external expansion of the entire design by one external sheath. This solution allows for the expansion of chamber along longitudinal direction, but blocks the radial inflation. It has been proved that the internal braiding around each chamber is able to reduce the non-linear actuation effect of STIFF-FLOP design [5].

Since the braiding is 0.5 mm in thickness and it is embedded in the body of the primary design. The maximal diameter of each chamber is 1.5 mm. The cross-section area of each chamber is  $1.76 \text{ mm}^2$ , while the cross-section of silicone part is  $82.66 \text{ mm}^2$  which means the primary design does not exploit the source of cross-section area sufficiently. For this reason, the secondary design aims to enlarge the cross-section area of single chamber.

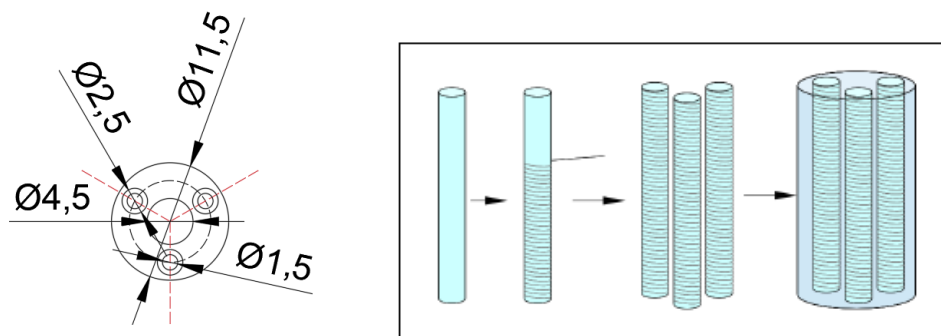


Figure 3.5 Primary design of downscaled STIFF-FLOP manipulator inspired by Fras, J [5]. (Left) The dimension of primary design. (Right) Chamber braiding concept [5]

#### *Secondary design:*

The secondary design is shown in Figure 3.6. It is inspired by Abidi, H [9]. Since it is impossible to enlarge the diameter of the cylindrical chamber, one method to increase the cross-section area of chamber is to increase the number of chambers. Six chambers constitute the secondary design. Three pairs of chambers are lined with a minimum-pitch thin inextensible thread in a tight helical winding. There are a couple of chambers for each bending motion parameter (MP).

Compared with primary design, this double-cylinder configuration increases the bending force by a factor of two. The cross-section area of the chamber for each MP is  $3.52 \text{ mm}^2$ , which is twice as large as the primary design.

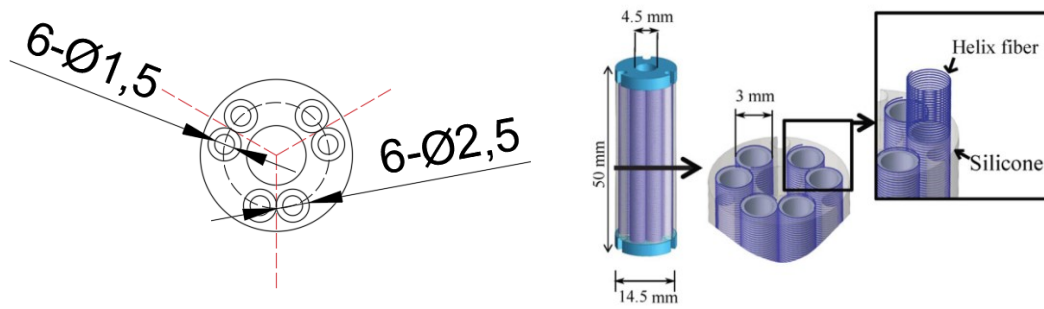


Figure 3.6 Secondary design of downscaled STIFF-FLOP manipulator (Left) The dimension of secondary design. (Right) Illustration of the design of Abidi, H [9]

### Third design:

The third design increases the number of chambers with a step further to exploit the source of cross-section area. As shown in Figure 3.7, the third downscaled design consists of 9 chambers. Compared with secondary design, the third design increases the cross-section area of chambers for each MP in a step further. A set of triple cylinder configuration is able to achieve  $5.25 \text{ mm}^2$  cross-section area for each MP. It can be observed that in the third design the number of chambers is saturated, and it is impossible for the module to contain more than 9 chambers.

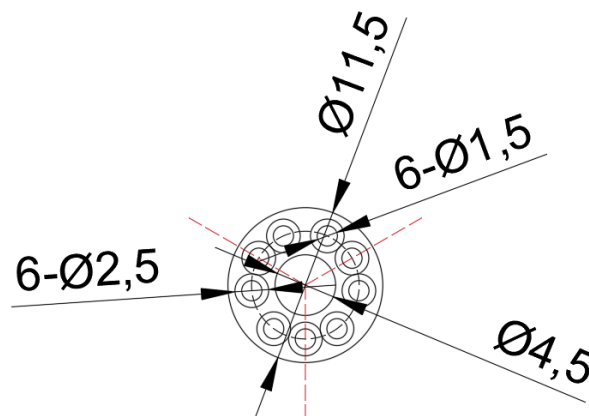


Figure 3.7 Third design of downscaled STIFF-FLOP manipulator. Three chambers constitute one MP.

### Final design:

In previous designs, due to the thickness of the helical threading is 0.5 mm, the minimal radial distance from the helical braiding to both external and internal edges is also 0.5 mm. If the braiding can be implemented at both external and internal edges of the module, and the thickness of the chamber wall is only 0.5 mm, the radial expansion of inflated chambers can also be restricted.

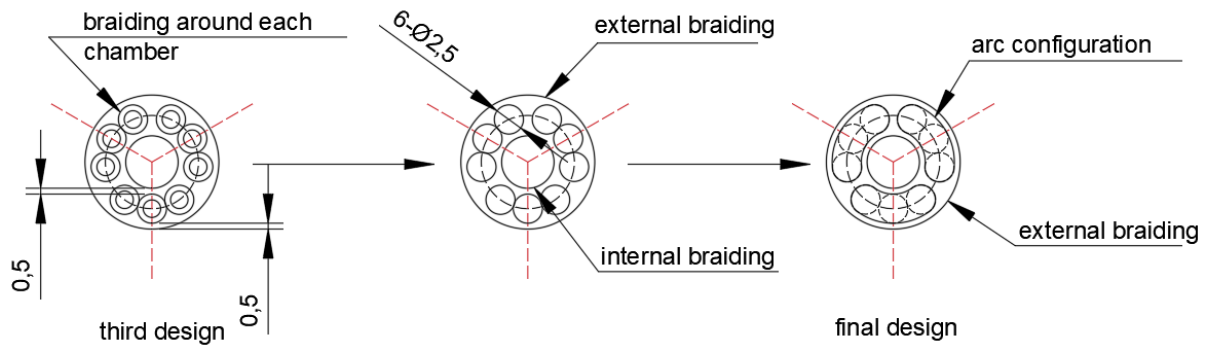


Figure 3.8 Improvement from triple-cylinder configuration to arc configuration.

As shown in Figure 3.8, the diameter of single chamber is increased to 2.5 mm so that the minimal thickness of wall between chamber and both internal and external edges is 0.5 mm. In this case, the braiding is implemented around the external and internal edges of the structure to restrict the radial expansion of the chamber. Without the braiding around each chamber, triple-cylinder configuration has the sharp edge between two adjacent chambers and the non-uniform thickness of chamber wall. To solve these issues, triple cylinders are combined and formed an arc configuration shown in Figure 3.8. The arc configuration has uniform thickness of chamber wall which is 0.5 mm and includes no sharp edges. Another advantage of arc configuration is increasing the cross-section area of chamber for each MP. The cross-section of arc chamber for each MP is  $17.6 \text{ mm}^2$ . In addition, in practical application of downscaled soft endoscope, it is proposed to pass instruments through the central channel. These instruments are assumed incompressible in the radial direction but bendable. That means when the downscaled design is filled with instruments, the internal braiding can be removed due to that the radial expansion of inflated chamber towards the center of the structure can be blocked by the incompressible but bendable instruments.

The performance comparison between primary design, secondary design, third design and final design are summarized in Table 3.2. The final design shown in Figure 3.8 will be fabricated and studied in the following chapters. The dimension and structure of the final design are illustrated in Figure 3.9. The final design consists of three arc chambers which are spaced equally in radial arrangement. Each arc chamber is for one MP of the final design. The cross-section area of each arc chamber is  $17.6 \text{ mm}^2$ . It is noted but not mentioned in Figure 3.8 that the minimal distance between two adjacent arc chambers is 0.78 mm which means there is no space for extending the cross-section area of the chamber. Therefore, arc configuration meets the design requirement of maximal cross-section area of chamber.

Table 3-2 Performance comparison between primary design, secondary design, third design and final design

Name of design	Indication	Improvement	Disadvantage
STIFF-FLOP design	a. External braided crimped sheath b. External diameter of 25 mm c. Semi-circular chambers	a. Suitable for colonoscopy in terms of dimension b. Stiffness adjustable c. Traceable in MR core	a. Not applicable for laparoscopy b. Non-linear actuation
Primary design	a. Braiding around each individual chamber b. 11.5 mm in external diameter c. Cylindrical chambers	a. Downscaled STIFF-FLOP design for laparoscopy b. Linear actuation	a. Cross-section area for each chamber is only 1.76 mm <sup>2</sup> .
Secondary design	a. Double-cylinder chamber configuration b. Six chambers for three MPs	a. Bending force increased by a factor 2 compared with primary design b. 3.52 mm <sup>2</sup> chamber cross-section area for each MP	a. Source of transversal cross-section area not exploited sufficiently
Third design	a. Triple-cylinder chamber configuration b. Nine chambers constituting three MPs	a. 5.25 mm <sup>2</sup> chamber cross-section area for each MP b. Source of cross-section area fully exploited	a. Complex fabrication processes b. Sharp edge between two adjacent chambers c. Non-uniform thickness of chamber walls
Final design	a. External braided sheath b. arc chamber configuration	a. Simplified fabrication processes b. 17.6 mm <sup>2</sup> chamber cross-section area for each MP	

It is shown in Figure 3.9 that the total length of the final design is 50 mm and the external diameter is 11.5mm. This size makes the final design suitable for both laparoscopy and colonoscopy. Three arc chambers are 30 mm in length. Chambers are covered by two cylindrical parts at both ends of the entire design. The bottom part contains three pneumatic tubes with 2.2 mm in diameter. These pneumatic tubes are for actuating chambers by air pressure. The radial expansion of the module will be limited by an external braided sheath, and the internal instruments which are incompressible but bendable. No internal braiding is implemented.

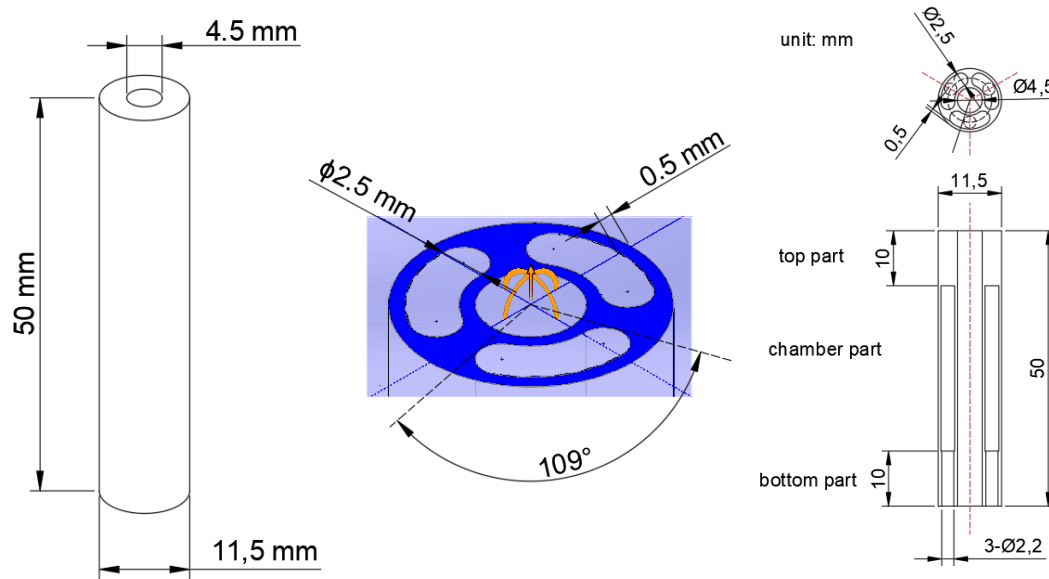


Figure 3.9 Design of a single module. Illustration of the module design: main dimensions, view of the structure of the internal chambers, main dimensions from top view and front view

Based on Equation (8), when the structure of the final design is determined, the relationship, between the bending angle and the air pressure distributed in the chamber, can be calculated. The numerical values of symbols in Equation (8) are listed in Table 3.3. The calculated analytical model of the final design, representing the relationship between the bending angle and the input air pressure, is shown in Figure 3.10.

Table 3-3 Numerical values and meaning of symbols of the final design in Equation (8)

Symbol	Meaning	value
$E$	Young's modulus	$0.0827 \text{ N/mm}^2$
$A$	Cross-section area of single arc chamber	$17.6 \text{ mm}^2$
$A'$	Cross-section area of the silicone part	$35.16 \text{ mm}^2$
$r$	Length of vector	12 mm
$l$	Length of module	50 mm
$I$	second moment of inertia	$1717.083 \text{ mm}^4$

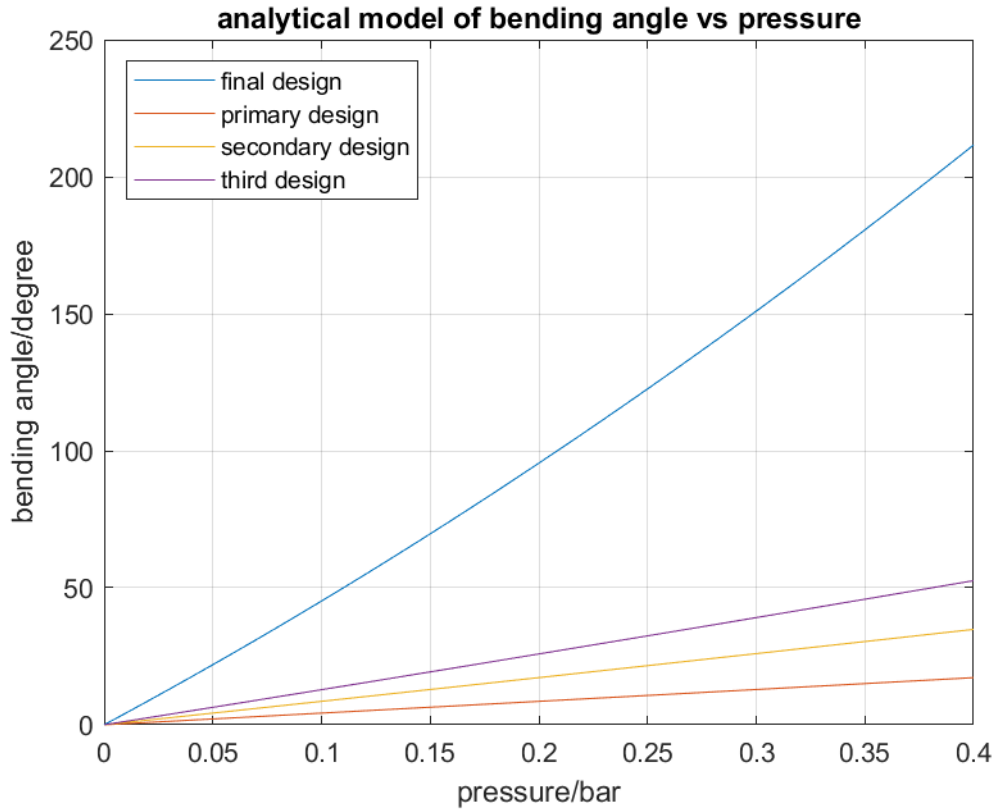


Figure 3.10 Analytical model of the new design in bending angle versus air pressure

### 3.4. Fabrication

In this section, the material of the final design and the molding of fabricating the single module will be discussed. Then the fabrication of the external braided sheath and assembling of each elements of the final design will be explained.

*Robot body fabrication:*

The molds shown in Figure 3.11 are printed by 3D printer. The printing material and molding process for each mold is referred in Table 3.4. The molding processes are displayed in Figure 3.12. Release agent is sprayed to the surface of molds to avoid the elastomer sticking hard to molds at removal process.

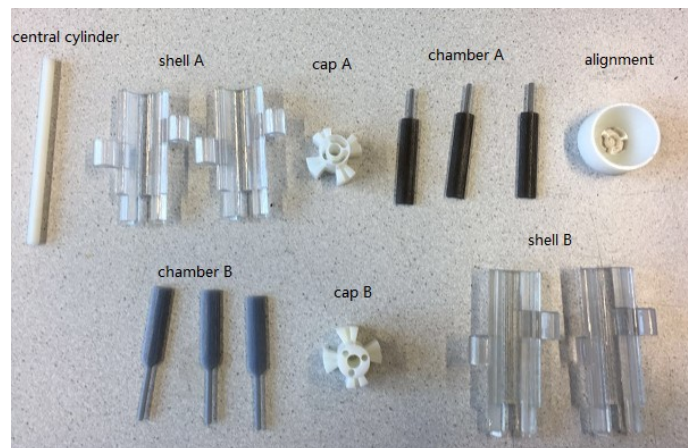


Figure 3.11 Molds of pneumatic soft robotic endoscope. Top: from left to right: central cylinder, shell A, cap A, chamber A, alignment. Bottom: from left to right: chamber B, cap B, shell B

*Table 3-4 Material of molds in corresponding molding processes*

Mold name	polyer name	elasticity modulus	molding process
Central cylinder	Verowhite	2,000 – 3,000 MPa	(a),(b),(d)
Shell A	Veroclear	290,000-435,000 psi	(a),(b)
Cap A	Verowhite	2,000 – 3,000 MPa	(a),(b)
Chamber A	Agilus Black, Veroclear	unknown	(a),(b)
Alignment	Veroclear	290,000-435,000 psi	(a),(b)
Chamber B	Agilus Black, Veroclear	unknown	(c),(d)
Cap B	Verowhite	2,000 – 3,000 MPa	(d)
Shell B	Veroclear	290,000-435,000 psi	(d)

The chamber part of the new design is made from silicone (EcoFlex 0050, Smooth on Inc). The raw material will be vacuumed for about 5 minutes until all air bubbles are removed. Finally, this material will be poured into the combinations of molds slowly to form the elastomer.

It is shown in Figure 3.12 that the molding process can be divided into four part. The chamber part of the new design is fabricated in step (a). The bottom part of the new design is fabricated in step (b). Step (c) and step (d) are for fabricating the top part of the new design. Finally, all molds will be removed from the elastomer of the new design. The detailed illustration of fabrication processes can be referred in Appendix A.3. The material of each part of the new design is shown in Table 3.5.

*Table 3-5 Material of each part of new design*

part	material	Young's modulus
chamber part	Eco-Flex 0050	12 psi
top part	Dragon Skin 10	22 psi
bottom part	Dragon Skin 10	22 psi
central channel	Dragon Skin 10	22 psi

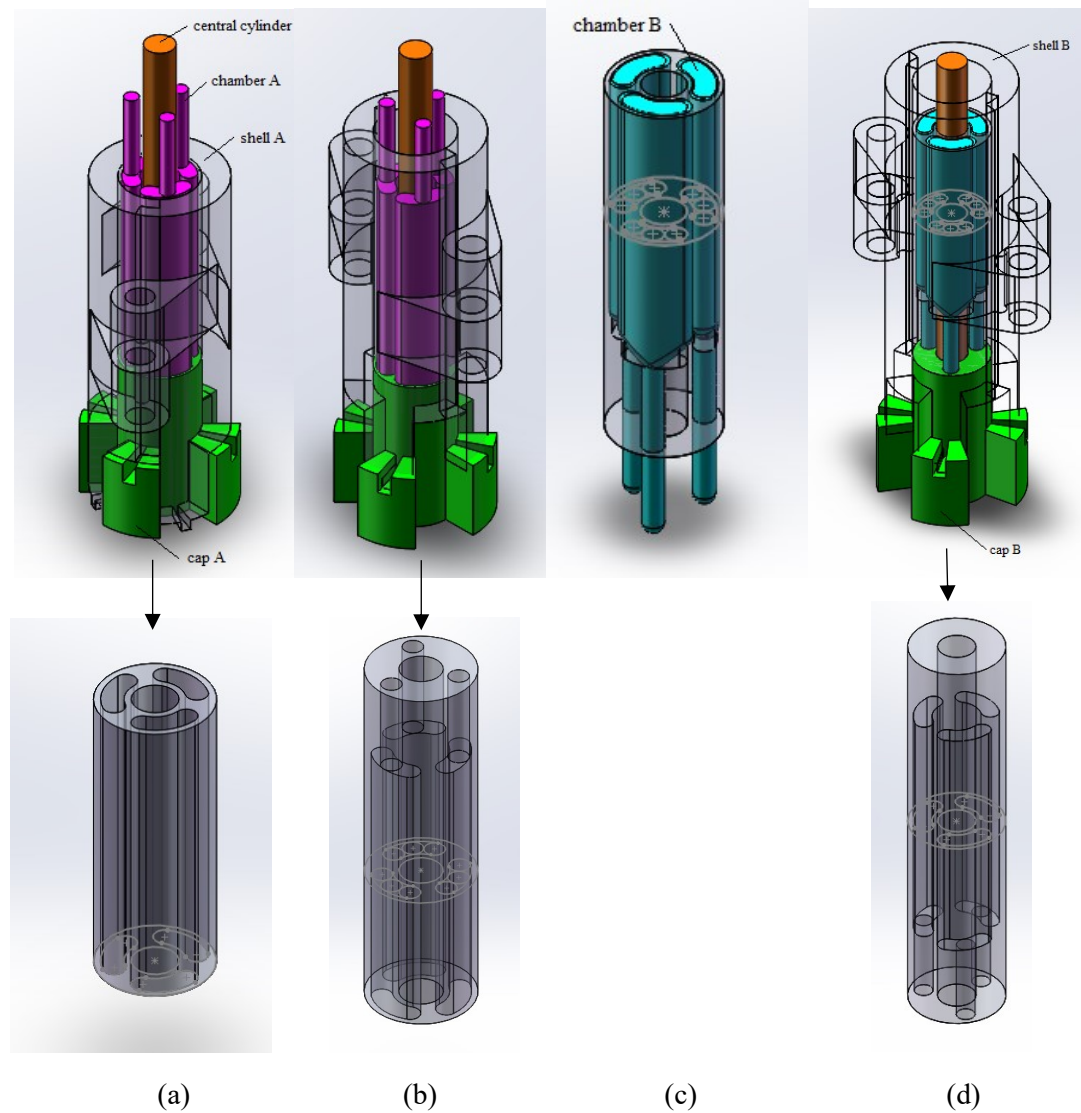


Figure 3.12 Molding processes of downscaled STIFF-FLOP design. (a) fabrication of chamber part. (b) bottom part molding. (c) Three chamber A molds are replaced by three chamber B molds. (d) Top part molding

#### External braided sheath:

To fabricate external braided sheath, the braided sleeve with diameter of 5mm (Farnell 1297224), shown in Figure 3.13 (a), is inserted by a  $\varnothing 12\text{ mm}$  metal cylinder shown in Figure 3.13 (c). This sleeve is pushed down until the fiber angle is  $0^\circ$ . Then the structure is hardened under the air flow with high temperature generated by the heat gun shown in Figure 3.13 (b). In this step, the heat gun is located around 90 cm away from the structure to make sure that the sleeve is hardened but does not melt. The influence of the length of the braided sheath on the bending performance of the module can be referred in Appendix A.1.

#### Assembling components:

As shown in Table 3.5, to simulate the instruments inside the central channel of module, the central channel is filled with Dragon Skin 10. Pneumatic tubes ( $\varnothing 2\text{ mm}$ ) are wiped by plastic glue (Loctite 406, Loctite.inc), and then they are inserted into the new design from the bottom part. The part of pneumatic tubes which are inserted into the new design is around 10 mm in length. The braided sheath is then put

on from the top of the module. At both ends of the module, it is fixed by plastic glue. The complete single module of the new design is shown in Figure 3.13 (d).

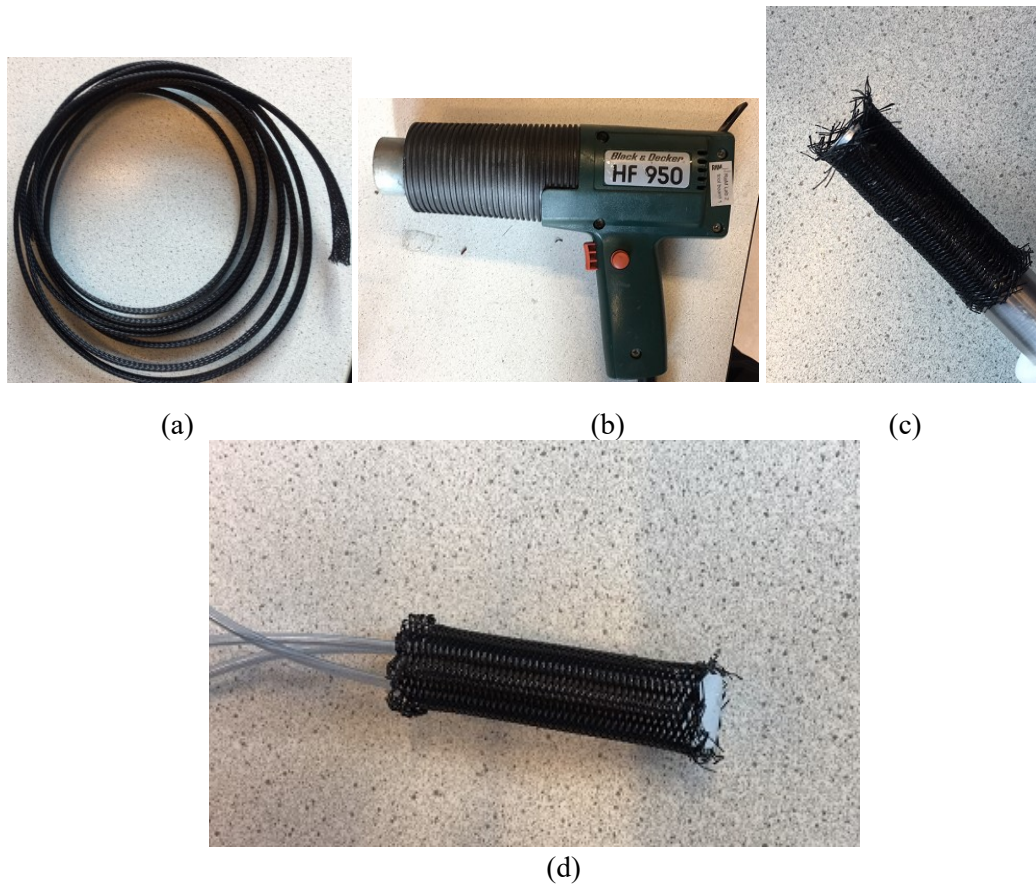


Figure 3.13 (a) braided sleeve with diameter of 5mm (Farnell 1297224). (b) the heat gun to harden the structure (c) the sleeve is pushed down until the crimped structure is formed. (d) Complete integration of module

### 3.5. Discussion and conclusion

In this chapter, based on the literature survey on requirements in terms of size, the dimension of the new design is determined. The diameter of the new design is 11.5 mm, while the length of the new design is 50 mm. It has a central channel which is 4.5 mm in diameter for instruments to pass through.

The analytical model between bending angle and air pressure is derived based on constant curvature model with Euler-Bernoulli formula and Hooke's Law. In this analytical model, the bending angle is the addition of a quadric part of pressure and a linear part of pressure.

The design objective is to achieve the downscaled STIFF-FLOP design with maximal bending ability in a fixed dimension and structure. This design objective is translated into obtaining the maximal cross-section area of chamber. Four proposed designs are developed and the design with arc chamber configuration is selected as the final design. The cross-section area of each arc chamber in the final design is  $17.6 \text{ mm}^2$ , which totally exploits the limited source of the cross-section area. The analytical model of the final design presents the maximal bending ability among four proposed designs.

The fabrication process contains four molding steps for the elastomer, assembling pneumatic tubes and fixing the external braided sheath at both ends of the new design. In the following chapters, the final design will be referred as the new design and the bending ability will be examined.

---

## 4. Characterization of a single soft pneumatic module

After the development of the new pneumatic soft robotic endoscope, the module of the new design is characterized in terms of the bending angle.

### 4.1. Aim of experiment

The research question on how to downscale STIFF-FLOP manipulator for laparoscopic application has been answered in chapter 3. In this chapter, the bending ability of the new design will be tested by system characterization experiment.

As discussed in chapter 3, the module of the soft pneumatic endoscope can be characterized by three parameters which are: one-plane bending angle  $\alpha$ , out-of-plane angle  $\beta$  and the curvature  $\kappa$ . In this project, the out-of-plane angle is not considered. The system characterization of the module in this article only refers to the relationship between the one-plane bending angle and the input pressure. This relationship is achieved by recording the input air pressure and corresponding one-plane bending angle simultaneously. The system characterization of the module will be utilized for the feedforward controller to control the bending performance of the new design in the next chapter.

It is assumed that the new design is compliant with constant curvature model which means the new design has constant radius of curvature all along the central axis. The bent configuration of the new design, under different air pressures, will be captured by a camera. Image processing will be used for obtaining the estimated backbone curvature with constant radius. The correctness of constant curvature assumption will be examined by comparing estimated backbone curvature with the physical backbone curvature.

In addition, the elongation capability of the new design will be assessed by recording the relationship between elongation of the new design and the input pressure.

### 4.2. Experiments setups

In this section, the setup for the system characterization experiment will be explained in details. Then the methodology of experiment will be described. The test protocol of the system characterization experiment will also be indicated in this section.

#### 4.2.1. Equipment

*Coil sensor for recording bending angle:*

The coil sensor (Aurora 5DOF sensor 610090) implemented is shown in Figure 4.1. The dimension of coil sensor is 0.8 mm  $\times$  11 mm. This dimension determines that the weight of the coil sensor is negligible compared to the new design. It means when the coil sensor is located on the tip of the new design, shown in Fig.4.2, there is no external force on the new design, which is compliant to the condition of constant curvature model. When the coil sensor is placed in a low-intensity, varying electromagnetic (EM) field, the voltage will be induced. The value of induced voltage is related to the position and Euler angles of the coil sensor.

The x-y-z position, yaw and pitch of the coil sensor is reported. However, the roll of the coil sensor is unavailable. If the bending moment of the new design is along the X-axis or Y-axis in a fixed coordinate system, then the yaw and pitch of the coil sensor are able to indicate the bending angle of the new design. As shown in Figure 4.2, the Z-axis of fixed coordinate system is in vertical direction. For obtaining the bending angle of the new design, the base of the new design is fixed at x-0-y plane so that the

longitudinal axis of the new design is along Z-axis. This is defined as the vertical module orientation in this project. When the new design is activated by air pressure, the bending moment will be along X-axis or Y-axis. In this module orientation and coordinate system, the value of the bending angle can be calculated by using only the yaw and pitch of the coil sensor.

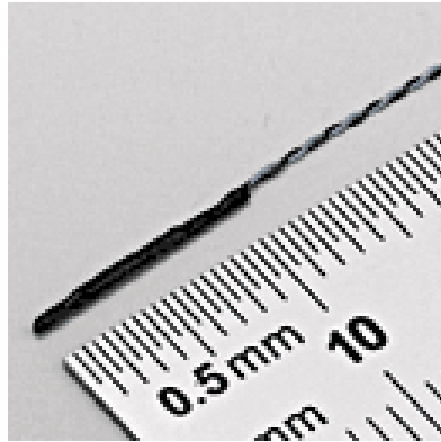


Figure 4.1 The dimension of the coil sensor (NDI medical). Due to the size of coil sensor is only 0.8 mm x 11 mm, no external force is on new design caused by the weight of coil sensor.

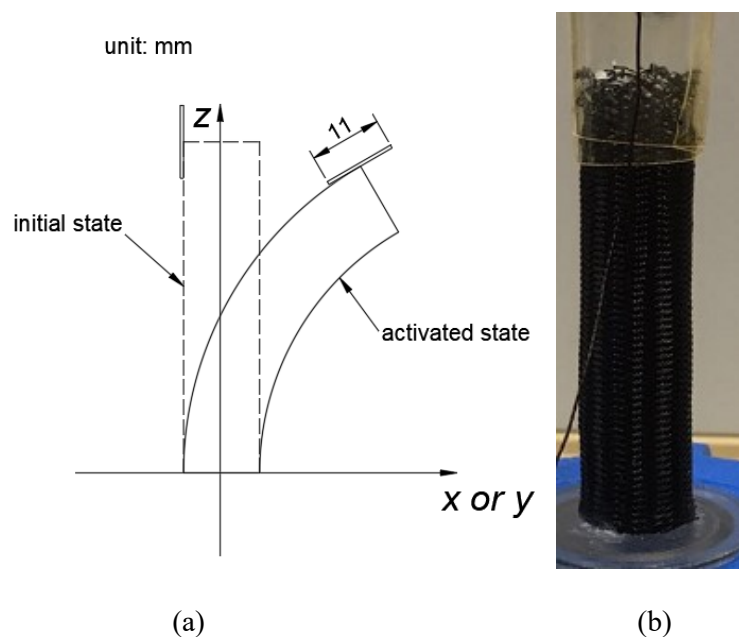


Figure 4.2 (a) Initial state and activated state of new design in vertical module orientation. The bending moment of new design along Z-axis is 0. (b) The coil sensor is attached to top end of the module with double layer tape

*Pressure regulator (Festo):*

The input pressure is generated and adjusted by a digital regulator (Festo) shown in Figure 4.3. This regulator connects the main pressure line in the lab and the chamber. It contains an internal controller to regulate the output pressure based on the input analog voltage. In the system characterization experiment, the maximum air pressure that pressure regulator can provide is 1.0 bar.



Figure 4.3 Digital pressure regulator (Festo)

*Pneumatic driver shield and Uno microcontroller:*

The analog voltage, which controls the pressure regulator to adjust the air pressure, is provided by Uno microcontroller (Arduino) via pulse width modulation (PWM). PWM is a technique for acquiring analog results with digital means. The pressure regulator requires voltage between 0V to 10 V, however, Uno microcontroller can only provide maximum voltage 5V. It means the output voltage of the Uno microcontroller needs to be amplified by a factor of 2.

The pneumatic driver shield (Lenssen, J.A., 2019) is for amplifying the voltage from Uno microcontroller. It is shown in Figure 4.4 that the pneumatic driver shield is a printed circuit board (PCB). It has the same shape as the Uno microcontroller and is placed directly on the Uno microcontroller. This structure helps to reduce the number of cables and makes the setup more robust. The layout of the pneumatic driver shield is described in Figure 4.5. The area (B) on the pneumatic driver shield contains four connectors, each of which can be connected to one pressure regulator.

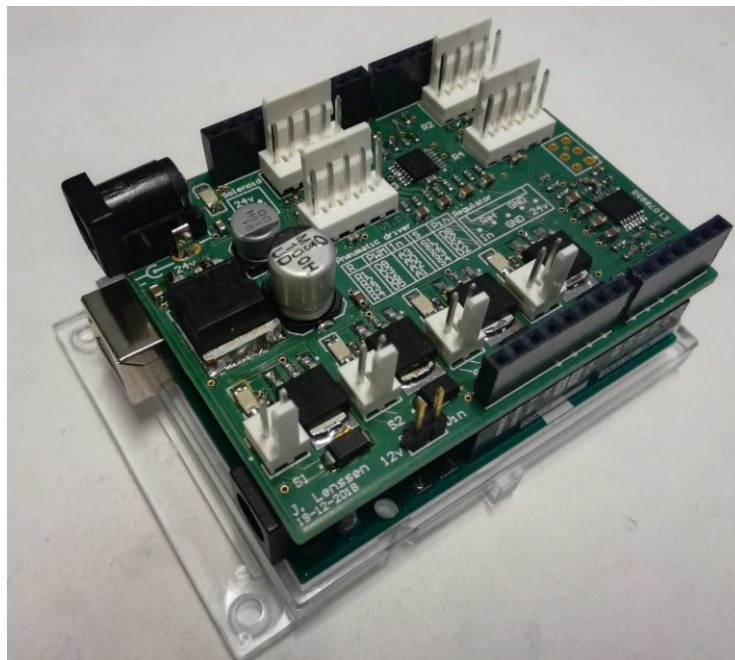


Figure 4.4 The combination of the pneumatic driver shield and the Arduino Uno microcontroller [6]. Pneumatic driver shield is located on top layer while Uno microcontroller is placed on the bottom layer.

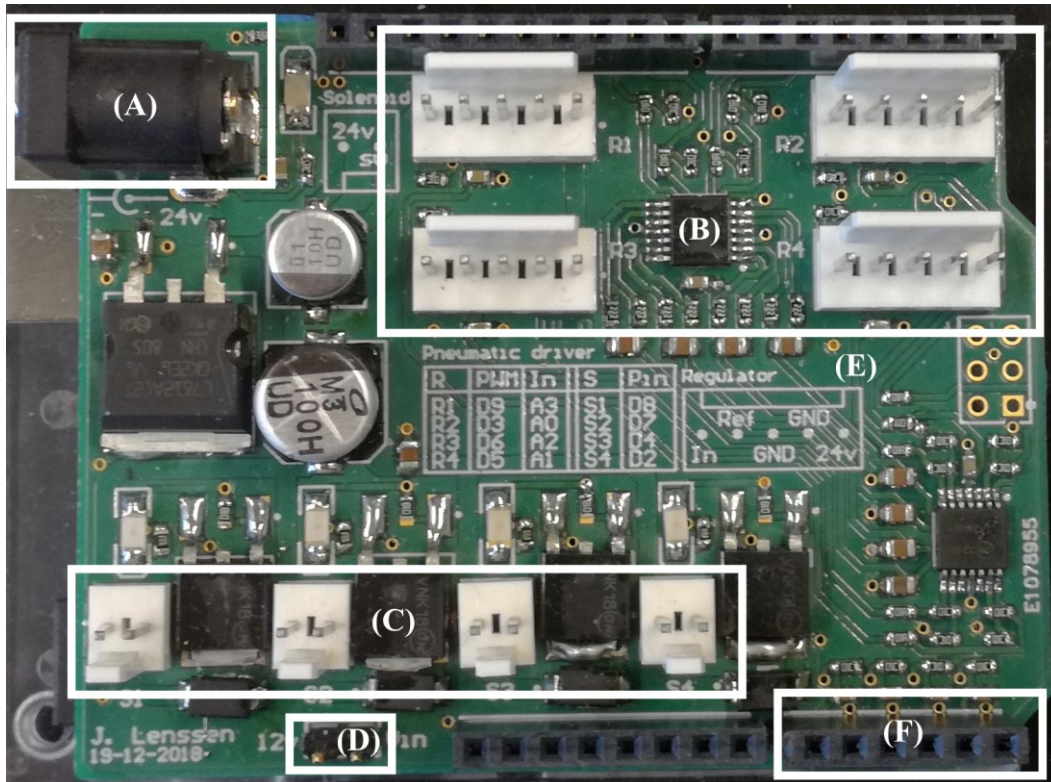


Figure 4.5 The layout of pneumatic driver shield [6]. (A) DC input for 24V power supply. (B) four connectors for connecting maximal four pressure regulator. (C) connectors for connecting maximal four solenoid valves which will not be used in this project. (D) jumper determining whether the Arduino Uno is powered by a separate source. (E) pin numbering information for connecting hardware. (F) the auxiliary analog inputs  $A_i$

#### 4.2.2. Experiment methodology

The purpose of this experiment is to obtain the mathematical relationship between the bending angle and input air pressure. As shown in Figure 4.6, the system characterization experiment is implemented by making the air pressure signal synchronize the tracking of the new design's bending angle.

The data transmitted from the coil sensor contains the position and orientation of the tip of the new design. The frequency of recording data is 40 Hz for the coil sensor. The bending angle of the new design can be calculated based on the orientation of the new design's tip. The time-varying bending angle of the new design is presented in Figure 4.7 (a).

Figure 4.7 (b) shows the time-varying staircase pressure signal. The period of time for each staircase is 2s. Each staircase corresponds to a specific value of the input air pressure. During this 2s period of time, 80 samples of the bending angle can be obtained in Figure 4.7 (a). The average of these 80 values of the bending angle corresponds to the air pressure for this staircase. By this method, the relationship between the bending angle and the input air pressure can be achieved and shown in Figure 4.8.

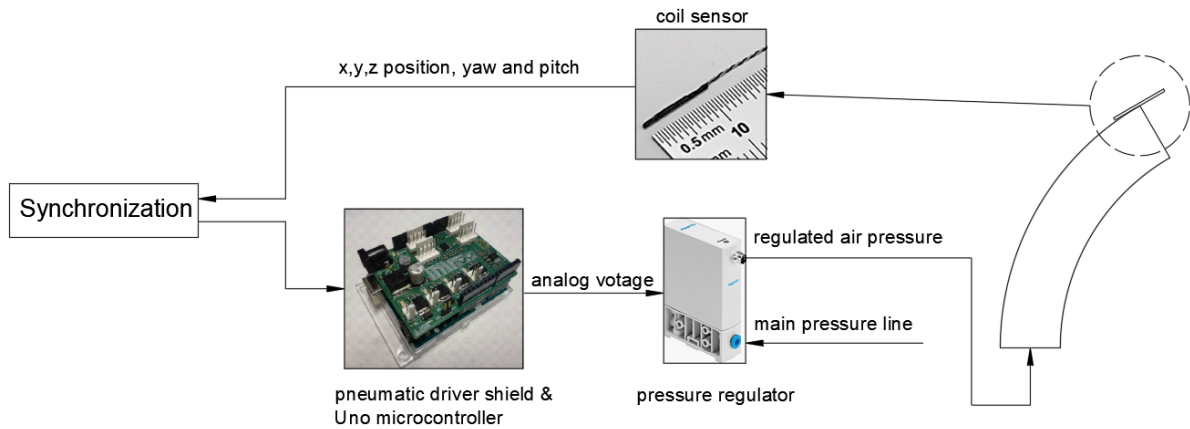


Figure 4.6 Schematic diagram of system characterization experiment. The tracking of the tip of new design by coil sensor is synchronized with varying input pressure to new design

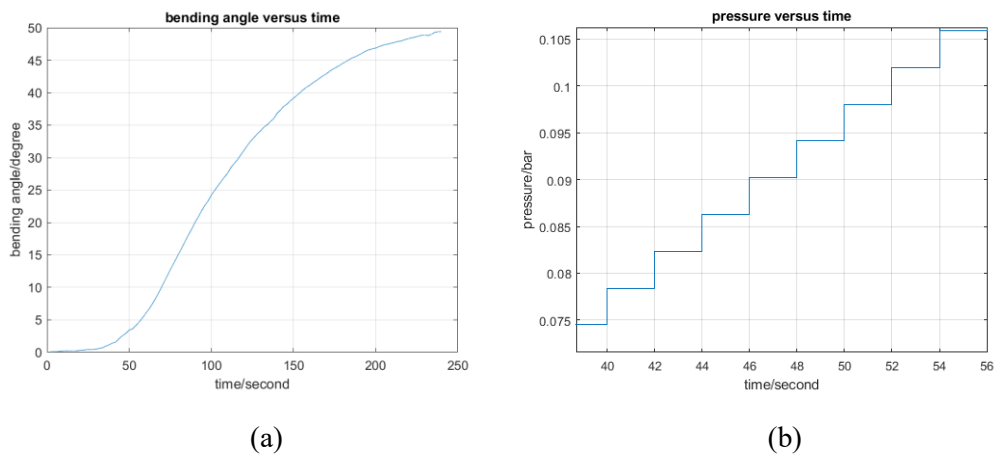


Figure 4.7 (a) bending angle of the new design tracked by coil sensor on time (b) pressure values of the new design adjusted by pressure regulator on time

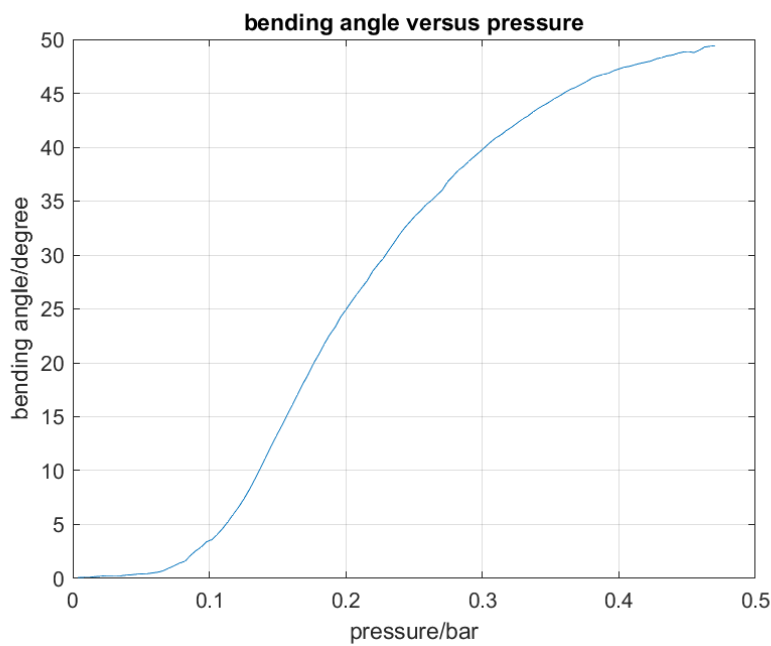


Figure 4.8 Synchronized plot presenting the relationship between bending angle of new design and the input air pressure

### 4.2.3. Test protocols

In this project, the one-chamber bending is defined as the bending performance of the new design when only one single chamber is actuated, while the two-chamber bending is defined as the bending performance of the new design when only two of three chambers are actuated with same air pressure simultaneously.

The one-chamber bending and two-chamber bending are measured by system characterization experiments. The one-chamber bending experiment will be conducted by only actuating single chamber and recording the corresponding bending angle. Two-chamber bending experiment will be executed by actuating two chambers with same air pressure at the same time and recording the corresponding bending angle. For one module of the new design, one-chamber bending experiment will be executed on three single chambers. For each chamber, this experiment will be repeated 5 times for testing the repeatability of the one-chamber bending performance. Similarly, one module of the new design involves three kinds of two-chamber combinations. Two-chamber bending experiment will be executed on three combinations of two chambers. For each combination, system characterization experiment will be repeated 5 times.

The objective of image processing on bent configuration is to examine the correctness of constant curvature assumption. The backbone curvature of the new design will be compared with the estimated backbone curvature of constant radius. If the backbone curvature coincides with the estimated backbone curvature, it means that the constant curvature assumption is correct, otherwise the constant curvature assumption is not applicable to the new design.

The elongation experiment is designed for measuring the elongation capability of the new design. This experiment is similar to one-chamber bending and two-chamber bending, but only the amount of elongation corresponding to the air pressure will be recorded.

Hysteresis experiments aim to examine the hysteresis behavior on one-chamber bending performance. The pressure will be increased and then decreased in the form of stairstep and, at the same time, the corresponding bending angle will be recorded.

## 4.3 System characterization results

In this section, the results of system characterization experiments will be presented in aspects of one-chamber bending and two-chamber bending. The correctness of constant curvature assumption will be examined. In addition, the elongation capability and hysteresis behavior of the new design will be measured and discussed. The analytical model and system characterization will be compared with each other.

### 4.3.1. One chamber bending

Due to the fact that one module contains three chambers, the module is able to bend in three different orientations. The relationship between the bending angle of the new design and the input air pressure to a single chamber is shown in Figure 4.9.

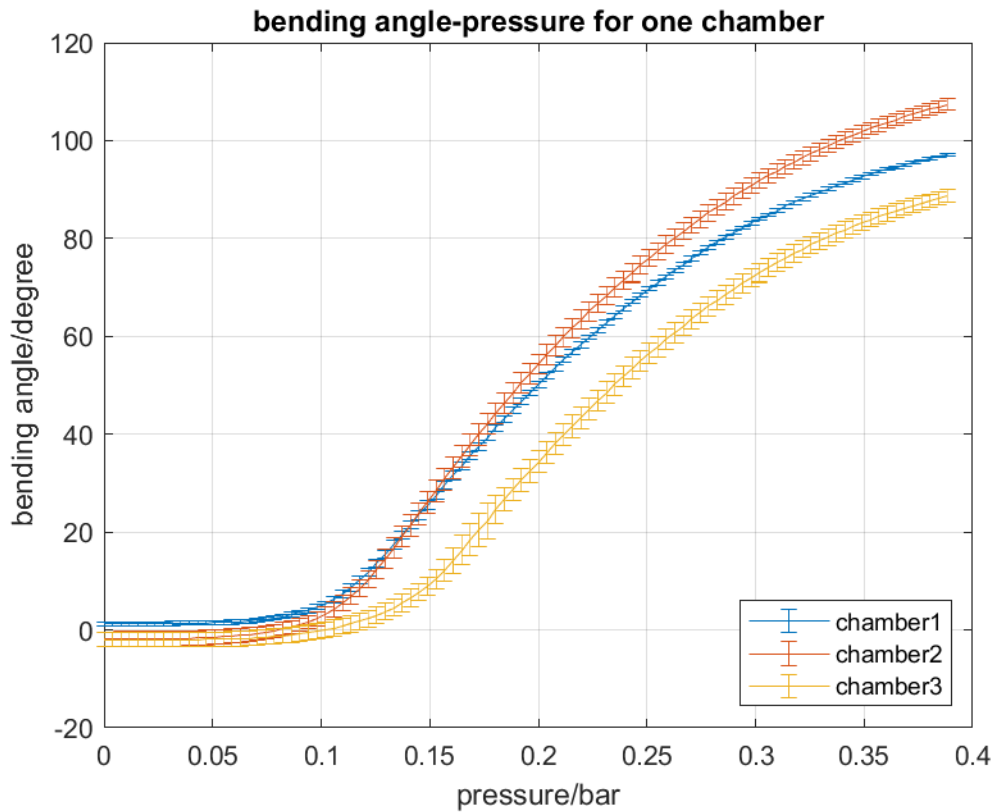


Figure 4.9 Bending angle versus pressure characteristic for three single chambers bending

It is observed in Figure 4.9 that three chambers result in different bending performance. This deviation might be caused by the fabrication processes. To analyze the one chamber bending, the gradient of bending angle to air pressure is plotted in Figure 4.10. Based on Figure 4.9 and Figure 4.10, the system characterization of one-chamber bending can be divided into three parts. The first part is from 0 bar to 0.05 bar. In this part, the gradient is almost 0. It means that the increase of air pressure will not lead to the change of bending angle. For this reason, this part is called 'zero-bending zone' in this article. The second part is from 0.05 bar to 0.15 bar. The gradient starts to increase from 0 until the maximum value (around 2.2 degree/ increment). From 0.05 bar to 0.1 bar, the bending angle increase in a low speed while when the pressure is from 0.1 bar to 0.15 bar, the bending angle increases in a high speed. The third part is when the pressure is more than 0.15 bar. In this part, the gradient starts to decrease in a constant speed (around  $10^\circ/(\text{increment} * \text{bar})$ ). The increase of pressure will also result in the increase of the bending angle. However, due to the decrease of the gradient, it is estimated that the pressure over a specific value (around 0.43 bar) will not result in the increase of the bending angle, and the bending angle of the module will eventually reach a maximum value (around  $100^\circ$ ).

One possible reason for zero-bending zone is the static friction between the elastomer and the external braided sheath. Because the inner diameter of the external braided sheath is 0.5 mm larger than the diameter of elastomer, when the chamber is unactuated, there is free space between the elastomer and the external braided sheath. It is not considered for this free space to cause zero-bending zone because the inflation of the chamber is observed very sensitive to air pressure when there is no limitation. This free space will be filled in rapidly by the inflation of the chamber with air pressure less than 0.05 bar. The inflation of the chamber will also lead to the elastomer touching the internal surface of the braided sheath. Due to the constraint of the external braided sheath, the chamber can only expand along its longitudinal direction which means there is a trend of movement between the elastomer and the braided

sheath. This trend of movement leads to static friction which will prohibit the expansion of chamber until it overcomes this static friction.

In second part, the low gradient, when pressure is from 0.05 bar to 0.1 bar, might be due to the free expansion of inflated chamber towards adjacent chambers. Although the radial expansion of the chamber is restricted, the inflated chamber would expand along the direction to adjacent unactuated chambers. This behavior may lead to the low gradient. The high gradient, when the pressure is from 0.1 bar to 0.15 bar, may be due to that the expansion of the inflated chamber is mainly along longitudinal direction.

In third part, one possible reason for the decreasing gradient is the saturation of bending ability of the external braided sheath. The bending of the module would increase the fiber angle of the external braided sheath. The increase in fiber angle would lead to the decrease in the bending performance of the external braided sheath. In addition, the energy for deformation would be consumed partly because of the friction between the external braided sheath and the elastomer.

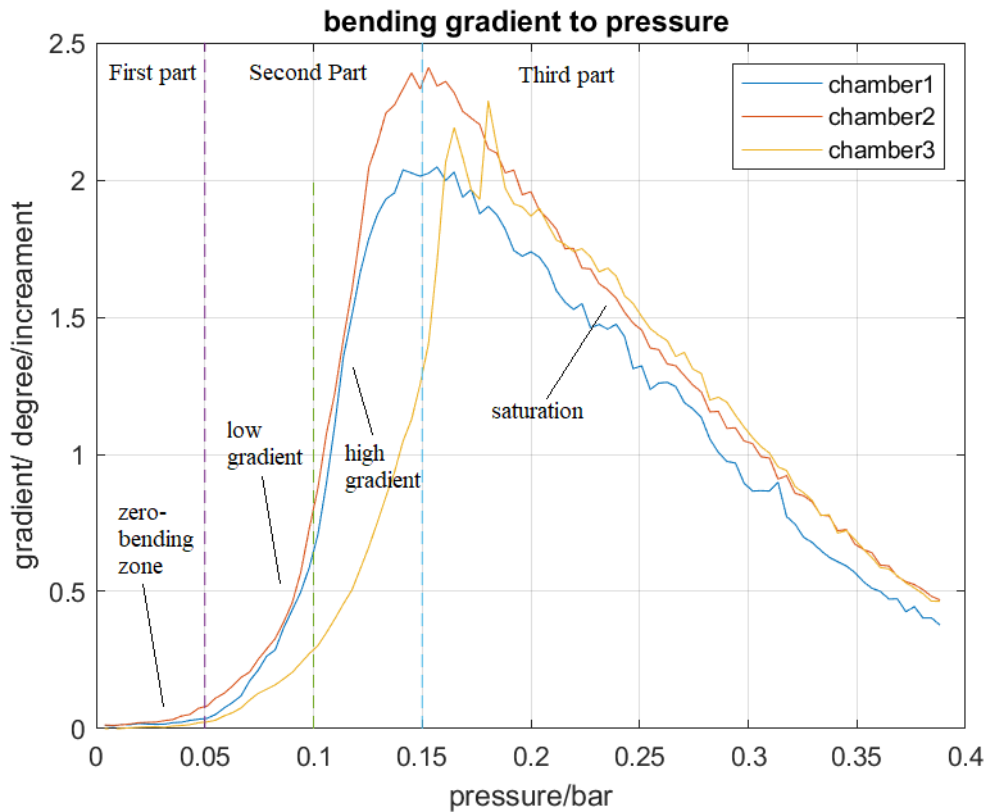


Figure 4.10 The increase rate of bending angle in terms of air pressure. The increase equals 0.0039 bar in this project

### 4.3.2. Two-chamber bending

The system characterization of two-chamber bending is illustrated in Figure 4.11. There are three combinations of two chambers. They are described as chamber 1&2, chamber 1&3 and chamber 2&3 in this article.

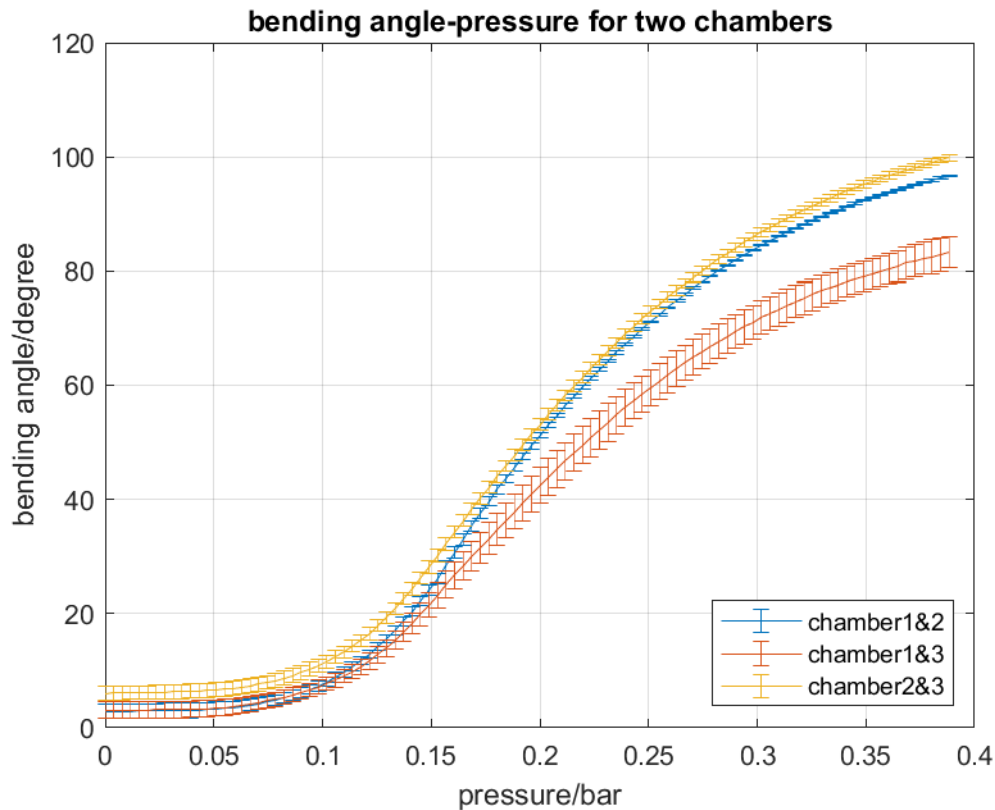


Figure 4.11 Bending angle versus pressure for two chambers bending

For analyzing the bending performance of two-chamber actuation, the gradient of the bending angle to air pressure is plotted in Figure 4.12. Similar to one-chamber bending, the bending performance of two-chamber actuation can also be divided into three parts. The first part is the zero-bending zone. This part is from 0 bar to 0.05 bar. In this part, the increase in air pressure will not lead to the change of the bending angle. The second part is from 0.05 bar to 0.15 bar. The gradient of the bending angle starts to increase and finally reaches a maximum value (around  $2^\circ/\text{increment}$ ). The third part is when the gradient starts to decrease and reaches 0 again.

The possible reasons for three parts in two-chamber bending are similar to one-chamber bending. In the low-gradient part of two-chamber bending, it is expected that the free expansion of inflated chambers toward the adjacent unactuated chamber, is less than that in one-chamber bending. However, statics show that for both one-chamber bending and two-chamber bending, the gradient  $0.5^\circ/\text{increment}$  corresponds to 0.09 bar. The free expansion of inflated chambers toward adjacent unactuated chamber in two-chamber bending is not relieved compared to one-chamber bending.

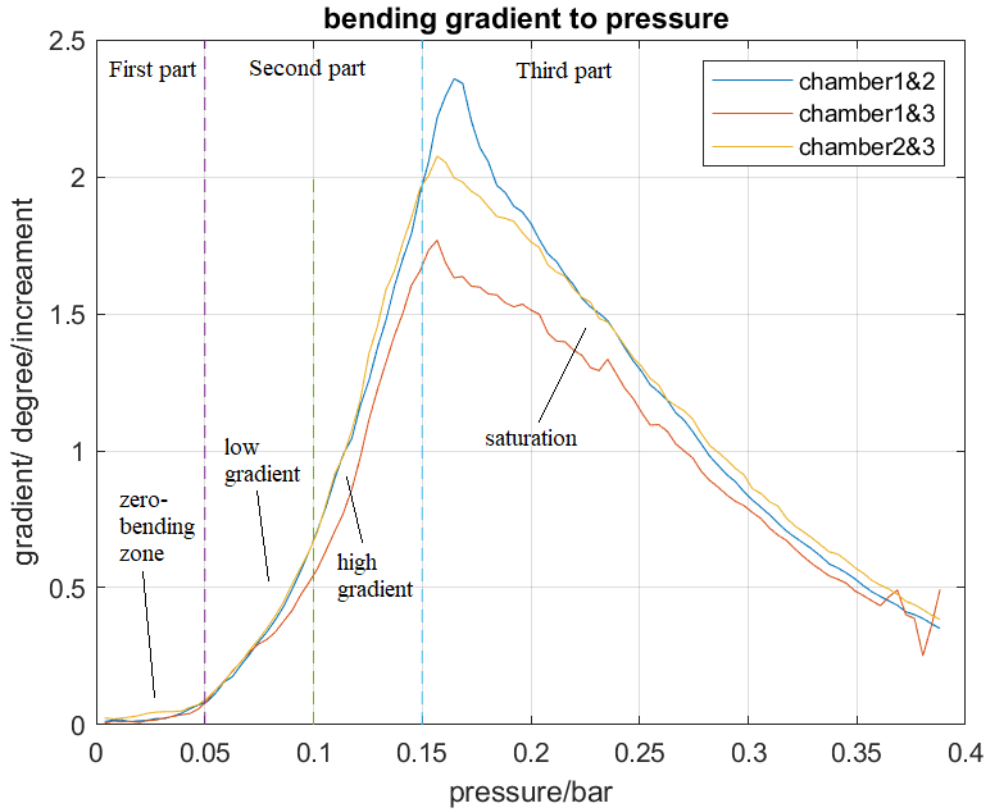


Figure 4.12 Gradient of two-chamber bending respect to air pressure

In chapter 3, it has been discussed that change of the internal layout caused by inflated chambers will result in the bending performance of two-chamber bending less than that of one-chamber bending. To examine the ability of the new design to maintain the internal layout, the system characterization of two-chamber bending will be compared to that of one-chamber bending. The comparison results are shown in Figure 4.13.

If the internal layout of the module does not change with the increase of air pressure, the system characterization of two-chamber bending should be the same as one-chamber bending. It is observed in Figure 4.13 (a) that the bending performance of chamber 1 is almost the same as the bending performance of the combination of chamber 2 and chamber 3. However, the sum of bending moments caused by two chambers actuation, will be influenced by the deviation of one-chamber bending. For example, in Figure 4.13 (b) and (c), there is a large difference between one-chamber bending and two-chamber bending. To remove the influence caused by different one-chamber system characterization, chamber 1 and chamber 2 are selected, since their one-chamber system characterization has little difference. The combination of chamber 1 and chamber 2 is selected to make comparisons with their one-chamber bending performance. It is shown in Figure 4.14 that there is little difference between the bending performance of two-chamber bending and one-chamber bending. It may prove that the internal layout of the new design does not change greatly.

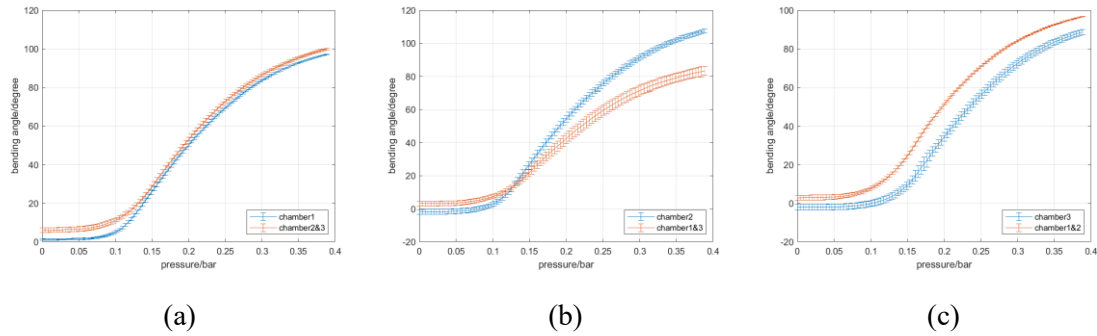


Figure 4.13 Comparison of system characterization between one chamber bending and two-chamber bending. (a) Comparison of system characterization between chamber 1 and chamber 2&3 (b) Comparison of system characterization between chamber 2 and chamber 1&3 (c) Comparison between system characterization between chamber 3 and chamber 1&2.

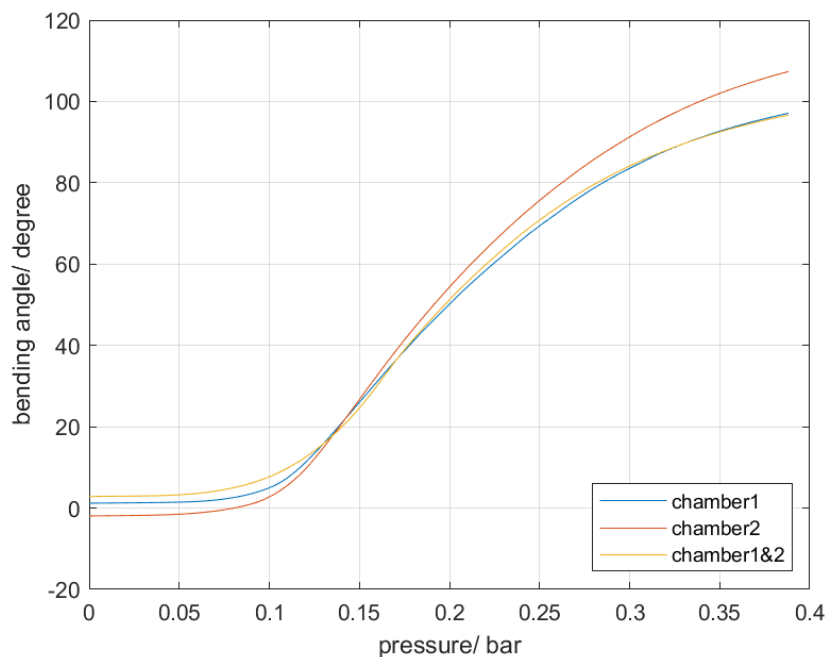


Figure 4.14 Bending angle versus pressure characteristic for chamber 1, chamber 2 and the combination of chamber 1 and chamber 2

### 4.3.3. Examining assumption of constant curvature model

In this section, the correctness of constant curvature assumption will be examined. The method to examine the constant curvature assumption is comparing the backbone curvature of the module with the estimated backbone curvature of constant radius. The length of the backbone and the bending angle of the new design are calculated by image processing program (ImageJ). Based on these two parameters, the estimated backbone curvature is calculated and drawn on the bent configuration of the new design.

The bent configuration is captured by camera view. An example shown in Figure 4.15 represents the bent configuration of one-chamber bending of the new design with input air pressure 0.2 bar. The plane containing the bent configuration is parallel to the camera view. A scale is located on the plane containing the bent configuration to provide a reference for the translation between number of pixels and actual length in unit mm.

The length of inner curvature  $l_1$  and the length of outer curvature  $l_2$  are derived from bent configurations. The length of backbone curvature  $l$  is the mean of  $l_1$  and  $l_2$ . That is:

$$l = \frac{l_1 + l_2}{2}$$

The radius  $\rho$  of the estimated backbone curvature is calculated as follows:

$$\rho = \frac{l}{\alpha}$$

$\alpha$  is the bending angle of the new design in the form of radian. The length of backbone and the corresponding bending angle of the new design under different pressures are shown in Table 4.1.

The backbone curvature of the module and the estimated backbone curvature of constant radius are presented in Figure 4.15. The estimated backbone curvature of constant radius is presented in the green line, while the backbone of physical module is presented by the purple line.

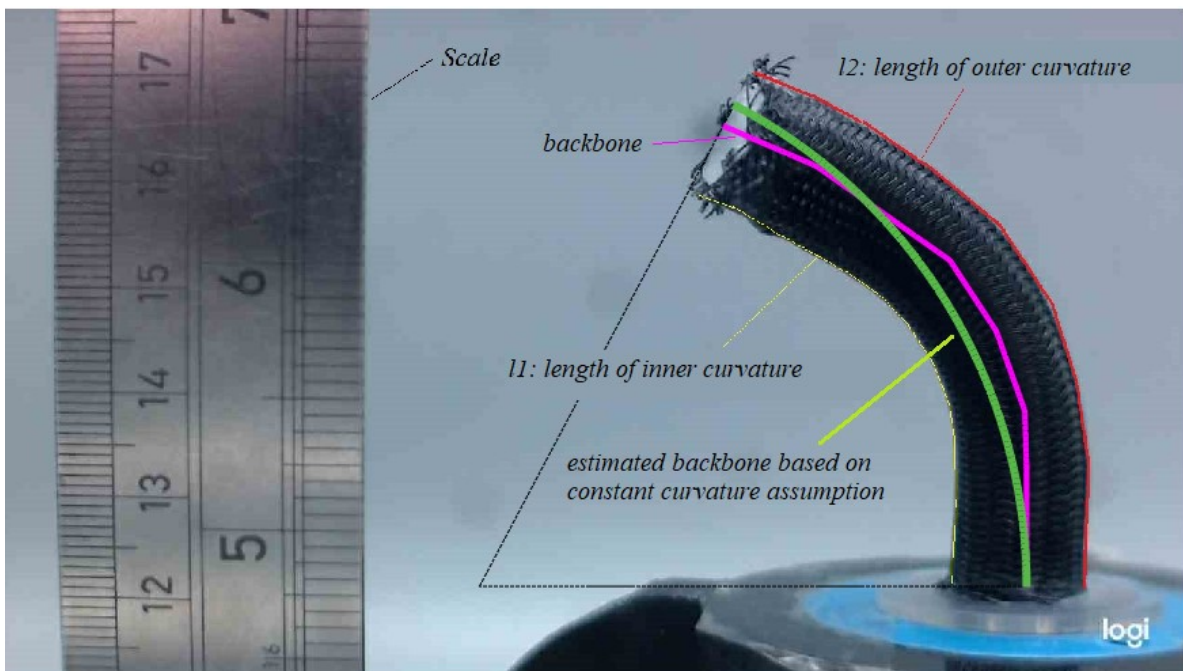


Figure 4.15 Bent configuration of module captured by camera view

Figure 4.15 shows that there is deviation between the backbone curvature of the new design and the estimated backbone curvature of constant radius. The physical module does not have constant radius along its central axis. It could be concluded that the constant curvature model is not applicable to the new design

#### *Elongating of the bending module:*

It is derived from Figure 4.16 that the elongating of inner curvature  $\Delta l_1$  at 0.4 bar is around 1.97 mm which is 4% compared to the original length of the module, while the elongating of the backbone curvature  $\Delta l$  and outer curvature  $\Delta l_2$  are 12.8 mm and 23.2 mm which are 25% and 44.7 % with respect to the original length of the module at 0.4 bar separately.

Table 4-1 Length of the module backbone under different pressures

chamber	pressure/ bar	$l_1/mm$	$l_2/mm$	backbone/ mm	bending angle /degree
1	0	51.3	52.5	51.9	0
1	0.1	50.7	52.6	51.6	6.2
1	0.2	50.7	62.7	56.7	42.2
1	0.3	53.2	73.6	63.4	78
1	0.4	53.1	76.2	64.6	93
2	0	48.9	51.1	49.4	3.8
2	0.1	51.5	54.6	53	12.2
2	0.2	50.3	66	58.1	62.3
2	0.3	48.6	71.4	59.9	96.3
2	0.4	50.5	76.1	63.3	119
3	0	51.9	52.1	52	1.5
3	0.1	52.5	51.7	52.1	0.5
3	0.2	52	59.4	55.7	30
3	0.3	51.5	68.8	60.1	69.6
3	0.4	54.4	73.1	63.8	79.6

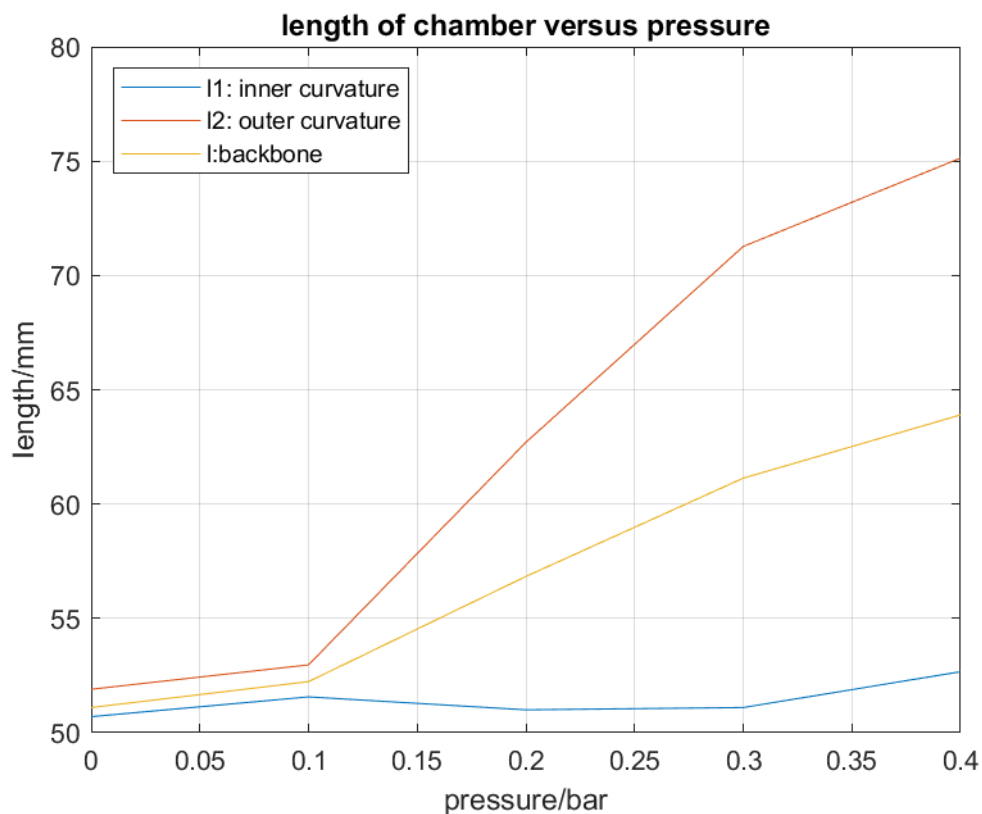


Figure 4.16 Length of inner curvature, outer curvature and backbone curvature under different pressures

#### 4.3.4. Elongation of the module with three actuated chambers

When all three chambers are activated with the same amount of pressure simultaneously, the module would only elongate. In practical, three chambers have three different system characterization. It means that when three chambers are activated with the same air pressure at the same time, the resulting elongation of the module is not along Z-axis. For this reason, the elongation is calculated by the square root of summation of increment of the tip position along x, y and z axis ( $\Delta l = \sqrt{\Delta x^2 + \Delta y^2 + \Delta z^2}$ ). Figure 4.17 shows the relationship between the elongation of the module and input pressure. The elongation of the module at 0.4 bar is 5.3 mm which is 10.6% with respect to the initial length of the module.

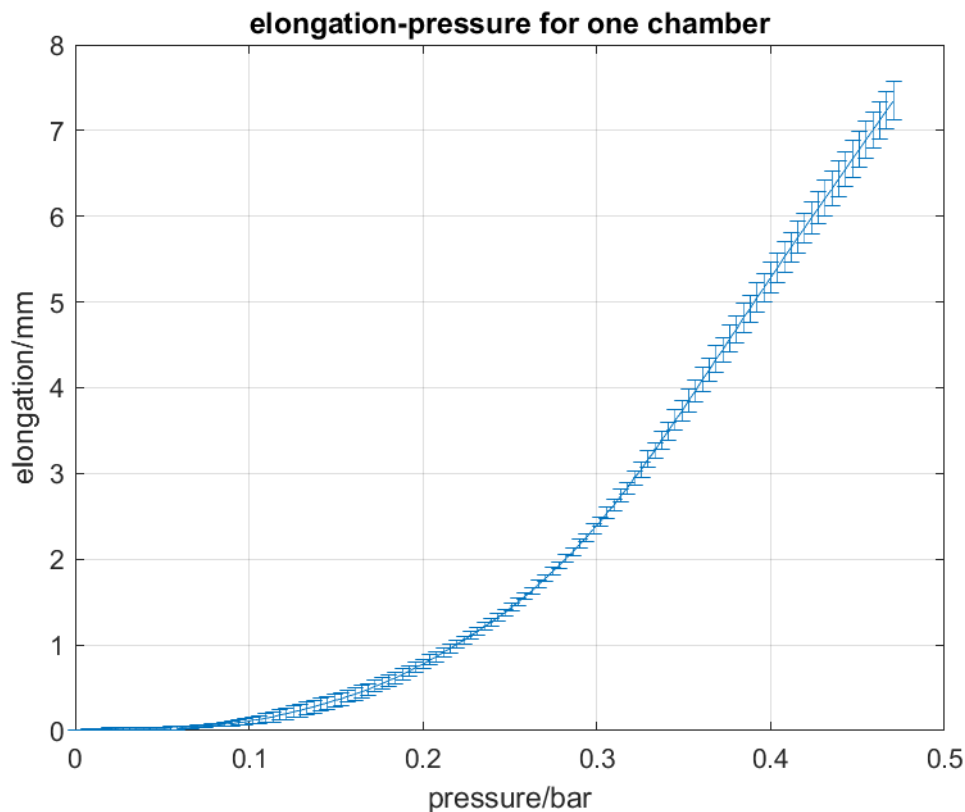


Figure 4.17 Elongation versus pressure graph for actuating all three chambers simultaneously

#### 4.3.5. Bending Hysteresis

The pressure in system characterization experiments varies in ascending order. In the hysteresis experiment, after the pressure increases to the maximum value, the recording of the bending angle continues, meanwhile the pressure value decreases in descending order until it reaches 0 bar. The resulting of the hysteresis experiment is shown in Figure 4.18. This experiment was executed on another module.

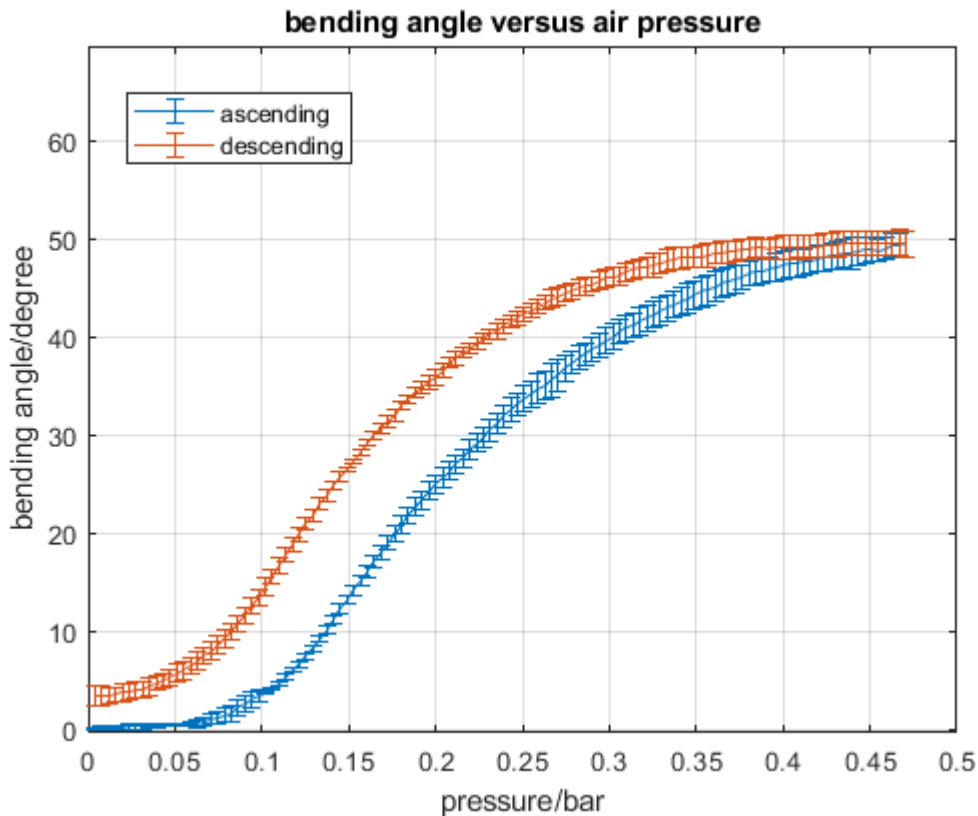


Figure 4.18 Hysteresis of bending angle with pressure varying in ascending and descending order

It is shown in Figure 4.18 that the maximum difference of bending angle between two curves is  $13.7^\circ$ . In previous studies, the bending performances of STIFF-FLOP design with internal braiding and external braiding have similar hysteresis [19].

One possible reason for the bending hysteresis is the strain hysteresis behavior of the elastomer under uniaxial deformation. The hysteresis behavior of elastomer, Eco-Flex 0030, under different load directions has been studied by D.Ahmad [20]. It is shown in Figure 4.19 that the uniaxial hysteresis becomes obvious when the strain of elastomer is over 0.75. However, the module of the new design is fabricated by Eco-Flex 0050 which hysteresis may be different from Eco-Flex 0030. The hysteresis of Eco-Flex 0050 is studied by Y.Hsu [21]. It is concluded that when the strain is less than 0.2, there is no hysteresis for Eco-Flex 0050. The strain of the inflated chamber in this project is from 0.25 to 0.45 by the measurement in chapter 4.3.3, which is more than 0.2. For this reason, the hysteresis of Eco-Flex 0050 should be studied in the future project.

In addition, the bending hysteresis may result from the stress relaxation [22] caused by the friction between the internal surface of the braided sheath and the external surface of the elastomer.

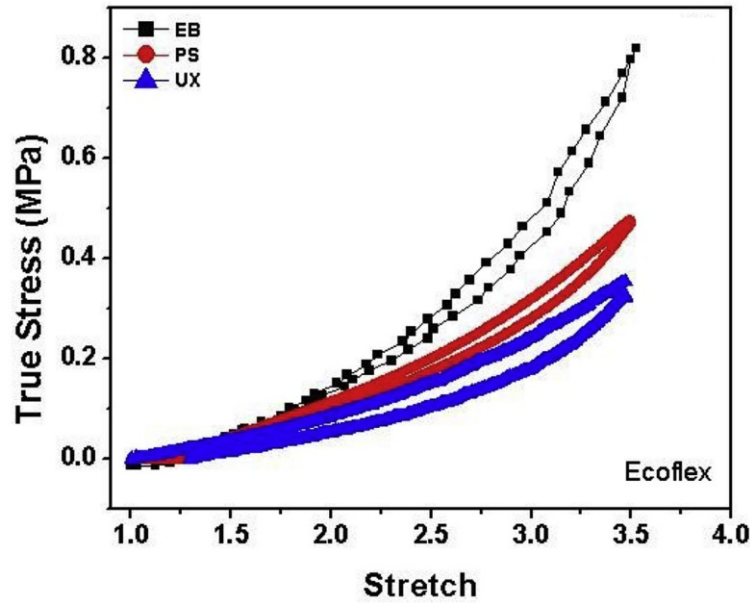


Figure 4.19 Hysteresis of Eco-Flex 0030 under UX (uniaxial), PS (pure shear), EB (equibiaxial) loading [20]

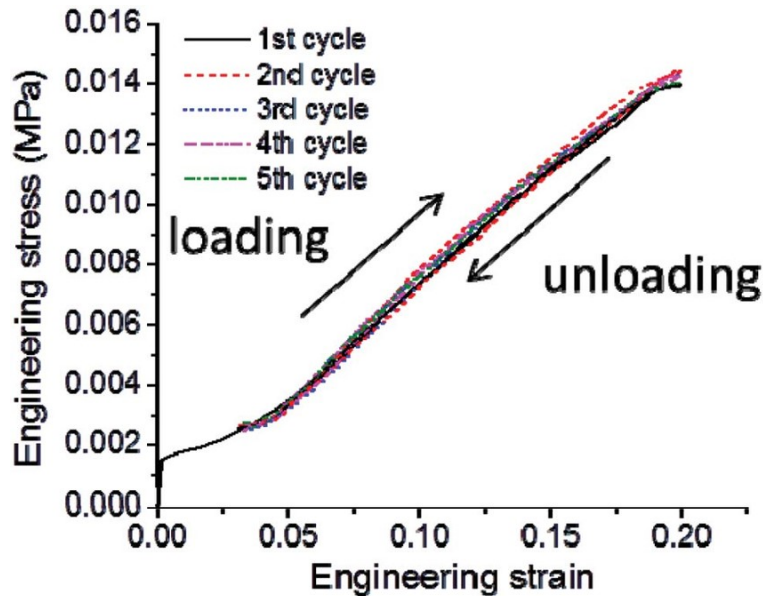


Figure 4.20 Hysteresis of Eco-Flex 0050 when strain is less than 0.2 [21]

#### 4.3.6. Comparison between analytical model and system characterization

The system characterization in Figure 4.21 represents the practical one-chamber bending behavior of the new design. The analytical model based on Equation (8) is plotted in the dash line.

In Equation (8), one assumption is that all parameters in the right part of equation except pressure are constant. For this reason, the bending angle in analytical model can be regarded as the addition of a quadratic part and a linear part of pressure. The quadratic part of the analytical model is inversely proportional to the square of Young's modulus. Referring to values of parameters shown in Table 3.3, the Young's modulus of elastomer is around  $\frac{1}{150}$  to  $\frac{1}{21462}$  compared to other parameters with equalized unit. For this reason, the linear part dominates the analytical model when the input air pressure is in

little value. This property is shown in Figure 4.22 that when the pressure is less than 0.3 bar, the curve of analytical model shows only linearity and when the pressure is more than 0.3 bar, the non-linearity is observed.

Even though research of Hsu [21] demonstrates that the Young’s modulus of Eco-Flex 0050 is constant when the strain is less than 0.2, research (Ranzani, T et al., 2015 and Kim, S et al., 2016) [23] [22] reveals that the Young’s modulus of Eco-Flex 0050 is not constant when the strain is more than 0.2. It is estimated that the elastic modulus for the strain less than 0.4 is around 0.11 MPa. For the strain between 0.4 and 1.0, the elastic modulus is around 0.37 MPa. In order to show the sensitivity of the analytical model to the elastic modulus, Figure 4.21 presents the performance of the analytical model with different possible values of elastic modulus within the range of strain it may occur. The analytical module behavior could be better represented by a more detailed model with local mechanical behavior (e.g. FE model). Although the analytical model does not follow the system characterization, in comparative study for different designs, shown in Figure 3.10, it indicates the influence of different chamber cross-section area on the bending performance of the module.

Compared to the analytical model, the system characterization shows great nonlinearity. As discussed in section 4.3.1, the system characterization can be divided into three parts with respect to the gradient of the bending angle to air pressure. The part of system characterization when air pressure is from 0 bar to 0.1 bar may result from the static friction between the external braided sheath and the elastomer. This static friction prohibits the axial elongating of the inflated chamber. The decrease of gradient, when air pressure is more than 0.2 bar, may be caused by the change of the fiber angle of the external braided sheath. When the module bends, the fiber angle of the external braided sheath increases, which is caused by the bending and elongating of the braided sheath. The increase of the fiber angle will reduce the bending performance of the external braided sheath. This may be the reason for the reduction of gradient.

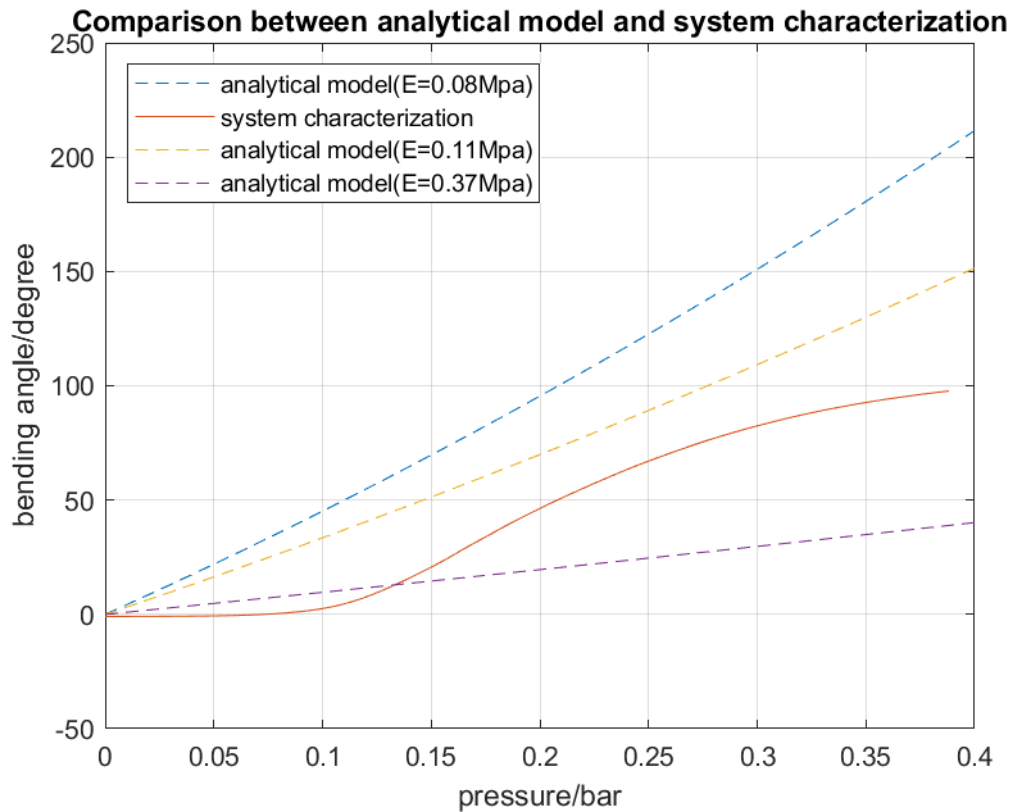


Figure 4.21 Comparison between analytical model and system characterization

It can also be observed that there is large difference between analytical model ( $E = 0.08$  Mpa) and system characterization. Combined with the result from chapter 4.3.3, the constant curvature model is not suitable for estimating the bending behavior of the new design. The more accurate model needs to be completed in the future project. One aspect that may be concerned is that the module of the new design is not fabricated by a single kind of silicone material. The top part and the bottom part of physical module are fabricated by Dragon Skin 10, a more rigid material than Eco-Flex 0050. The chamber part of the module could be considered as constant curvature model, while the bottom part and the top part could be regarded as rigid beams. The entire new design would be regarded as the constant curvature model connecting two rigid beams.

It is assumed that the bending performance of the module is influenced by the friction between the external braided sheath and the elastomer. In addition, the bending of the external braided sheath would increase its fiber angle which limits the bending performance of the module. However, these two factors are not included in the current constant curvature model.

#### 4.4 Conclusion of experimental characterization

In this chapter, experiments were designed and conducted for obtaining the system characterization of the new design. The module of the new design can obtain  $90^\circ$  one-plane bending angle under input pressure 0.38 bar. The maximum pressure is estimated as 0.43 bar by analyzing the gradient of the bending angle to air pressure. Contrast to STIFF-FLOP design, it is not observed the large deviation of system characterization between one-chamber bending and two-chamber bending. This could indicate that the new design is able to maintain the internal layout of chambers.

The backbone curvature of physical module does not coincide with the estimated backbone curvature of constant radius. It reveals that the constant curvature assumption is inapplicable for the new design.

For one-chamber bending, the backbone elongates 25% under pressure 0.4 bar. The elongation of the module is measured 10.6% with respect to the initial length when three chambers are actuated by 0.4 bar pressure.

The experimental characterization also measures the hysteresis on one-chamber bending. The elastomeric hysteresis property of material is considered as one possible reason. However, this hypothesis should be verified in the future research due to the lack of support literature and related documents.

The system characterization contains the zero-bending zone, gradient increasing part and gradient decreasing part, which is different from the analytical model. The zero-bending zone may result from the static friction between the external braided sheath and the elastomer. The gradient increasing part could be caused by the free expansion of inflated chamber towards the adjacent chambers or the longitudinal expansion. The gradient decreasing part may be due to the influence of the bending performance of the external braided sheath. The Young's modulus of the material has been proven inconstant with respect to strain. However, further research is required for understanding to what degree the change of Young's modulus affects the bending performance of the new design.

## 5. Control of bending angle of single module in one plane

In constant curvature assumption, the kinematic model (Webster, 2010) [24] provides mathematical transformations between characteristics in different spaces for tracking the tip of STIFF-FLOP design. This kinematic model is shown in Figure 5.1. The new design can be characterized by different parameters in different spaces. For example, in actuator space, the new design can be characterized by chamber length ( $l$ ) and chamber pressure ( $P$ ), while in configuration space, the new design can be characterized by the robot curvature  $\kappa$ , out-of-plane angle  $\beta$  and backbone length  $l$ . It is shown in Figure 5.2 that the tip position ( $x, y, z$ ) in the task space can be transformed into arc parameters ( $\kappa, \beta, l$ ) in configuration space. In constant curvature assumption, the one-plane bending angle  $\alpha$  is equivalent to the scalar product of  $l$  and  $\kappa$ . For this reason, in configuration space, the arc parameters ( $\kappa, \beta, l$ ) can be replaced by ( $\alpha, \beta$ ).

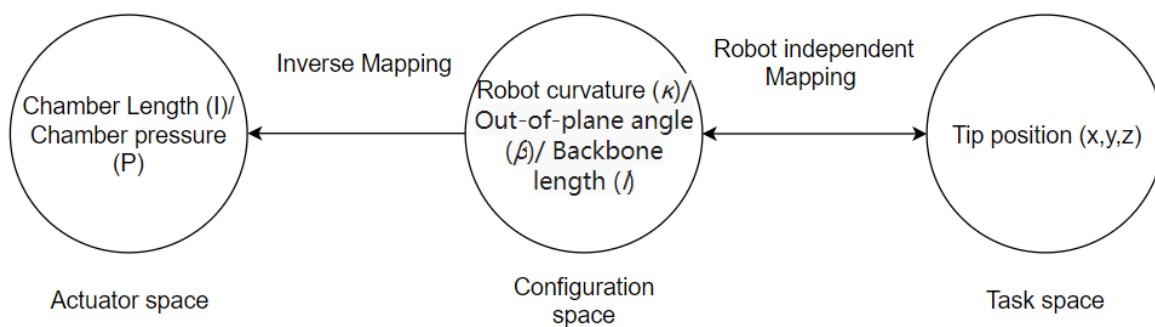


Figure 5.1 Kinematics model of constant curvature continuum robot (Webster,2010) [24]

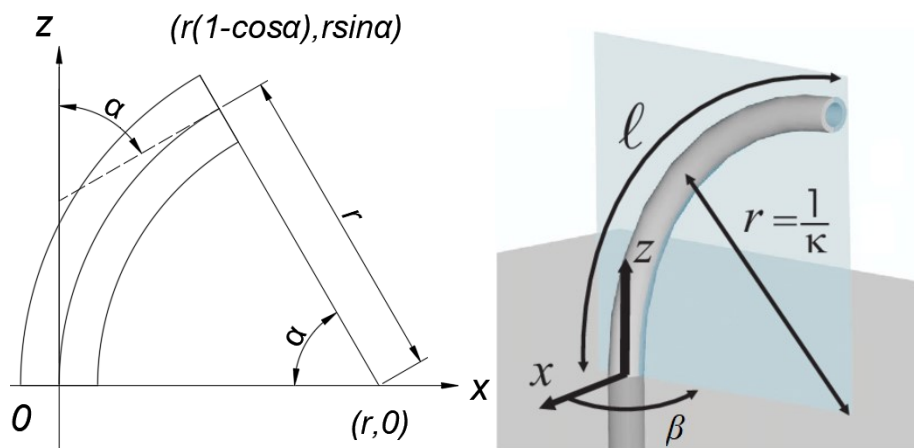


Figure 5.2 (left) constant curvature arc, the position of the tip in one-plane can be presented by the curvature radius  $r$  and the bending angle  $\alpha$ . (Right) arc parameters in constant curvature model,  $l$  is the length of the module,  $\kappa$  is the curvature of the module which equals reciprocal of  $r$ ,  $\beta$  is the out-of-plane rotation angle [24]

It is concluded in chapter 4 that the physical bending performance of the new design deviates from constant curvature model. However, in configuration space, the new design can still be characterized by ( $\alpha, \beta$ ). Therefore, it is still meaningful to control these two parameters. In this project, the control of out-of-plane angle is not considered. The controller will be designed to control only one-plane bending angle  $\alpha$ .

In previous studies, the physical bending performance of STIFF-FLOP design, in lab environment, is employed as feedforward controller. However, only feedforward controller is not functional when STIFF-FLOP design works in a different environment because disturbances, e.g. load on the tip of module, friction and module orientations, will have influence on the practical bending performance. Therefore, in this project, a PID feedback controller is developed for a more accurate control of one-plane bending angle.

The control performance of PID feedback controller is examined by validation experiments, for answering research questions on how to control the bending of the new design to compensate for limited load and module orientations. The preferable control performance is that the new design follows the desired trajectory of one-plane bending angle, when the new design is placed in different module orientations or limited load is attached on the tip of the new design. In this chapter, algorithms of PID feedback controller and feedforward controller will be introduced. The result of system characterization shown in chapter 4 is selected as the feedforward controller.

The module without load is defined, as only the coil sensor is attached on the tip of the new design shown in Figure 4.2. The weight and tension of the coil sensor is negligible compared to the weight of the module. That is why the module with only the coil sensor is defined as the module without load. The module with load is defined, as the disc sensor (Aurora 6DOF 61066) is added on the tip of the new design shown in Figure 5.3 (b). The weight of single module, containing elastomer and external braided sheath, is around 5g, while the disc sensor is around 20g. The cap is designed as the connection between Disc sensor and the module.

To examine the control performance of the controller to compensate for different module orientations, validation experiments will be performed on the module without load in vertical, horizontal and inverted module orientations. Three different module orientations of the module without load are shown in Figure 5.4. To examine the controller ability to compensate for limited load on the tip of the module, validation experiments will also be performed on the module with load. Figure 5.5 shows the module with load in three different module orientations.

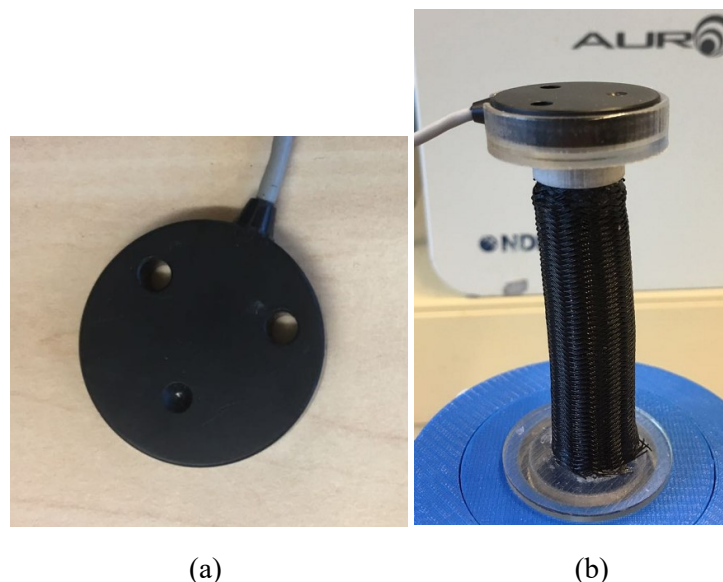
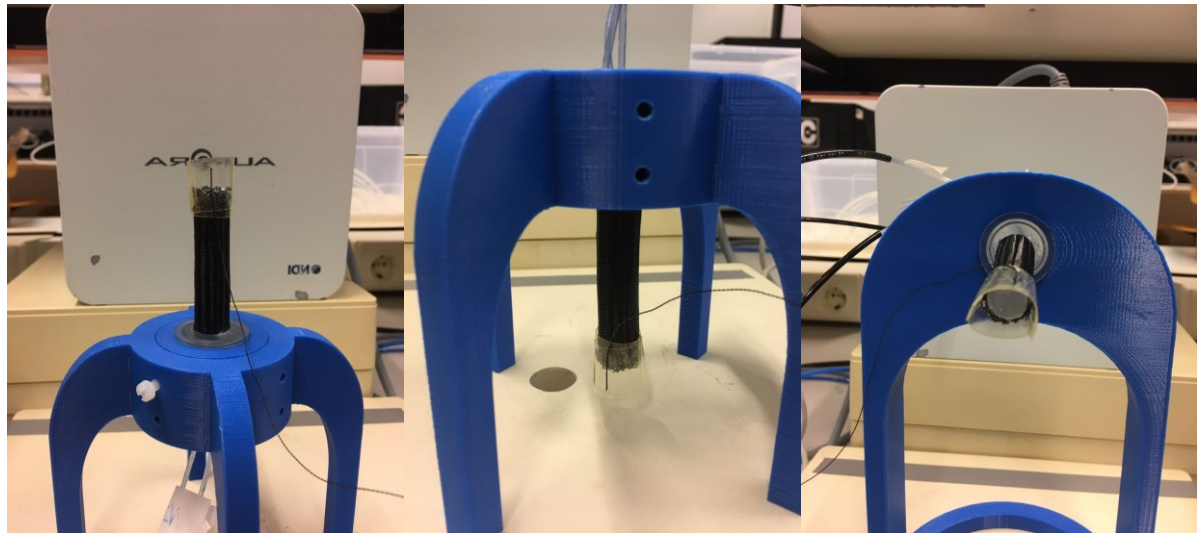
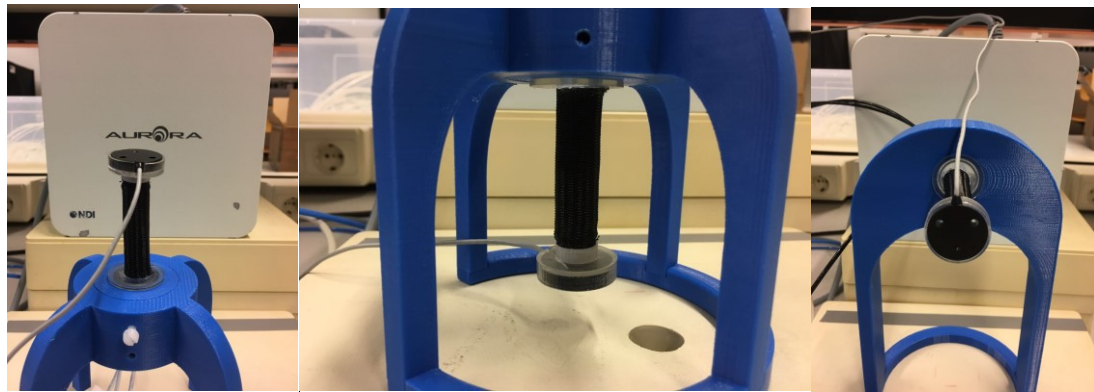


Figure 5.3 (a) Aurora 6DOF Disc sensor (b) the combination of Disc sensor on tip of the module in vertical orientation.



(a) (b) (c)

Figure 5.4 Module without load in different module orientations (a) Vertical module orientation. (b) Inverted module orientation. (c) Horizontal module orientation



(a) (b) (c)

Figure 5.5 Module with load in different module orientations. (a) Vertical module orientation. (b) Inverted module orientation. (c) Horizontal module orientation

### 5.1. Feedback and Feedforward algorithm for bending control

In Figure 5.6, on the plane comprising of x and z axis, when chamber 1 is pressurized, while chamber 2 and chamber 3 have 0 input pressure, the module bends to the positive direction. In this case, it is defined as positive bending, that the bending angle  $\alpha$  and corresponding air pressure are all positive values. In contrast, when chamber 2 and chamber 3 are activated by the same amount of pressure simultaneously, the resulting bending angle and corresponding air pressure are negative values. In this case, it is defined as negative bending, that both bending angle  $\alpha$  and corresponding air pressure are negative values.

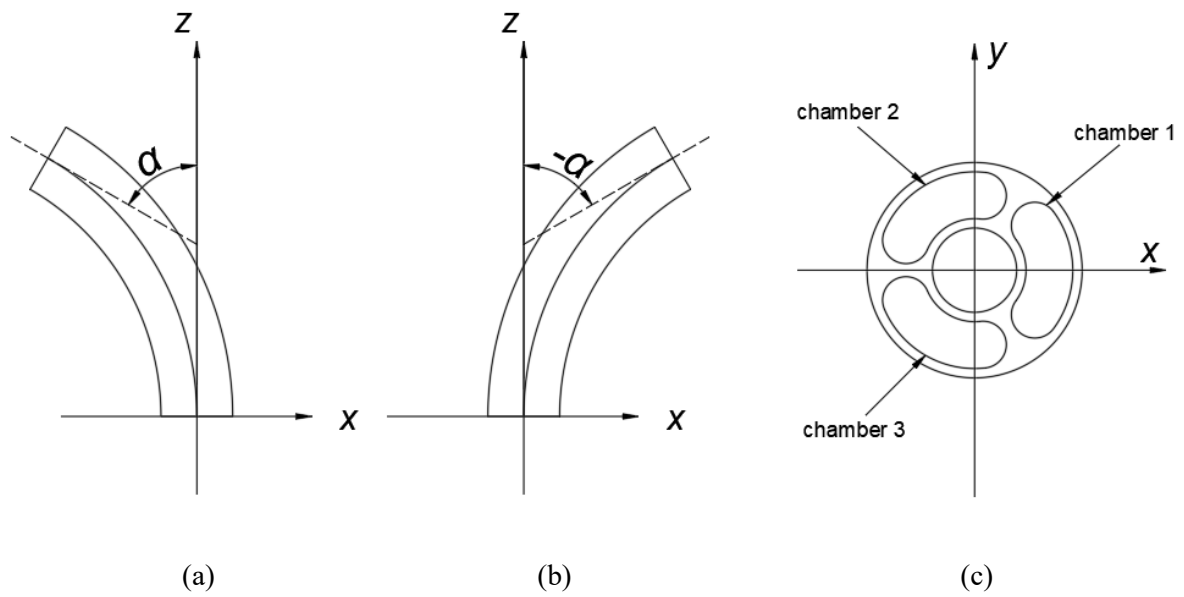


Figure 5.6 (a) Positive value of bending angle corresponds to positive value of pressure. (b) Negative value of bending angle corresponds to negative value of pressure. (c) The bottom view of module.

### 5.1.1. Combination of PID feedback controller and feedforward controller

It is shown in Figure 5.7 that the feedback control loop comprises PID controller, pressure regulator, module of the new design and sensor. The one-plane bending angle of module,  $\alpha_{cur}$ , is measured by sensor (coil sensor or disc sensor). Then  $\alpha_{cur}$  is given to PID controller to take a controlling action presented at Equation (9) and (10). The PID controller compares  $\alpha_{cur}$  with a desired one-plane bending angle  $\alpha_{ref}$ , and calculates the feedback control signal  $\mu_{fb}$  which will be given to pressure regulator. The bending of the module is directly affected by the varying pressure  $p$  from pressure regulator.  $\mu_{fb}$  will be 0 until  $\alpha_{cur}$  is equivalent to  $\alpha_{ref}$ .

In PID feedback control system, the controller takes action only after  $\alpha_{cur}$  deviates from  $\alpha_{ref}$ . To improve the response of the feedback control loop, the feedforward controller is implemented. Figure 5.7 shows that the feedforward control signal  $\mu_{ff}$  is only dependent on  $\alpha_{ref}$ . Feedforward control signal  $\mu_{ff}$  is then added directly to  $\mu_{fb}$  for adjusting the output of pressure regulator.

$$e(t) = \alpha_{ref}(t) - \alpha_{cur}(t) \tag{9}$$

$$\mu_{fb} = K_p e(t) + K_i \int e(t) dt + K_d \frac{de(t)}{dt} \tag{10}$$

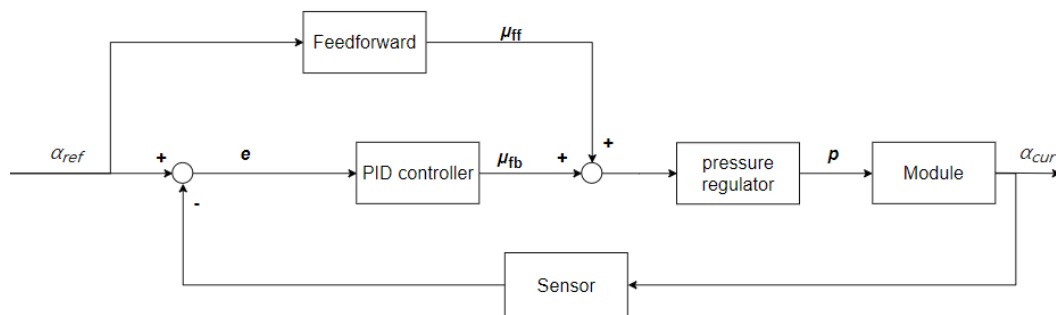


Figure 5.7 The block diagram of the entire closed loop system for controlling one-plane bending angle  $\alpha$

### 5.1.2. Implementation of feedforward controller

The feedforward controller is implemented by inverting the result of system characterization shown in Figure 5.8. The hysteresis behavior of the new design shown in Figure 4.18, is not addressed in the feedforward controller because it is estimated that the bending hysteresis can be compensated for by the feedback controller. The system characterization, shown in Figure 4.9 and Figure 4.11, is interpolated linearly so that it represents a non-linear mathematical relationship between one-plane bending angle and input air pressure. The value of air pressure corresponding to the desired one-plane bending angle, can be obtained from the inversed system characterization.

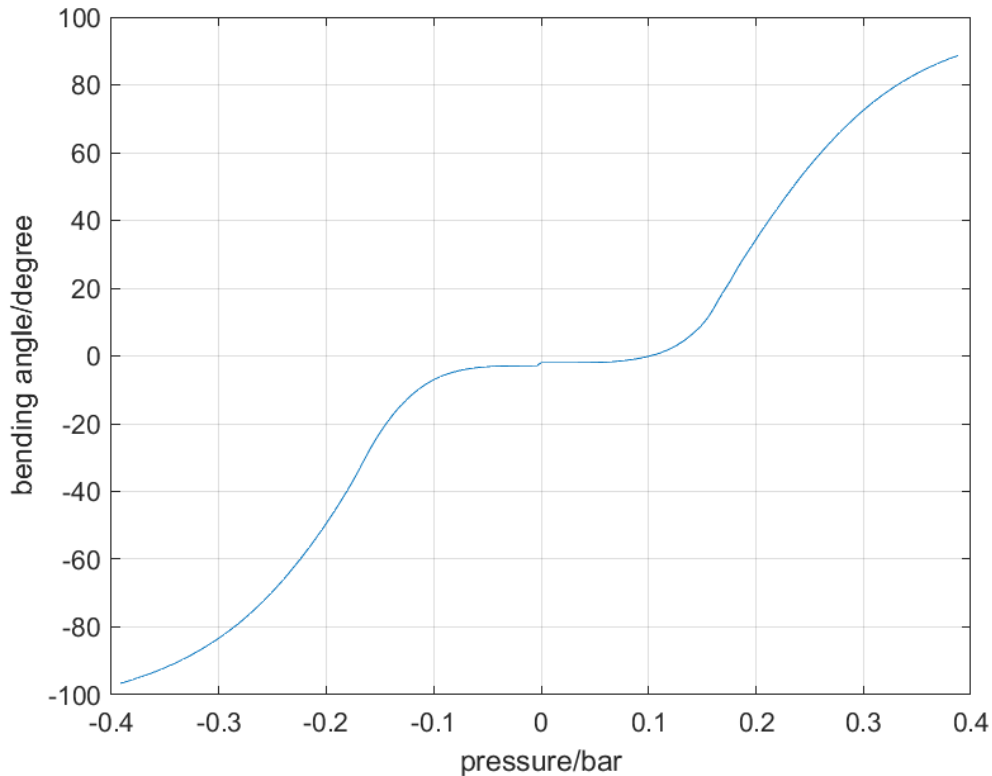


Figure 5.8 System characterization for both positive bending and negative bending

## 5.2. Experiments on bending control

Figure 5.9 shows the hardware of the control system. The sensor sends rotation matrix and translation vector to PID feedback controller and feedforward controller. The current bending angle  $\alpha_{cur}$  is derived from rotation matrix. The control effort  $\mu$  is calculated based on  $\alpha_{cur}$  and reference bending angle  $\alpha$  in real time. This control effort  $\mu$  is then translated into analog voltage signal by Arduino Uno microcontroller, to affect pressure regulators. In this experiment, if the value of  $\mu$  is positive, pressure regulator 1 will be activated, while pressure regulator 2 will be inactivated. Meanwhile, the negative value of  $\mu$  corresponds to activating pressure regulator 2, and inactivating pressure regulator 1. For this reason, the pressure in chamber 1 is controlled directly by pressure regulator 1. The pressure in both chamber 2 and chamber 3, are controlled by pressure regulator 2.

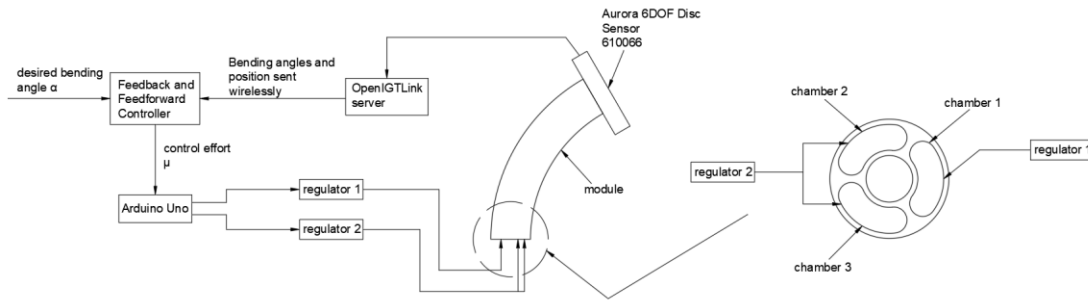


Figure 5.9 Implementation of the control system on hardware level. The desired bending angle  $\alpha$  is sent to the feedback and feedforward controller. By calculating the error between the current bending angle and the desired bending angle, the controller sends the control effort  $\mu$  to Arduino Uno which translates the control effort to the voltage of two regulators. Regulator 1 controls the pressure of chamber 1 and regulator 2 controls the pressure of chamber 2 and chamber 3.

The reference bending angle  $\alpha_{ref}(t)$  is a cycloidal function of time  $t$ . This cycloidal function can be referred as Equation (11).

$$\Delta(t) = 2\pi \frac{t - t_0}{t_1 - t_0}$$

$$\alpha_{ref}(t) = \begin{cases} A \frac{\Delta - \sin(\Delta)}{2\pi}, & 0 \leq \Delta \leq 2\pi \\ A, & \end{cases} \quad (11)$$

In this experiment, the amplitude  $A$  is  $30^\circ$ .  $t_0$  is the starting time which is  $0s$ , while  $t_1$  is the end time of cycloidal function which is  $30s$ . When time is more than  $30s$ ,  $\alpha_{ref}(t)$  will be consistent at  $30^\circ$ . Figure 5.10 shows the reference bending angle  $\alpha_{ref}(t)$  for both positive bending and negative bending. It is estimated that the control system including PID controller and feedforward controller would make the bending of the new design follow the trajectory of  $\alpha_{ref}(t)$ .

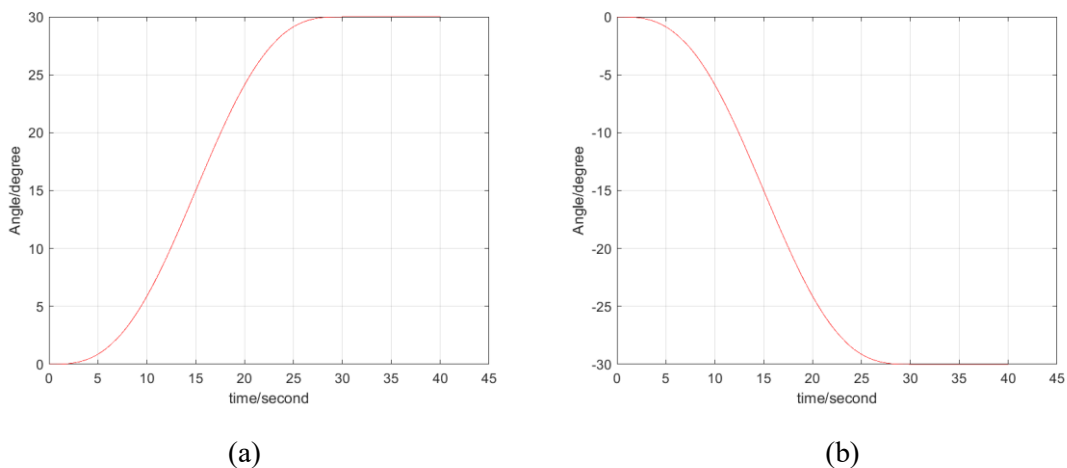


Figure 5.10 Desired one-plane bending angle as reference signal. (a) reference bending signal for positive bending (b) reference bending signal for negative bending

### 5.3. Results of experiments of bending control

For each module orientation, the validation experiments will be performed on three different planes. It is defined that positive bending in plane 1 is when chamber 1 is pressurized, while the negative bending is plane 1 is when chamber 2 and chamber 3 are pressurized simultaneously. Similarly, it is defined that

positive bending in plane 2 corresponds to only chamber 2 is pressurized, while negative bending in plane 2 is when chamber 1 and chamber 3 are pressurized simultaneously. Positive bending in plane 3 is defined as only pressurizing chamber 3, while the negative bending in plane 3 is defined as pressurizing chamber 1 and chamber 2 simultaneously.

The settings of PID controller should be properly tuned so that the response of the control system is fast enough, and the stable control system is obtained. Ziegler-Nichols tuning method is utilized for determining the values of proportional gain  $K_p$ , integral gain  $K_i$  and derivative gain  $K_d$ . These settings of PID controller are tuned manually until the response of control system is stable. The final settings of PID controller in this experiment are shown as follows:

$$K_p = 5 \times 10^{-4}$$

$$K_i = 2 \times 10^{-3}$$

$$K_d = 0$$

$$Prop(i + 1) = K_p Error(i + 1)$$

$$Int(i + 1) = K_i \sum_{j=1}^i \left( \frac{Error(i + 1) + Error(i)}{2} \Delta t \right)$$

$$Der(i + 1) = K_d \frac{Error(i + 1) - Error(i)}{\Delta t}$$

$$\mu_{fb}(i + 1) = Prop(i + 1) + Int(i + 1) + Der(i + 1)$$

The control performance will be unstable when  $K_p$  is more than  $5 \times 10^{-4}$ . In addition, non-zero  $K_d$  will also cause the control system unstable. The sensitivity of derivative part  $Der(i + 1)$  to noise is inversely proportional to the magnitude of the sampling time  $\Delta t$  of the controller.  $\Delta t$  is defined as how much time it takes for the controller to receive the measurement, run control logic and calculate the control effort. When the PID feedback controller works,  $\Delta t$  of each control cycle is inconstant. The varying  $\Delta t$  could be the source of instability when  $K_d$  is implemented with non-zero value.

Figure 5.11 shows the control performance on the module with or without load in vertical module orientation. The control performance on the module (with and without load) in inverted module orientation is shown in Figure 5.12. Figure 5.13 presents the control performance on the module (with and without load) in horizontal module orientation.

In Figure 5.11, it is observed that the value of the bending angle at 0s is nonzero. In the case of applying the coil sensor, one possible reason is the error of calibration. In this experiment, the initial state of the coil sensor should be vertical and perpendicular to the transversal cross-section area of the module. However, due to the dimension of the coil sensor, it is difficult to calibrate the sensor's orientation accurately. One possible solution for calibrating the orientation of the coil sensor is adding a cap on the tip of the module, which contains a concave surface for fixing the coil sensor.

Another possible reason for the non-zero initial bending angle is the bending hysteresis of the new design. The new design will not come back to its initial bending angle after the pressure is released. The validation experiments on the control performance are repeated several times, and the calibration

of the coil sensor is only conducted at the beginning of the first experiment. For this reason, the nonzero value of initial bending angle could be caused by the bending hysteresis of the new design.

For the disc sensor, the non-zero initial bending angle could result from the weight and the tension of the disc sensor.

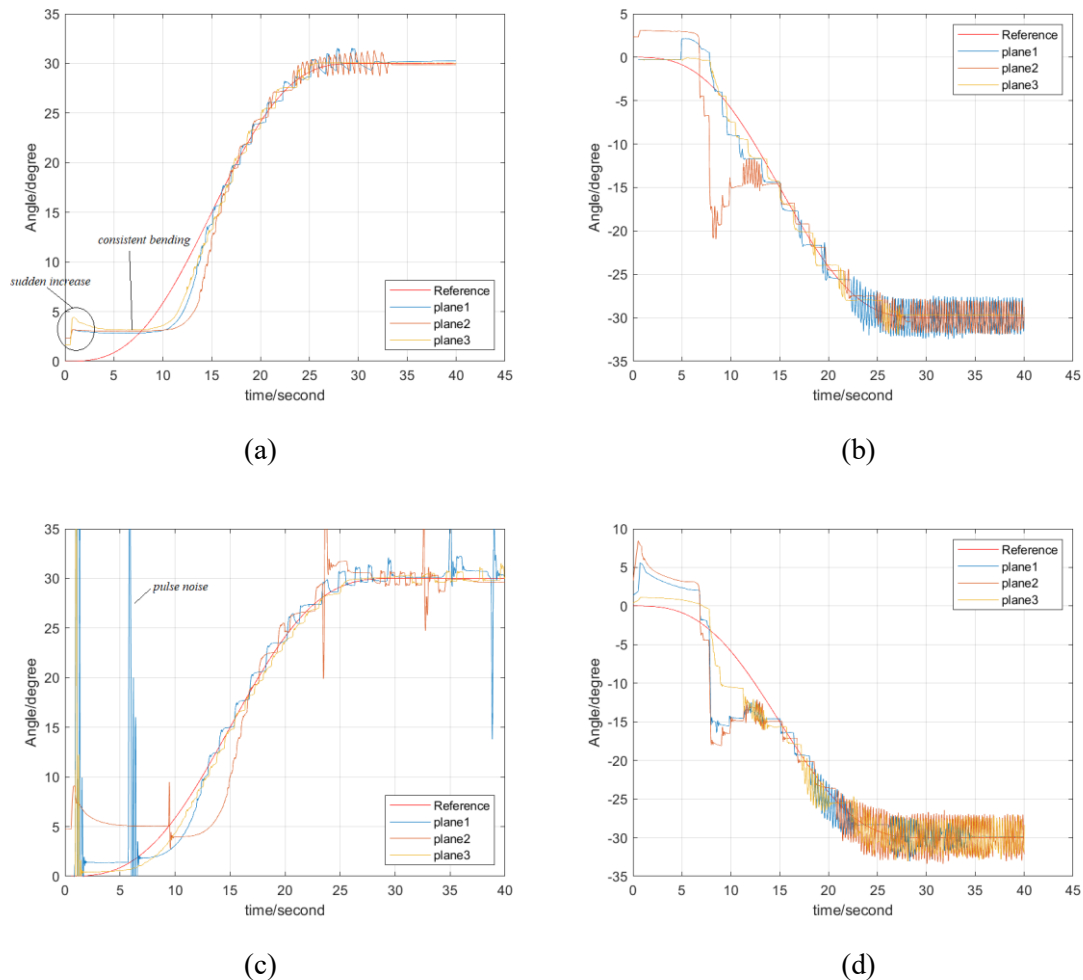


Figure 5.11 Control performance on module in vertical module orientation (a) Positive bending for module without load (b) Negative bending for module without load (c) Positive bending for module with load (d) Negative bending for module with load

Figure 5.11, Figure 5.12 and Figure 5.13 show a sudden increase of the bending angle when time is between 0s and 5s. The sudden increase of the bending angle could be caused by the response of the feedforward controller. It can be derived from Figure 5.8 that the feedforward control effort  $\mu_{ff}$  corresponding to zero value of  $\alpha_{ref}$ , will make the pressure regulator provide 0.1 bar air pressure to the module. This amount of air pressure would result in the sudden increase of the bending angle.

The total control effort  $\mu$  will decrease under the control effort of PID controller. However, due to the hysteresis property and zero-bending zone discussed in chapter 4, the varying control effort would lead to invariant bending angle. This could explain why the bending angle is consistent before 10s.

When time is more than 10s, the deviation between  $\alpha_{ref}$  and  $\alpha_{cur}$  is large enough to make the corresponding air pressure overcome zero-bending zone, and the bending angle of the module starts to follow the trajectory after 10s. It is shown in Figure 5.11 that the static control performance is not influenced by the limited load when the module is in vertical module orientation.

In Figure 5.11 (c), pulse noise occurs on the dynamic of the control performance. This pulse noise could not be the measurement noise of the sensor because this motion was observed in the experiment. One possible reason for the pulse noise is the varying sampling time of controller  $\Delta t$ . The mean sampling frequency of the controller is measured 40 Hz, which is the same as the sampling frequency of the sensor. However, due to the inconstant  $\Delta t$ , in some control cycles of PID controller, several samples from the sensor may pass between receiving a measurement and calculating the feedback control effort  $\mu_{fb}$ . Meanwhile, the value of  $\mu_{fb}$  depends on  $\Delta t$ . The delay of  $\Delta t$  could lead to a negative impact on the control performance and cause the pulse noise.

Another possible reason for the pulse noise is the dynamic system of the new design. The chamber of the module is connected with pressure regulator by pneumatic tubes which are 1m to 2m in length. The module with pneumatic tubes could be regarded as a storage of momentum of air (inductance) in series with a resistance of air flow and a storage of air pressure (capacitance) [25]. It means that the module in Figure 5.7 could be regarded as a second order system with respect to air pressure. The specific frequency of pressure change would result in pulse noise or even unstable response. However, this hypothesis needs to be verified because the flexibility of the pneumatic tube and the momentum of air are unknown. In this project, it is estimated that the resistance and inductance are more obvious than capacitance behavior, and the module of the new design with pneumatic tubes would be regarded as a first order system with respect to air pressure.

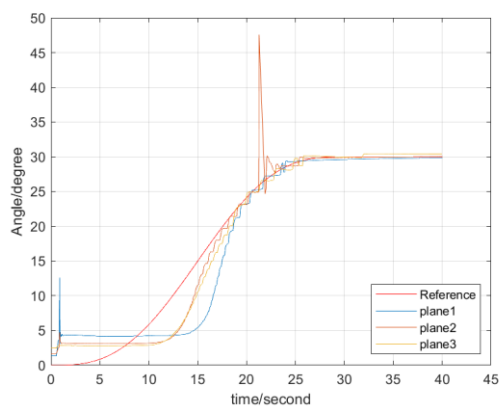
Figure 5.11 (b) and Figure 5.11 (d) show the oscillation of the bending angle around  $30^\circ$  in the static control performance. This oscillation behavior is also referred in Figure 5.12 and Figure 5.13. It seems that the oscillation occurs more frequently in negative bending than in positive bending. The different resolutions of two pressure regulators could be one reason causing the oscillation in the static control performance. In Figure 5.9, the resolution of pressure regulator 1 for positive bending is  $\frac{1}{255}$  bar, while the resolution of pressure regulator 2 for negative bending is  $\frac{2}{255}$  bar. The analog signal (PWM frequency) as input to pressure regulator is an integer number between 0 and 255. The optimal analog signal corresponding to control effort could be in the middle between two adjacent integer numbers. This may result in the analog signal changing between two adjacent integers and causing the oscillation of air pressure.

The bending of the module does not follow the trajectory when  $\alpha_{ref}$  is less than  $15^\circ$ . It may be caused by the zero-bending zone of the new design. As shown in Figure 4.9, the zero-bending zone and the low-gradient part of the new design correspond to pressure range from 0 bar to 0.1 bar, and the bending angle range from  $0^\circ$  to  $5^\circ$ . During this range of air pressure, the bending angle of the new design is insensitive to the change of the air pressure since the gradient of the bending angle to the air pressure is in low value referred in Figure 4.10. The bending angle  $10^\circ$  corresponds to air pressure 0.12 bar which is in the range of high-gradient part in Figure 4.10. The high-gradient part of the new design could explain why the bending of the module overcomes the consistent bending and starts to reduce the deviation between  $\alpha_{ref}$  and  $\alpha_{cur}$  because in this part, the change of the bending angle is much more sensitive to the change of the air pressure.

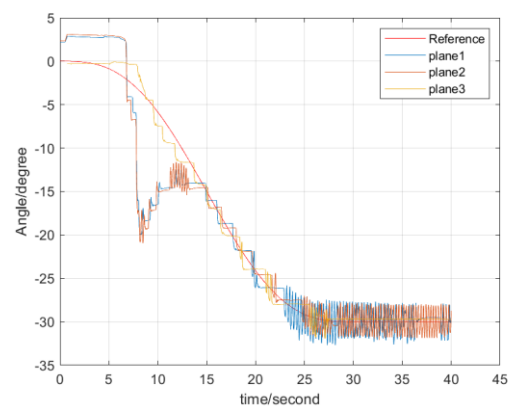
When  $\alpha_{ref}$  is more than  $15^\circ$ , the controller makes the bending of the module follow the trajectory. It means the PID controller has acceptable dynamic and static control performance when  $\alpha_{ref}$  is more than  $15^\circ$ .

Table 5- 1 Time of new design to start following the trajectory for different module orientations and limited load

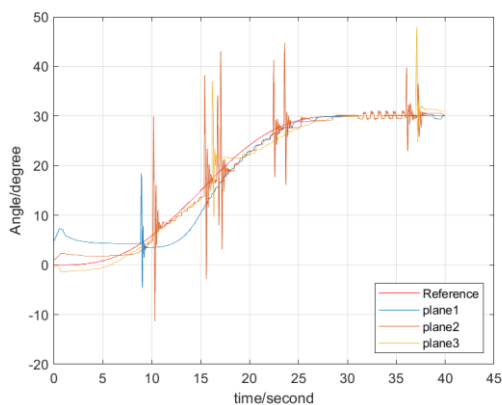
module orientation	bending direction	load/without load	time starting following the trajectory/ s
vertical	positive	without load	16.8
vertical	negative	without load	15
inverted	positive	without load	20
inverted	negative	without load	15
horizontal	positive	without load	15
horizontal	negative	without load	15
vertical	positive	with load	12.83-16.75
vertical	negative	with load	15
inverted	positive	with load	11.6-25
inverted	negative	with load	15
horizontal	positive	with load	20
horizontal	negative	with load	15



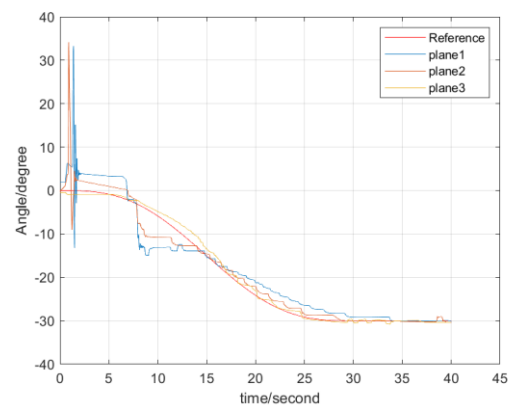
(a)



(b)



(c)



(d)

Figure 5.12 Control performance on module in inverted orientation. (a) Positive bending for module without load (b) Negative bending for module without load (c) Positive bending for module with load (d) Negative bending for module with load

As shown in Figure 5.12 and Figure 5.13, the load does not influence the static control performance. For assessing the dynamic control performance, Table 5.1 shows the time it takes for the controller to make the bending of the module follow the trajectory. As shown in Figure 4.13, the bending characterization of the module is asymmetric. Based on Figure 4.13 (a), the control performance in plane 1 is selected to reduce the influence of the asymmetric bending characterization, since the deviation of the bending characterization in plane 1 has the smallest value. For this reason, in Table 5.1, the positive bending refers to the actuation of chamber 1, while the negative bending refers to the actuation of chamber 2 and chamber 3 simultaneously.

It is estimated that the module orientations have influence on the dynamic control performance. It is verified at Table 5.1 that in positive bending, the time for the module without load in vertical, inverted and horizontal module orientation to follow the trajectory is 16.8s, 20s and 15s respectively. Moreover, in positive bending, the time for the module with load is different from the module without load. For instance, in positive bending, the time for the module without in vertical module orientation is 16.8s while the time for the module with load is 12.83s-16.75s. However, in negative bending, the time is independent on module orientations and limited load. This could be due to the control process. In negative bending, at time 0s, the feedforward control effort will result in the bending of the module in positive direction, while the reference bending angle varies in negative direction. This causes the deviation between  $\alpha_{ref}$  and  $\alpha_{cur}$  in negative bending more than that in positive bending. The larger deviation will lead to the rapid response of the feedback controller which could make the bending of the module overcome the zero-bending zone in a more rapid speed.

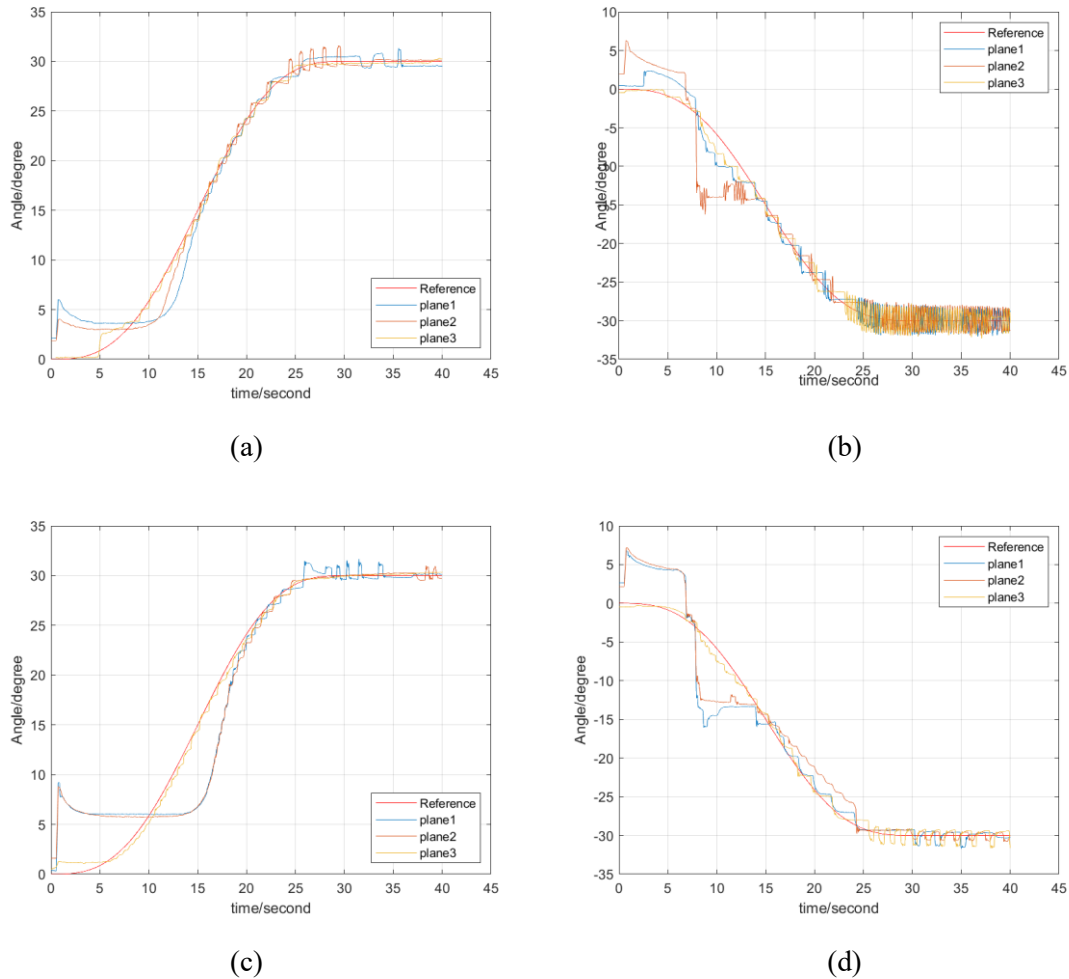


Figure 5.13 Control performance on module in horizontal orientation. (a) Positive bending for module without load (b) Negative bending for module without load (c) Positive bending for module with load (d) Negative bending for module with load

#### 5.4. Conclusion of one-plane bending angle control of new design

In this chapter, the PID feedback controller is developed for controlling the one-plane bending angle of the new design to compensate for the influence of module orientations and load. The feedforward controller based on the system characterization in chapter 4 is designed to improve the response of the PID controller. The control performance on the module in different load (0g and 20g) and module orientations (vertical, inverted and horizontal) is recorded and analyzed.

The result reveals that the static control performance is acceptable, when the desired bending angle is more than  $15^\circ$ , since the static bending angle of the module equals the reference with low steady state error, or the static bending angle oscillates around the reference. In addition, in the dynamic control performance, the controller is able to make the bending of the module follow the trajectory, when the desired bending angle is more than  $15^\circ$ . However, the controller is not able to make the bending of the module follow the given reference signal, when the reference bending angle is less than  $15^\circ$ . Possible reasons are the error of the feedforward controller, bending hysteresis and zero-bending zone of the physical module. In addition, the dynamic control performance contains issues such as non-zero initial bending angle, sudden increase of the bending angle, pulse noise and oscillation around the reference bending angle. The non-zero initial bending angle would be due to the bending hysteresis of the new design or the calibration error of the sensor. The sudden increase of the bending angle would be caused by the error of the feedforward controller. The pulse noise would be solved by reducing the delay of

sampling time of PID controller. The oscillation around the reference bending angle would result from different resolutions of pressure regulators.

The static control performance is not influenced by the load and module orientations. It is estimated that the load and module orientations will have impact on the dynamic control performance. However, due to the asymmetric bending characteristic of the module and nonzero initial bending angle, the effects of module orientations and load on dynamic control performance cannot be determined and it needs to be researched in the future proje

## 6. Conclusion and Future Work

### 6.1. Conclusion

This study aimed to downscale STIFF-FLOP manipulator for both laparoscopic and colonoscopy applications, and to control the bending performance of the new design to compensate for limited load and different module orientations. Insights were gained on how to downscale STIFF-FLOP manipulator with the criteria that the new design obtains maximal bending ability with limited dimension and structure. Meanwhile, this project also provides insight on how to control the bending of the new design so that the influence of limited load and module orientations can be compensated for.

The external diameter of the new design is 11.5 mm which is suitable for laparoscopy in terms of size. The new design can obtain 90° one-plane bending angle under input pressure 0.38 bar. The maximum pressure is estimated as 0.43 bar. Contrast to STIFF-FLOP manipulator, there is no obvious difference in one-chamber bending and two-chamber bending. The constant curvature assumption is examined by comparing the backbone curvature of the bending module with the estimated backbone curvature of constant radius. The result shows that the module of the new design is not compliant with constant curvature model because the backbone curvature of the bending module does not coincide with the estimated backbone curvature of constant radius.

The backbone of the bending module elongates 25% under pressure 0.4 bar. When all three chambers are activated by 0.4 bar air pressure, the module of the new design elongates around 10.6% with respect to the initial length (50 mm).

The PID feedback controller is developed to compensate for the influence of module orientations (vertical, inverted and horizontal) and load (0g and 20g) on the one-plane bending angle of the new design. It is also estimated to be able to compensate for the bending hysteresis which is observed in experimental characterization. The controller is functional in static control performance because it has low steady-state error or oscillation around the static reference bending angle. In addition, it can make the new design follow the reference trajectory, when the desired bending angle is more than 15°. However, the new design is not able to follow the reference bending angle, when the desired bending angle is less than 15°, due to the zero-bending zone in the bending characterization. Because the module of the new design contains asymmetric bending characteristic, the influence of limited load and different module orientations on the dynamic control performance is not determined in this project.

## 6.2. Future works

The elastomer of the new design meets the design requirement in terms of size. However, the implementation of the external braided sheath increases the diameter of the entire module slightly. The braiding could be embedded into the elastomer to reduce the dimension of the entire module.

The bending characterization of the physical module is not compliant with constant curvature model. A more accurate model should be developed considering this property. The module of the new design could be regarded as a constant curvature model connecting two rigid beams.

The elastomeric hysteresis property of the material could be studied in the future work. Meanwhile the stress-strain property of the chamber should be modelled and tested.

The PID controller is not able to make the bending of the new design follow the reference trajectory, when the desired bending angle is less than  $15^\circ$ . Methods could be implemented for improving the response of the controller in the zero-bending zone of the new design, and reducing the delay of the sampling time of the controller. Meanwhile, the pulse noise and oscillation issues should be solved in the future study.

In this project, the control of out-of-plane angle is not considered. The control algorithm should be developed for controlling both the one-plane bending angle and out-of-plane angle.

---

## Bibliography

1. Polygerinos, P., et al., *Soft Robotics: Review of Fluid-Driven Intrinsically Soft Devices; Manufacturing, Sensing, Control, and Applications in Human-Robot Interaction*. Advanced Engineering Materials, 2017. **19**(12).
2. Gifari, M.W., *Study on the Design of Soft Surgical Robots for Endoscopic NOTES Application*. 2018.
3. Cianchetti, M., et al. *STIFF-FLOP surgical manipulator: Mechanical design and experimental characterization of the single module*. in *IEEE International Conference on Intelligent Robots and Systems*. 2013.
4. Cianchetti, M., et al., *Soft Robotics Technologies to Address Shortcomings in Today's Minimally Invasive Surgery: The STIFF-FLOP Approach*. Soft Robotics, 2014. **1**(2): p. 122-131.
5. Fras, J., et al. *New STIFF-FLOP module construction idea for improved actuation and sensing*. in *Proceedings - IEEE International Conference on Robotics and Automation*. 2015.
6. Lenssen, J.A., H. Naghibi, and M. Abayazid. *Evaluation of design aspects of modular pneumatic soft robotic endoscopes*. in *RoboSoft 2019 - 2019 IEEE International Conference on Soft Robotics*. 2019.
7. Fraš, J., et al., *Static modeling of multisection soft continuum manipulator for stiff-flop project*, in *Advances in Intelligent Systems and Computing*. 2014. p. 365-375.
8. Mosadegh, B., et al., *Pneumatic networks for soft robotics that actuate rapidly*. Advanced Functional Materials, 2014. **24**(15): p. 2163-2170.
9. Abidi, H., et al., *Highly dexterous 2-module soft robot for intra-organ navigation in minimally invasive surgery*. International Journal of Medical Robotics and Computer Assisted Surgery, 2018. **14**(1).
10. Peng, Y., et al., *Development of continuum manipulator actuated by thin McKibben pneumatic artificial muscle*. Mechatronics, 2019. **60**: p. 56-65.
11. Connolly, F., C.J. Walsh, and K. Bertoldi, *Automatic design of fiber-reinforced soft actuators for trajectory matching*. Proceedings of the National Academy of Sciences of the United States of America, 2017. **114**(1): p. 51-56.
12. Babu, S.P.M., et al. *Antagonistic pneumatic actuators with variable stiffness for soft robotic applications*. in *RoboSoft 2019 - 2019 IEEE International Conference on Soft Robotics*. 2019.
13. Gorissen, B., M. De Volder, and D. Reynaerts, *Chip-on-tip endoscope incorporating a soft robotic pneumatic bending microactuator*. Biomedical Microdevices, 2018. **20**(3).
14. la Chapelle, C.F., et al., *Trocar types in laparoscopy*. Cochrane Database of Systematic Reviews, 2015(12).
15. Kim, Y., et al., *Toward the Development of a Flexible Mesoscale MRI-Compatible Neurosurgical Continuum Robot*. IEEE Transactions on Robotics, 2017. **33**(6): p. 1386-1397.
16. Blinman, T., *Incisions do not simply sum*. Surgical Endoscopy, 2010. **24**(7): p. 1746-1751.
17. Bernth, J.E., A. Arezzo, and H. Liu, *A Novel Robotic Meshworm With Segment-Bending Anchoring for Colonoscopy*. IEEE Robotics and Automation Letters, 2017. **2**(3): p. 1718-1724.
18. Alazmani, A., et al., *Quantitative assessment of colorectal morphology: Implications for robotic colonoscopy*. Medical Engineering and Physics, 2016. **38**(2): p. 148-154.
19. Lageveen, J.W., *Developing a Path Planning Algorithm to Enhance the Performance of a Soft Robotic Endoscope*. 2019.
20. Ahmad, D., S.K. Sahu, and K. Patra, *Fracture toughness, hysteresis and stretchability of dielectric elastomers under equibiaxial and biaxial loading*. Polymer Testing, 2019. **79**.
21. Hsu, Y.-Y., et al., *Novel Strain Relief Design for Multilayer Thin Film Stretchable Interconnects*. Electron Devices, IEEE Transactions on, 2013. **60**: p. 2338-2345.
22. Kim, S., et al. *Biomimetic skin-type shear sensor*. in *International Conference on Control, Automation and Systems*. 2016.
23. Ranzani, T., et al., *A bioinspired soft manipulator for minimally invasive surgery*. Bioinspiration and Biomimetics, 2015. **10**(3).
24. Webster Iii, R.J. and B.A. Jones, *Design and kinematic modeling of constant curvature continuum*

- robots: A review*. International Journal of Robotics Research, 2010. **29**(13): p. 1661-1683.
25. Lenssen, J.A., *Towards a steerable multi-module soft robotic endoscope for NOTES applications*. 2019.
26. Connolly, F., et al., *Mechanical programming of soft actuators by varying fiber angle*. Soft Robotics, 2015. **2**(1): p. 26-32.

---

## Appendices

### Appendix 1. Influence of unfixed external braided sheath on system characterization

In system characterization, the external braided sheath is fixed on both ends of the new design with original fiber angle  $0^\circ$ . In this part, the bending performance of the new design will be studied, when the external braided sheath is not fixed.

Figure A1 shows that the relative position between the elastomer and the external braided sheath contains three cases. In Figure A1 (a), the length of the external braided sheath is the same as the elastomer, however the fiber angle of the external braided sheath is not  $0^\circ$ . This configuration is defined as case 1. After some repetition of system characterization experiments, the external braided sheath will elongate, and the relative position between the elastomer and the external braided sheath will alter which is shown in Figure A1 (b). This configuration is defined as case 2. In this case, both the fiber angle and the length of the external braided sheath increase. If the external braided sheath is compressed too much as shown in Figure A1 (c), the length of the external braided sheath will be less than the elastomer, and the fiber angle will decrease compared to case 1. It is defined as case 3 in this article.

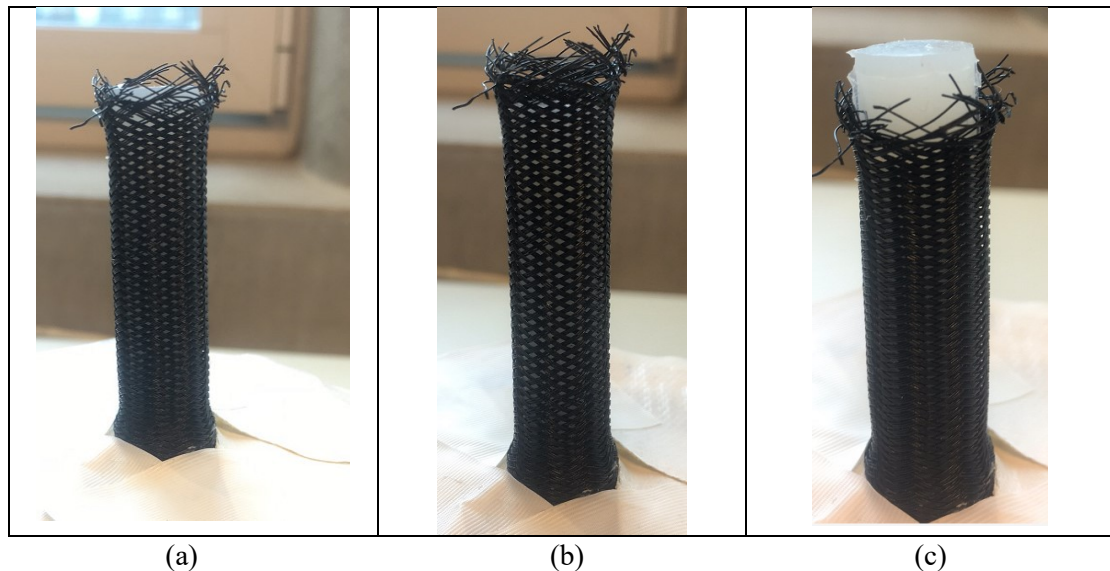


*Figure A1. Tested new design with unfixed braided sheath. (a) Case 1: The length of external braided sheath is the same as elastomer. (b) Case 2: The external braided sheath elongates and its fiber angle increases. (c) Case 3: The external braided sheath is compressed and its fiber angle decreases.*

The system characterization of the module in three cases is shown in Figure A2. It is observed that if the external braided sheath is not fixed, the module of the new design will have different bending performance due to different relative position between the external braiding and the elastomer. With the same input pressure, case 3 obtains the largest bending angle while case 1 obtains the smallest bending angle. One possible reason could be due to different fiber angles in different cases. It has been proven that the braiding with  $0^\circ$  fiber angle will result in the maximal elongation performance of the pneumatic actuator, while the increase of fiber angle will lead to the decrease of elongation performance [26]. The relative movement between the external braided sheath and the elastomer would cause the change of the fiber angle of the external braided sheath, and would decrease the bending performance of the new design.

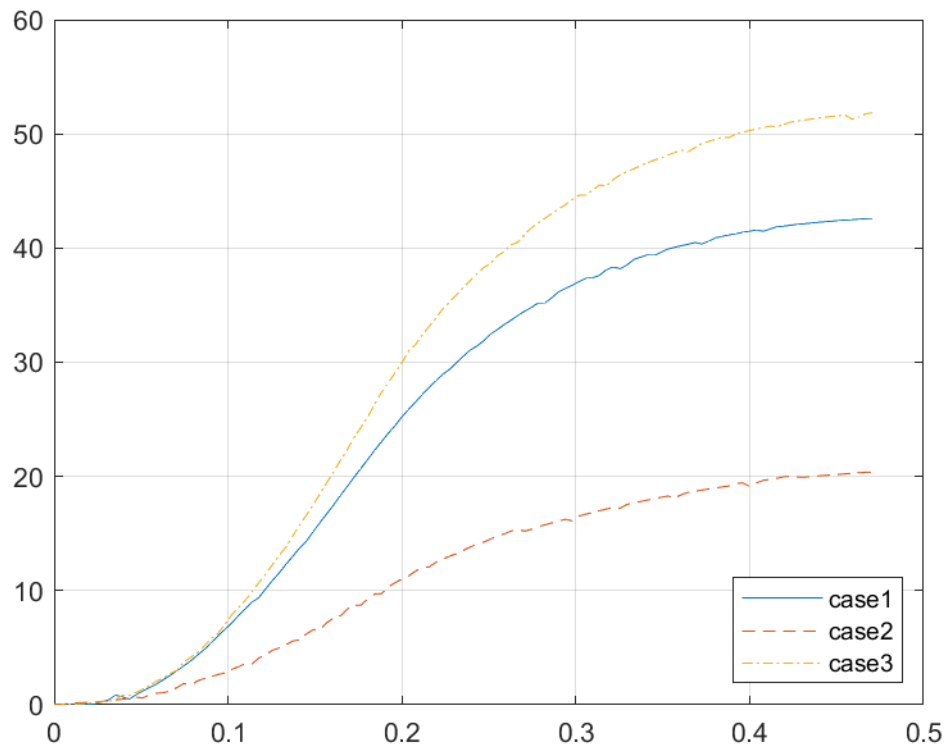


Figure A2 System characterization of new design with unfixed external braided sheath shown in Figure A1

## Appendix 2. List of material for downscaled STIFF-FLOP design

Material:

- 1) EcoFlex 0050 Liquid Silicone Elastomer
- 2) Dragon Skin 10 Liquid Silicone Elastomer
- 3) Plastic glue
- 4) Braided sleeve with diameter of 5mm
- 5) Pneumatic tubes with diameter of 2mm

### Appendix 3. Detailed fabrication processes

Figure 3.12 shows that the molding process of the new design can be divided into four steps. First, the molds, containing central cylinder, chamber A, shell A and cap A, are arranged in the configuration shown in Figure 3.12 (a). The material is poured into this combination of molds until the edge of shell A. In this step, the chamber body part of the new design is fabricated. Second, after the silicone cures, the height of shell A is adjusted 10 mm higher than previous step, while other molds are not changed. This molds configuration is shown in Figure 3.12 (b). Another silicone material (Dragon Skin 10) is then poured into the new configuration of molds to make the bottom part of the new design. Dragon Skin 10 is chosen because the bottom part made of Eco-Flex 0050 will have leakage issue when it is pressurized. Third, after the elastomer cures, it is removed from the combination of molds. It is shown in Figure 3.12 (c) that three chamber B molds are replacing three chamber A molds in the elastomer. The chamber B mold contains the slope connection between the small part and the large part. The slope structure makes the chamber B molds easily removed from the bottom part of the new design after the entire molding process is completed. The elastomer with three chamber B molds is then inserted into a new molds configuration shown in Figure 3.12 (d). This molds configuration comprises the central cylinder, shell B and cap B. To fabricate the top part of the new design, similar to step in Figure 3.12 (b), Dragon Skin 10 is poured into the new configuration until the edge of the shell B. Finally, after the elastomer cures, three chamber B molds are removed from the elastomer of the new design by dragging the small part of the chamber B mold away from the elastomer.